

796

INTERACTION OF THE NUCLEATION PHENOMENA
AT ADJACENT SITES IN NUCLEATE BOILING

INTERACTION OF THE NUCLEATION PHENOMENA
AT ADJACENT SITES IN NUCLEATE BOILING

by

MOHAMMED A. H. SULTAN, B.Sc., M.Eng.

A Thesis

Submitted to the School of Graduate Studies

in Partial Fulfilment of the Requirements

for the Degree

Doctor of Philosophy

McMaster University

November, 1980

TO MY WIFE BOSHRA
AND TO MY KIND PARENTS

DOCTOR OF PHILOSOPHY (1980)
(Mechanical Engineering)

McMASTER UNIVERSITY
Hamilton, Ontario

TITLE: Interaction of the Nucleation Phenomena
at Adjacent Sites in Nucleate Boiling

AUTHOR: Mohammed Abd El-Moty Hamed Sultan

B.Sc. (Alexandria University,
Alexandria, Egypt)

M.Eng. (McMaster University)

SUPERVISOR: Dr. Ross L. Judd

NUMBER OF PAGES: xvii, 163

ABSTRACT

This investigation is an original study in nucleate pool boiling heat transfer, consisting of two parts: an experimental study and a theoretical study. The experimental study was performed with water boiling at atmospheric pressure on a single copper surface. Two different levels of heat flux were investigated. For the lower level of heat flux (92.21 kW/m^2), three different levels of subcooling ($0, 6.5, 12^\circ\text{C}$) were studied and for the higher level of heat flux (192.11 kW/m^2), two different levels of subcooling ($0, 7.5^\circ\text{C}$) were studied as well.

The cross-spectral density function and the cross-correlation function were used to determine the time elapsed (τ) between the start of bubble growth at two neighbouring active sites with separation (S). The experimental results indicate that for the lower level of heat flux at three different levels of subcooling, the separation (S) and the time elapsed (τ) are related. For the higher level of heat flux at 0°C subcooling it was not possible to detect any correlation, but for the 7.5°C subcooled condition a weak correlation was found to exist. For the lower level of heat flux, all the experimental data for the saturated and subcooled boiling conditions plotted as $(S-R_d)$ versus $(\tau-\tau_g)$ drew together into a single curve, indicating that a single relationship could fit all the data.

Three different theoretical models were devised in an attempt to explain the experimental observations. The first model involved heat diffusion in the water; the second model was based upon the disturbance caused by the propagation of a pressure pulse in a mixture of water and vapour and finally the third model involved heat diffusion in the solid. The first two models failed to give satisfactory agreement with the experimental results, but the theoretical predictions corresponding to heat diffusion through the solid gave good agreement with the experimental findings.

ACKNOWLEDGEMENTS

The author wishes to express his sincere gratitude to his supervisor Dr. Ross L. Judd for his valuable advice, useful suggestions, guidance and continuous encouragement throughout the duration of the present investigation.

Sincere thanks are extended to Dr. J. H. T. Wade, Professor J. N. Siddall and Professor C. W. Dunnett for their helpful comments and acting as members of the Ph.D Supervisory Committee.

Thanks are also due to Ms. BettyAnne Bedell for typing the manuscript.

The financial assistance of McMaster University and the Natural Sciences and Engineering Research Council of Canada through grant A4362 is appreciated.

Finally, gratitude is expressed to my beloved wife, Boshra, for her continuous encouragement and patience throughout the duration of my studies.

TABLE OF CONTENTS

	<u>Page</u>
NOMENCLATURE	x
LIST OF FIGURES	xiii
LIST OF TABLES	xvii
CHAPTER 1 INTRODUCTION	1
CHAPTER 2 LITERATURE SURVEY	5
2.1 Introduction	5
2.2 Indentification of Active Sites	8
2.3 Interaction of Nucleation Sites in Nucleate Boiling	16
2.4 Bubble Flux Density	18
CHAPTER 3 EXPERIMENTAL INVESTIGATION	24
3.1 Experimental Apparatus	24
3.1.1 Boiler Assembly	25
3.1.2 Temperature Measurement System	28
3.1.3 Power Circuitry and Measurement	38
3.1.4 Bubble Detection Probe	41
3.1.5 Nucleation Site Locating System	46
3.2 Test Conditions	46
3.3 Test Procedures	48
CHAPTER 4 STATISTICAL SIGNAL PROCESSING	53
4.1 Digitizing of Continuous Data	53
4.2 Measurement of the Time Elapse	58

	<u>Page</u>
4.2.1 Determination of Time Elapse By Cross-Spectral Density Function Analysis	59
4.2.2 Determination of Time Elapse By Cross-Correlation Function Coefficient Analysis	62
4.3 Confidence Limit on the Cross-Correla- tion Function Coefficient	64
4.4 Signal Processing Flowchart	65
4.5 Representative Example	65
CHAPTER 5 RESULTS AND DISCUSSION	70
5.1 Experimental Results	70
5.2 Theoretical Analysis and Discussion	82
5.2.1 Heat Diffusion Through the Water	85
5.2.2 Propagation of a Pressure Pulse	91
5.2.3 Heat Diffusion Through the Surface	102
5.3 Implications of the Research	112
REFERENCES	117
APPENDIX A ESTIMATION OF THE HEAT TRANSFER RATE	121
APPENDIX B BULK LIQUID TEMPERATURE	131
APPENDIX C PROPAGATION OF A TEMPERATURE DISTURB- ANCE IN A SEMI-INFINITE MEDIUM	136
APPENDIX D PREDICTION OF ACTIVE SITE DENSITY, BUBBLE GROWTH PERIOD, BUBBLE EMISSION FREQUENCY AND BUBBLE DEPARTURE SIZE	140
APPENDIX E DETERMINATION OF QUALITY IN TWO-PHASE MIXTURES	144
APPENDIX F TIME DELAY CALIBRATION	148
APPENDIX G BUBBLE DETECTION PROBE ASSEMBLY	152

	<u>Page</u>
APPENDIX H EXPERIMENTAL DATA AND RESULTS	157
APPENDIX I CORRELATION ANALYSIS	162

NOMENCLATURE

<u>SYMBOL</u>	<u>DESCRIPTION</u>
Q	Rate of Heat Transfer
A	Total Area of Heat Transfer Surface
Q/A	Heat Flux
D	Bubble Departure Size
a	Pressure Pulse Propagation Velocity
C	Specific Heat
h	Sampling Interval
\bar{h}_c	Heat Transfer Coefficient
h_{fg}	Latent Heat of Vaporization
f	Bubble Frequency
f_c	Cutoff Frequency
k	Thermal Conductivity
m	Mass
P	Pressure
S	Separating Distance
s	Entropy
t	Time
T	Temperature
R_d	Bubble Departure Radius
\bar{R}	Average Bubble Radius
N/A	Active Nucleation Site Density
x	Quality of the Two-Phase Mixture
N	Number of Digitizing Samples for Each Probe
x(t)	Probe #1 Signal
y(t)	Probe #2 Signal

μ_x	Mean Value of Series $x(t)$
μ_y	Mean Value of Series $y(t)$
R_x	Auto-Correlation of Series $x(t)$
R_y	Auto-Correlation of Series $y(t)$
f_x	Predominant Frequency of Series $x(t)$
f_y	Predominant Frequency of Series $y(t)$
C_{xy}	Cross-Covariance of Non Zero Mean
R_{xy}	Cross-Covariance of Zero Mean
S_{xy}	Cross-Spectral Density Function
L_{xy}	Co-Spectral Density Function
Q_{xy}	Quadrature Spectral Density Function
θ_{xy}	Cross-Spectral Phase Shift
$ S_{xy} $	Cross-Spectral Magnitude
ρ_{xy}	Cross-Correlation Function Coefficient
C_{xy}	Coherence Function
$P(t)$	Probability Density Function
$R_{S\tau}$	Regression Coefficient (S, τ)

GREEK LETTERS

ρ	Density
σ	Surface Tension
λ	Gamma Distribution Scaling Parameter
ν	Gamma Distribution Shape Parameter
θ	Contact Angle
τ	Elapsed Time
τ_g	Bubble Growth Period
τ_w	Bubble Waiting Period

τ_T	Bubble Cycle Time
κ	Thermal Diffusivity

SUBSCRIPTS

l	Liquid
v	Vapour
w	Surface
s	Saturation
∞	Bulk
i	Inside
o	Outside

LIST OF FIGURES

Figure		<u>Page</u>
1	The Formation of Vapour Bubbles Over Cavities in a Heated Surface	7
2	Influence of Heat Flux on the Active Site Pattern	9
3	Influence of Subcooling on the Active Site Pattern	9
4	Active Nucleation Site Distribution According to Judd	13
5	Distribution of Active Nucleation Sites According to Sultan and Judd	15
6	Effect of Carrier Frequency on the Bubble Detection Probe Response	17
7	Shape Factor Versus Distance Between Two Nucleation Centers	19
8	Distribution of Bubble Flux Density	21
9	Cumulative Percentage Bubble Flux Density Versus Cumulative Percentage Area	22
10	Section of Boiler Vessel	26
11	Nucleation Site Location System	29
12	Experimental Arrangement	30
13	Experimental Arrangement	31
14	Thermocouple Locations	34
15	Thermocouple Assembly	35
16	Thermocouple Circuit	37
17	Thermocouple Switching Arrangement	39
18	Power Circuit Diagram	40
19	Bubble Detection Probe Assembly	42
20	Signal Conditioning Unit	44

	<u>Page</u>
21	Influence of Probe Displacement from Nucleation Site 45
22	Telescope 47
23	Output of the Conductance Probes Situated at Two Neighbouring Active Sites 54
24	Sampling of Continuous Record 55
25	Sampling Near the Cut off Frequency 57
26	Signal Processing Flowchart 66
27	Example of the Data Obtained in the Present Study 67
28	Characteristic Boiling Curve for Present Investigation 72
29	Arrangement of Active Nucleation Site (A) and Its Surrounding Active Nucleation Sites (B, C, D, E, F) 73
30	Relationship Between Elapsed Time (τ) and Separating Distance (S) 75
31	Relationship Between Elapsed Time (τ) and Separating Distance (S) 76
32	Relationship Between Elapsed Time (τ) and Separating Distance (S) 77
33	Relationship Between Elapsed Time (τ) and Separating Distance (S) 78
34	Relationship Between Elapsed Time (τ) and Separating Distance (S) 79
35	Relationship Between Elapsed Time (τ) and Separating Distance (S) 80
36	Relationship Between Elapsed Time (τ) and Separating Distance (S) for Three Levels of Subcooling 81
37	Distance ($S-R_d$) Versus Time Elapse ($\tau-\tau_g$) 84
38	Interference Fringe Pattern for a Growing Freon 113 Bubble 86
39	Distribution of High Temperature Liquid in the Vicinity of a Growing Bubble 87

	<u>Page</u>
40	Idealized Model for Heat Diffusion from an Instantaneous Ring Source of Strength Q in the Surrounding Water 88
41	Comparison Between the Theoretical Pre- diction for Heat Diffusion in the Water and the Experimental Findings 92
42	Pressure Pulse Propagation Originating from an Active Nucleation Site 93
43	Pressure-Density Diagram for Water 96
44	Velocity of Sound in Two-Phase Region for Water 99
45	Effect of Quality on Velocity of Sound in Two-Phase Region for Water 100
46	Comparison Between the Theoretical Prediction of the Pressure Pulse Dis- turbance and the Experimental Findings 103
47	Heat-Transfer Coefficient Obtained By Barakat and Sims 104
48	The Directions of the Flow Around a Bubble During Growth and After Bubble Detach- ment 105
49	Temperature Distribution in a Copper Heating Wall After Bubble Detachment 107
50	Temperature Distribution in a Steel Heating Wall After Bubble Detachment 107
51	Idealized Model for the Transfer of Heat from an Instantaneous Ring Source to the Heating Surface 108
52	Superposition of Temperature Distributions 109
53	Comparison Between the Experimental Results and the Prediction of Heat Diffusion in Solid 113
54	Comparison Between the Theoretical Prediction of the Heat Diffusion in the Solid and the Experimental Findings 114

	<u>Page</u>
55	Comparison Between the Three Theoretical Models Predicting the Correlation of the Distance ($S-R_d$) with Time Elapse ($\tau-\tau_g$) 115
56	Heat Loss From the Heater Block 122
57	Location of Thermocouples Used in Determining Heat Loss 124
58	Temperature Gradient in the Heater Neck 129
59	Thermocouple Probe 132
60	Bulk Liquid Temperature Profiles for Saturated Conditions 133
61	Bulk Liquid Temperature Profiles for Subcooled Conditions 134
62	Control Volume for Determination of the Quality of Two-Phase Mixtures 145
63	An Example of the Time Delay Calibration for $x(t)$ Leading or Lagging $y(t)$ (Cross-Correlation Function) 149
64	Time Delay Calibration for $x(t)$ Leading or Lagging $y(t)$ (Cross-Correlation Function) 150
65	Time Delay Calibration for $x(t)$ Leading or Lagging $y(t)$ (Cross-Spectral Density Function) 151
66	Bubble Detection Probe Assembly 153
67	Positioning Mechanism 155
68	Relationship Between the Separation Distance and the Number of Dial Indicator Turns 156

LIST OF TABLES

TABLE		<u>Page</u>
1	Location of Thermocouples in the Neck of the Copper Heating Block	35
2	Nominal Values of Test Conditions	49
3	Estimated Values of Departure Radius and Bubble Growth Time	83
4	Thermocouple Readings	127
5	Tabulation of the Experimental Data	158
6	Tabulation of the Experimental Results	161
7	Correlation Coefficient Analysis	163

CHAPTER 1

INTRODUCTION

In recent years, boiling heat transfer has achieved world wide interest since it is the most efficient mode of heat transfer in use. The boiling phenomenon is associated with the transfer of tremendous quantities of thermal energy relative to the heat transfer rate attainable in non-boiling systems. Thus, boiling heat transfer is frequently applied as a cooling mechanism in processes which involve very high density heat generation rates such as those that are found in nuclear reactors.

Boiling heat transfer is defined as the mode of heat transfer that occurs with change of phase from liquid to vapour. When the surface temperature exceeds the saturation temperature of the liquid sufficiently, vapour bubbles form at specific locations on the heating surface such as pits, scratches, and grooves which have the ability of trapping vapour. These locations at which bubbles originate are called active sites. The bubbles grow rapidly in the superheated liquid layer adjacent to the surface until they attain maximum size. Depending upon whether the liquid is subcooled or superheated, the bubbles will either collapse or continue growing and move out into the bulk of the liquid.

Because of the extensive experimental and theoretical

research conducted by many researchers in the last two decades which has provided better understanding of the nucleate boiling phenomenon, many of the boiling parameters such as bubble growth, waiting time, departure size, bubble emission frequency, etc. in the single bubble regime can be predicted with a reasonable degree of accuracy. However, one of the assumptions involved in these predictions is that no interaction occurs between the bubbles, so that the fundamental mechanism of heat transfer which prevails in nucleate boiling has not been conclusively established due to the lack of information to describe the multiple bubble regime.

Extrapolating from the single bubble viewpoint to the multiple bubble viewpoint, it is necessary to address two aspects of the boiling phenomenon which are interrelated, the first of which is nucleation site interaction and the second of which is multiple bubble interaction. Information about nucleation site interaction is required and it is this topic which the present thesis addresses.

As far as nucleation site interaction is concerned, the only direct reference to this phenomenon is Chekanov [1], who experimentally studied the interaction between two artificial nucleation centers in nucleate boiling for saturated and subcooled conditions at atmospheric pressure. Chekanov analyzed experimental measurements of the time elapsed between the start of bubble growth at two neighbouring active sites as a random variable. Using a statistical distribution for the elapsed time, this was found to follow the Gamma distribution. At a distance of more

than three times the bubble maximum diameter, "attractive" interaction occurred and the growth of a bubble at one center enhanced the growth of a bubble at the other. For a distance of less than three times the bubble maximum diameter, "repulsive" interaction occurred and the growth of a bubble at one center inhibited the growth of a bubble at the other.

The bubble flux density of water boiling at atmospheric pressure on a single copper surface was studied by Sultan and Judd [2], whose results indicated that the formation of bubbles occurs in a non-uniform manner over a heating surface. According to the boiling conditions used and the non-uniform distribution of bubble flux density observed, the formation of bubbles was assumed to originate within small areas which had a diameter about three times the maximum bubble diameter. Because of the cluster effect these results were found to be inconsistent with Checkanov's [1] results which indicated that the formation of a bubble at one nucleation site inhibited the formation of a bubble at a neighbouring nucleation site if the nucleation site spacing became very small. A theoretical model to explain this phenomenon does not exist and hence the potential usefulness of the present investigation is obvious.

The study reported herein was performed to determine the effect of bubble formation at a particular active site on the bubble formation at the surrounding active sites. It consists of two parts: an experimental study and a theoretical study. The experimental study was performed with water boiling

at atmospheric pressure on a single copper surface at different levels of heat flux and subcooling. The experimental results were obtained from analysis of the cross-spectral density function and the cross-correlation function coefficient. Three different theoretical models were devised in an attempt to explain the experimental findings. A theoretical model involving heat diffusion in the solid close to the heating surface gave good agreement with the experimental results, suggesting that this is the mechanism responsible for the activation of the surrounding nucleation sites.

CHAPTER 2

LITERATURE SURVEY

2.1 Introduction

The phenomenon of nucleate boiling is governed by the process of bubble nucleation. So far, there is no completely satisfactory theory of nucleation and in general there are two main types of nucleation, homogeneous and heterogeneous nucleation. The heterogeneous nucleation is of more interest so far as most of the engineering applications are concerned.

Homogeneous nucleation takes place in pure liquids where no suspended non-wettable matter exists or in a container with very smooth walls. The theory of homogeneous nucleation has been advanced through the kinetic approach by Becker and Doring [3], Volmer [4] and Frenkel [5], who considered the molecules of which the liquid is composed to have a distribution of energies such that only a small fraction have energies considerably greater than the average. Such activated molecules are assumed to initiate the nucleation by a step-wise collision process in which inactivated molecules become activated and join a cluster of activated molecules until the cluster is sufficiently large and contains sufficient energy to spontaneously explode into a vapour bubble. Therefore, very high levels of superheat are required for homo-

geneous nucleation to be initiated.

In heterogeneous nucleation where nucleation is observed to occur on the walls rather than in the bulk of the liquid, the surface temperatures at which nucleation takes place are very much smaller than those required for homogenous nucleation. Casual observations of nucleate boiling show bubble streams originating from specific locations on the heating surface; microscopic observation of these locations reveals a cavity or a scratch where a bubble nucleates. Corty and Foust [6], Bankoff [7], Clark, Streng and Westwater [8] and others developed the postulate that bubbles at a heating surface originate from surface cavities in which a gas or a vapour pre-exists as shown in figure (1). As heat is added, more vapour forms in the cavity as shown in figure (1.a) and a bubble forms and departs as shown in figure (1.b), after which liquid closes in over the cavity trapping vapour which becomes the nucleus for the next bubble. Two cases of different contact angle and opposite curvature of the vapour-liquid interface may be considered. In figure (1.c) where the vapour pressure is larger than the liquid pressure, the cavity if it contains pure saturated vapour in thermal equilibrium with the cavity walls, will collapse and be completely filled with liquid as the surface is allowed to cool below the saturation temperature of the liquid, thus becoming inactive. In figure (1.d) where the vapour pressure is less than the liquid pressure, the interface recedes into the cavity as the surface cools below the saturation temperature

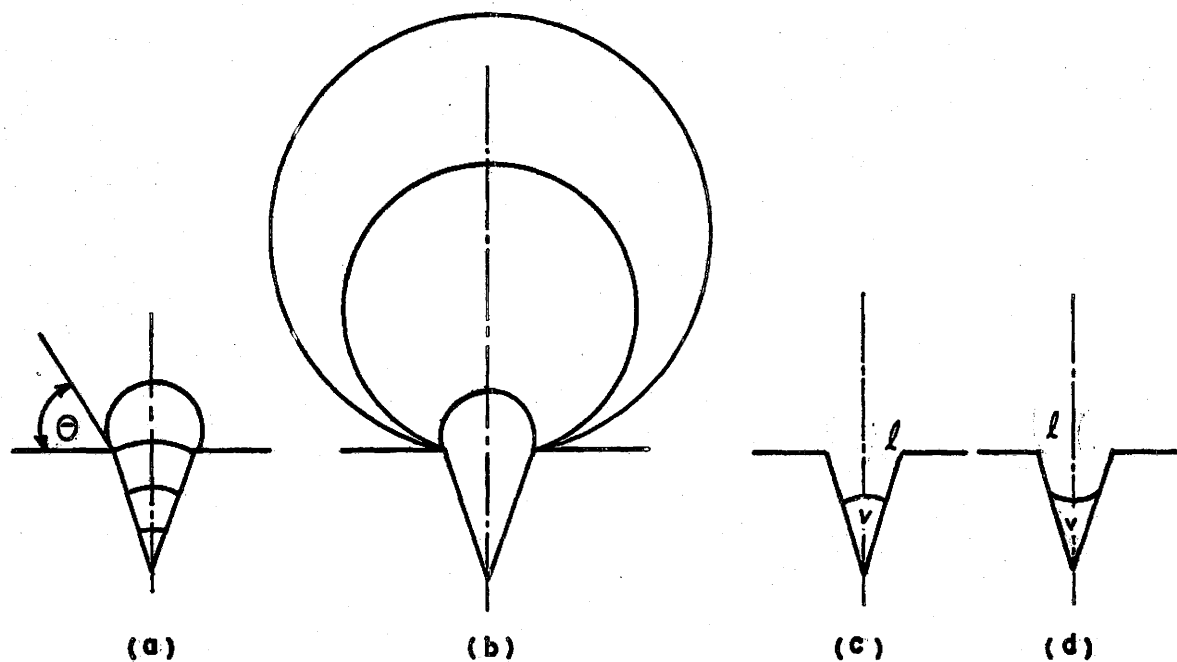


Figure (1). The Formation of Vapour Bubbles Over Cavities in a Heated Surface

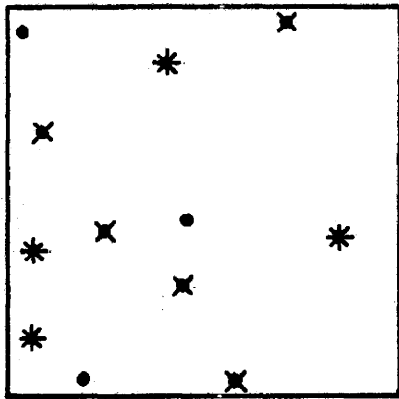
of the liquid thereby increasing the radius of curvature and reducing the vapour pressure. Since the vapour pressure decreases, its saturation temperature decreases. Consequently, the nucleus can be reactivated if the surface is subsequently reheated.

The influence of heat flux and subcooling on the pattern of the active nucleation sites was studied by Sultan and Judd [2]. An area of (0.2 x 0.2) inch square was selected from the area tested to examine the change in pattern of the active nucleation sites with changing heat flux and subcooling during a single experimental run. Figure (2) shows the influence of three different levels of heat flux on the active nucleation site pattern at constant subcooling. As the heat flux increased, bubbles continued to originate from the nucleation sites already activated and some more nucleation sites appeared due to the increase of heat flux. Figure (3) shows the influence of three different levels of subcooling on the active nucleation site pattern at constant heat flux. As the subcooling increased, the active nucleation site pattern did not change.

2.2 Identification of Active Sites

There are five different site identifying techniques which are known at the present time; electroplating, observation of thin scale deposits, scanning electron microscopy, high speed camera and electrical probe methods.

The electroplating technique was investigated by



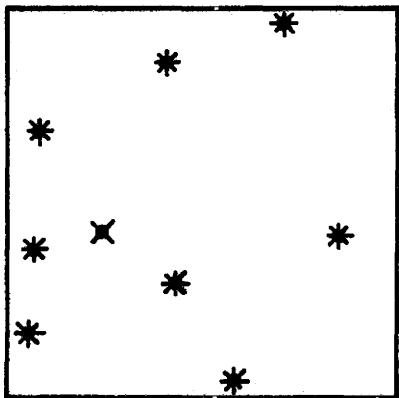
$$+ \quad \frac{Q}{A} = 20,300 \text{ (BTU/HR FT}^2\text{)}$$

$$x \quad \frac{Q}{A} = 52,600 \text{ (BTU/HR FT}^2\text{)}$$

$$\bullet \quad \frac{Q}{A} = 105,600 \text{ (BTU/HR FT}^2\text{)}$$

$$(T_S - T_\infty) = 20 \text{ (}^\circ\text{F)}$$

Figure (2). Influence of Heat Flux on the Active Site Pattern



$$+ \quad (T_S - T_\infty) = 3 \text{ (}^\circ\text{F)}$$

$$x \quad (T_S - T_\infty) = 20 \text{ (}^\circ\text{F)}$$

$$\bullet \quad (T_S - T_\infty) = 36 \text{ (}^\circ\text{F)}$$

$$\frac{Q}{A} = 52,600 \text{ (BTU/HR FT}^2\text{)}$$

Figure (3). Influence of Subcooling on the Active Site Pattern

Gaertner and Westwater [9] to determine the locations as well as the number of active sites up to $17.5 * 10^5$ sites/m². Approximately 3 1/2 liters of nickel-plating solution was placed in a boiler for a run. A copper heating surface was prepared by a series of seven grades of emery paper ending with grade 4/0. The technique was based on the electroplating phenomena by which an impressed current, at low heat flux resulted in a nickel film being plated on the copper surface. The electroplating technique indicated the location of the active sites, since during the electroplating, vapour bubbles originating at the active sites would push the plating solution away from the heating copper surface so that very little nickel could be plated at the active site locations. Then high contrast photographs were taken of the plated surface to permit counting of the pinholes representing the active sites. However, this technique is restricted to electroplating solutions only.

The technique of observing thin scale deposits was proposed by Heled and Orell [10], which greatly facilitates the identification and location of active sites over the boiling heating surface. This technique was based on the observation of thin scale deposits ($12.7 * 10^{-3}$ to $76.2 * 10^{-3}$ μm) which were formed on highly polished surfaces (first polished to a high degree and then electroplated with either chrome or nickel). The tap water or distilled water which was boiled contained soluble salts which formed ring shaped deposits during nucleate boiling. At the beginning,

Orell tried this technique using an artificial cylindrical pit. The results indicated that the size of the pits ranged from $23 * 10^{-2}$ to $78 * 10^{-2}$ μm at a temperature difference of 10°C in the presence of a thermal boundary layer of $118 * 10^{-2}$ μm thickness which are in good agreement with the theoretical cavity size range predicted by Hsu [11]. Using this technique, active site density could be obtained up to $15.7 * 10^4$ sites/ m^2 . Furthermore this technique can be used for different fluids in the presence of a highly polished heating surface as long as sufficient salts can be dissolved.

Nail, Vachon and Morehouse [12] used the scanning electron microscope technique to identify the location of active sites over the heating surface which was made from cold rolled, 304 stainless steel. A-C power was controlled so that the first twelve to twenty active sites formed on the heating surface remained on the surface sufficiently long to allow the bubble locator to be positioned over the center of the selected bubbles, the positions of all the centers were recorded and the stainless steel heating surface was removed for study in the scanning electron microscope in order to measure the cavity size. This technique is restricted to low heat flux conditions only.

The high speed camera technique has been used by many investigators in order to study the boiling phenomena. Using this technique the location of the active sites over the heating surface can be determined. Recently, Judd [13]

studied the boiling of dichloromethane (methylene chloride) on a borosilicate glass heating surface coated with a half wave length thickness of stannic oxide, using a high speed camera operating at 4000 frames per second. The location of active sites were obtained for different levels of heat flux and subcooling under atmospheric and subatmospheric pressures. The location of the active sites for saturation conditions under atmospheric pressure obtained by Judd's work is represented in figure (4). This technique was found to be suitable only for organic liquids such as carbon tetrachloride and dichloromethane which would not attack the glass heating surface coating. Photographic studies of water boiling on a metal heating surface cannot be performed by using a high speed camera technique. The boiling of water at atmospheric pressure on a horizontally electrically heated, 1 mm stainless steel sheet, was studied by Sgheiza and Myers [14] using a high speed infrared camera operating at 15 to 60 frames per second. According to the appearance of the temperature contours on the underside of the boiling surface observed with the infrared camera, it was possible to identify the active site locations during boiling. For the boiling of organic liquids on metal surfaces the active site locations can be obtained using the infrared camera. Raad and Myers, [15] studied the boiling of methylene chloride at atmospheric pressure on a metal surface consisting of an electrically heated 1 mm stainless steel sheet. Active nucleation sites were located and counted by photographing

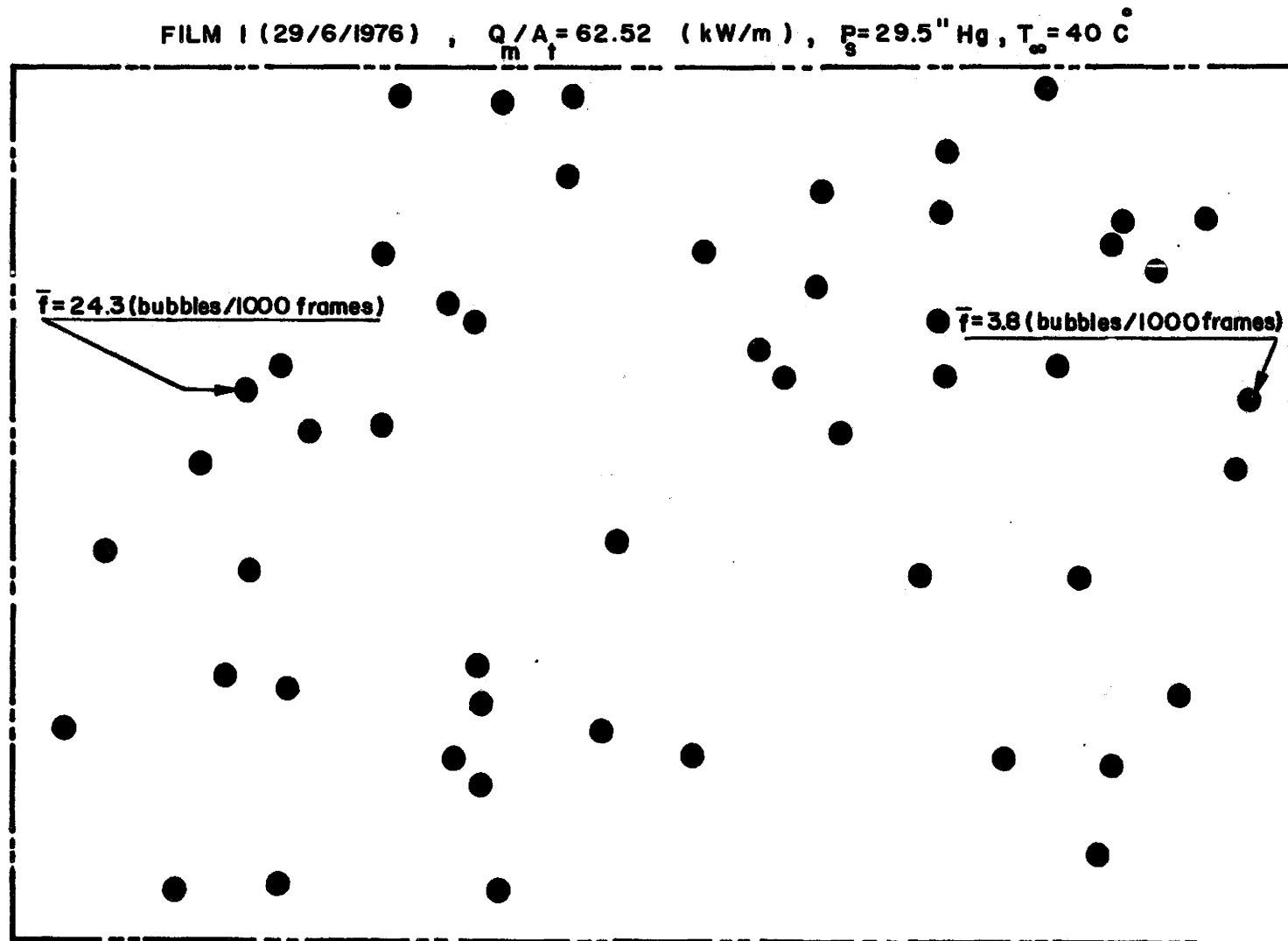


Figure (4). Active Nucleation Site Distribution
According to Judd

changing colour patterns in the liquid crystals that coated the underside of the thin heater for heat fluxes up to 75.7 kW/m^2 .

Finally, the electrical probe technique which is widely used for obtaining information on the flow structure in two phase gas-liquid flows as presented by reference [16] may be used to advantage. The behaviour of a vapour void on a horizontal heating surface which includes the distributions of time-average void fraction and the thickness of the liquid rich layer were studied by Iida and Kobayasi [17] using an electrical probe technique. The conductance probes, which depend for their operation on the fact that the electrical conductivity of a two phase mixture is strongly dependent on the phase distribution can be used for flow regime study, since the electrical conductivity of the vapour phase is significantly different from that of the liquid phase. Consequently the probe technique can be used to identify the active site locations. Recently Sultan and Judd [2] used the bubble detection probe technique to identify the location of the active sites in order to study the spatial distribution of the active sites as well as the bubble flux density. Boiling of water at atmospheric pressure on a single copper surface was performed for different levels of heat flux and different levels of subcooling. The distribution of the active sites at heat flux 166 kW/m^2 and 1.7°C subcooling is presented in figure (5). The influence of changing carrier frequency on the bubble detection probe response is represented

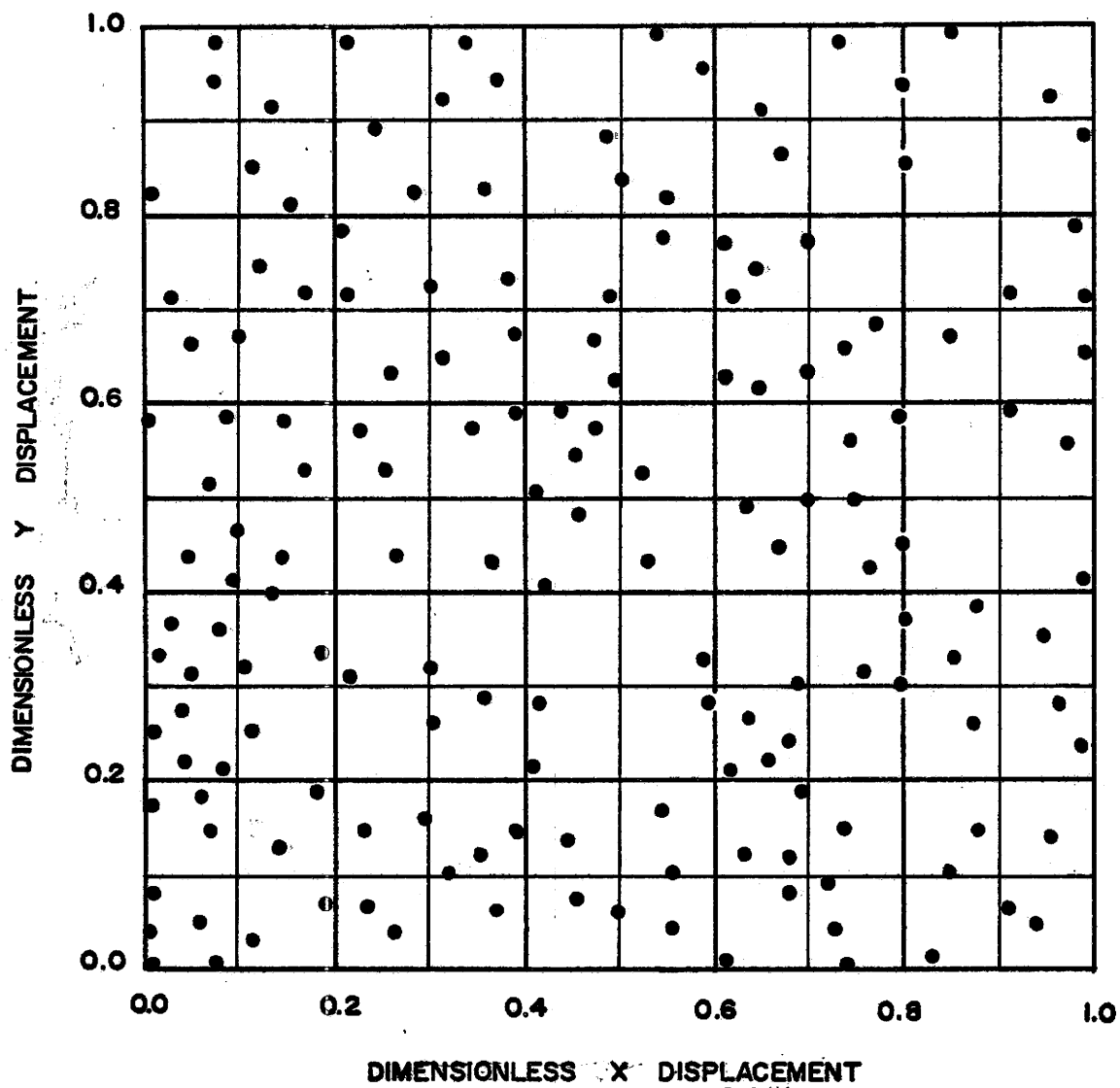


Figure (5). Distribution of Active Nucleation Sites According to Sultan and Judd

in figure (6). More recently Shoukri and Judd [18] studied the effect of the cavity size on the bubble emission frequency. The bubble detection probe was used to determine the locations and the bubble emission frequency as well at different active sites for boiling of water and isopropyl alcohol on a single copper surface having two different surface finishes.

2.3 Interaction of Nucleation Sites in Nucleate Boiling

The only direct reference available for the interaction of nucleation sites is Chekanov [1], who experimentally studied the interaction between two artificial nucleation sites in water boiling at atmospheric pressure. The time elapsed between the start of bubble growth at two neighbouring artificial nucleation sites was obtained using the analysis of the photomultiplier signals corresponding to the formation of bubbles above the surface. The water was boiled on a very thin permalloy plate with 20 μ thickness and dimensions of 1 x 4 cm. Two heated copper rods, 1.4 mm diameter and 4 mm length were located beneath the permalloy plate to act as artificial nucleation centers. The heated rods could be moved relative to each other in order to change the distance between them. Chekanov analysed experimental measurements of the time elapsed between the start of bubble growth at two neighbouring nucleation sites as a random variable using statistical methods and found that the results followed a Gamma

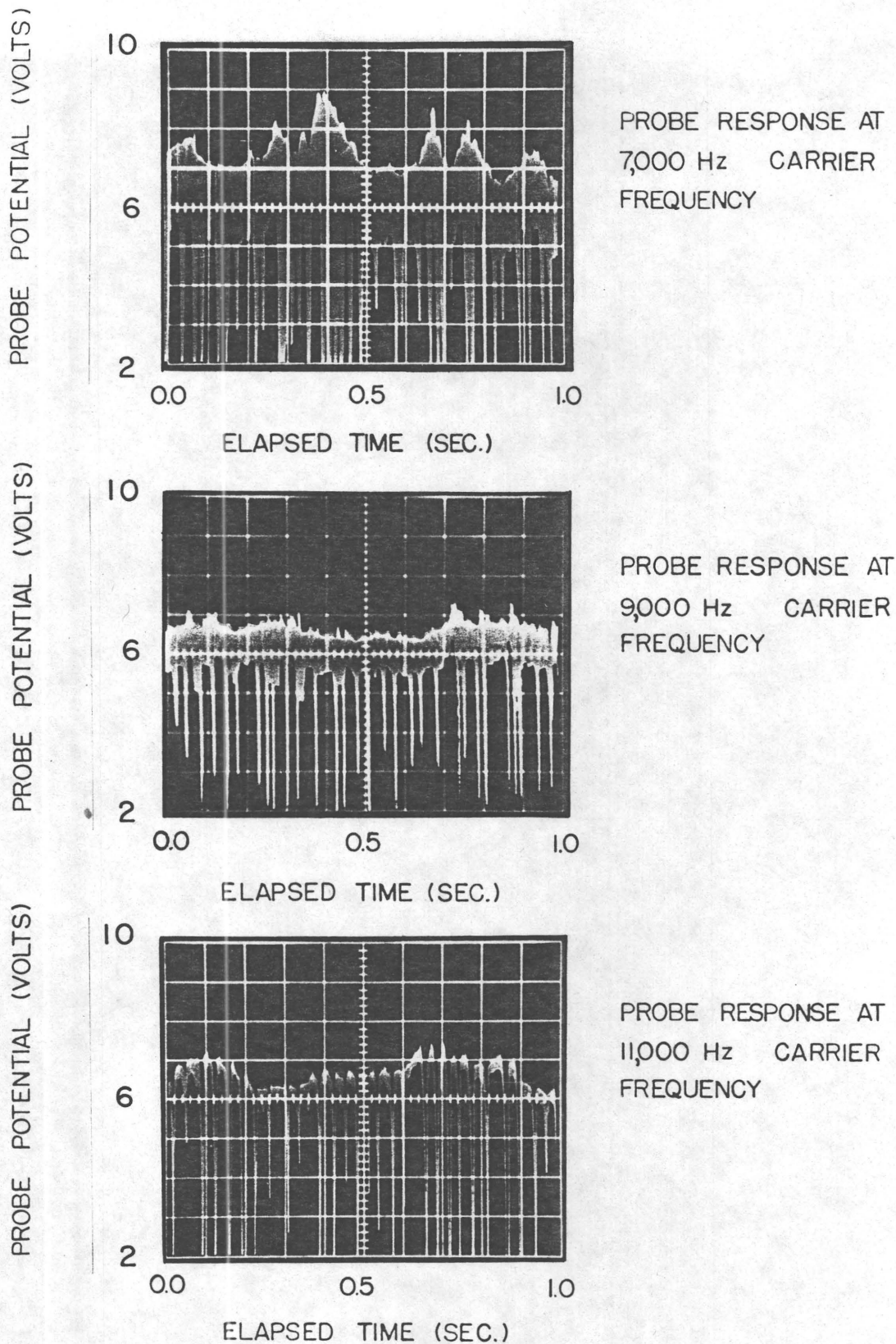


Figure (6). Effect of Carrier Frequency on the Bubble Detection Probe Response

distribution

$$P(\tau) = \frac{\lambda (\lambda \tau)^{\nu-1} e^{-\lambda \tau}}{\Gamma(\nu)}$$

where $P(\tau)$ is the probability density function

ν is the shape parameter

λ is the scaling parameter

Chekanov found the shape parameter ν to be a function of the different spacings as shown in figure (7). At a distance greater than three times the bubble maximum diameter there was "attractive" interaction in which ν was found to be less than unity ($\nu < 1$) and the growth of a bubble on one center enhanced the growth of a bubble on the other. For a distance of less than three times the bubble maximum diameter there was "repulsive" interaction in which ν was found to be greater than unity ($\nu > 1$) and the growth of a bubble on one center inhibited the growth of a bubble on the other. Chekanov postulated that the formation of bubbles affected one another by acoustic action and hydrodynamic mixing. At distances between the two nucleation sites much greater than maximum bubble diameter there were no interactions, probably because the acoustic effect is of little importance under these boiling conditions.

2.4 Bubble Flux Density

The bubble flux density distribution on the heating surface is the indirect source of information about the

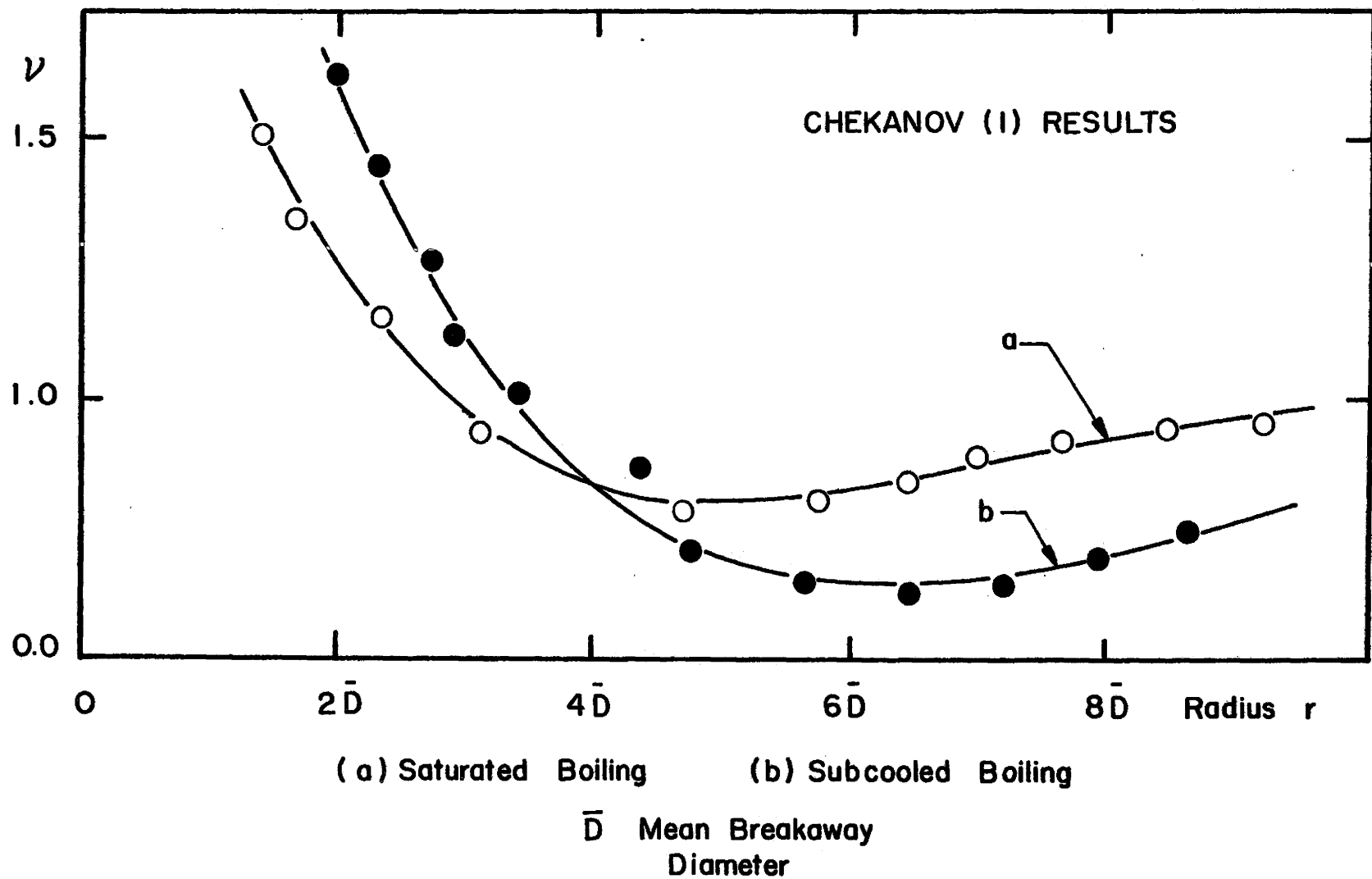
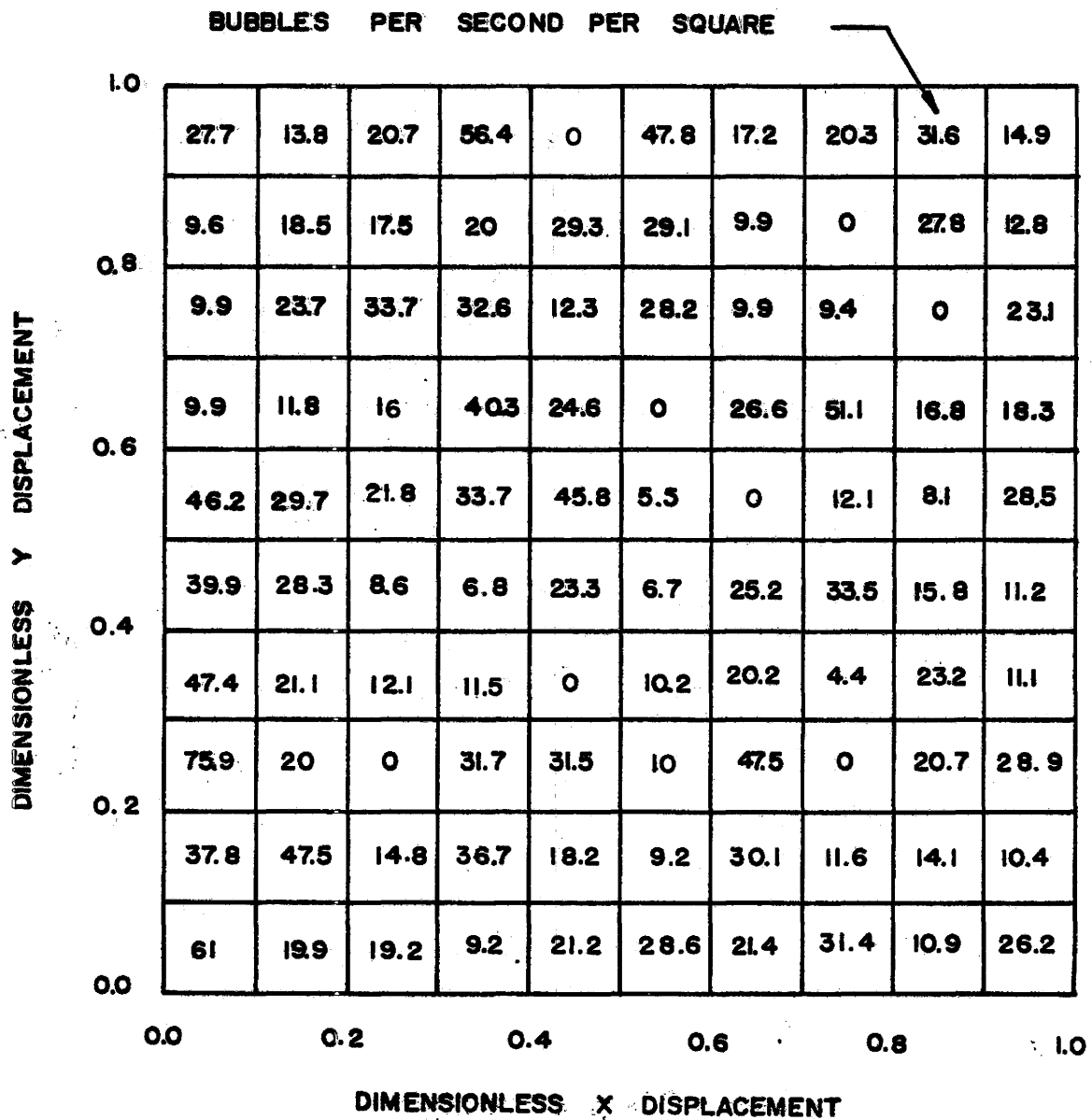


Figure (7). Shape Factor Versus Distance Between Two Nucleation Centers

behaviour of the bubble formation process. The fact that very little bubble flux density data exists may be due to the fact that knowledge of the frequency of vapour bubble emission is not very extensive. Voutsinos [52] studied the influence of heat flux and subcooling upon the bubble flux density. For dichloromethane boiling on a glass surface, Voutsinos showed that the bubble flux density increases with increasing heat flux in agreement with Judd and Hwang [19]. For increasing subcooling Voutsinos' results for the same surface/fluid combination were found to be contrary to Judd and Hwang's results, perhaps because of different methods of computing the average frequency of vapour bubble emission. Recently Sultan and Judd [2] studied the bubble flux density for boiling of water at atmospheric pressure on a single copper surface at different levels of heat flux and subcooling. A typical distribution of bubble flux density is shown in figure (8). The percentage cumulative bubble flux density versus the percentage cumulative area for the heating surface is shown in figure (9). It is seen that the effect of subcooling is quite small but that the effect of heat flux is significant. The bubble flux density was observed to be non-uniformly distributed on the heating surface as shown in figure (9). Consequently, there was a tendency for the bubble flux density distribution to become uniform at high heat flux, in which case ten percent of the area would contribute ten percent of the bubble flux density.

It can be deduced from Sultan and Judd's [2] results that



TEST B1

$$\frac{Q}{A} = 166.0 \quad (\text{KW}/\text{m}^2)$$

$$(T_s - T_\infty) = 1.7 \quad (^\circ\text{C})$$

Figure (8). Distribution of Bubble Flux Density

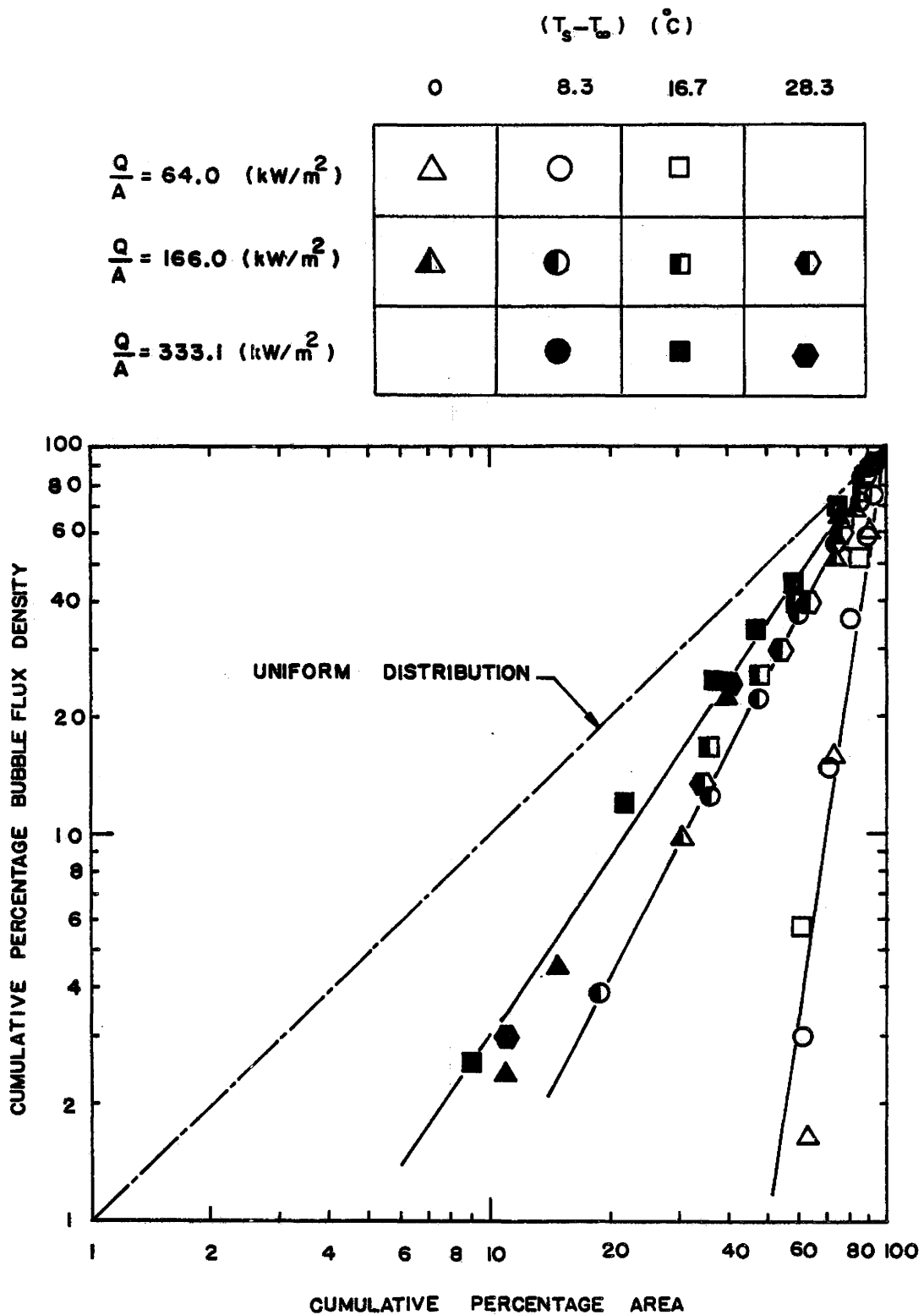


Figure (9). Cumulative Percentage Bubble Flux Density Versus Cumulative Percentage Area

at the lower level of heat flux the bubble flux density must have been distributed in cluster form, perhaps because the formation of bubbles at one nucleation site enhanced the formation of bubbles at surrounding nucleation sites.

CHAPTER 3

EXPERIMENTAL INVESTIGATION

The apparatus used was built by Wiebe [20], in 1970 to measure the liquid temperature distribution perpendicular to the heating surface. The apparatus is capable of:

1. Boiling water up to a maximum heat flux of 470 kW/m^2 .
2. Subcooling the bulk liquid by at least 20°C at the maximum heat flux conditions.
3. Obtaining unidirectional heat flow normal to the boiling surface.

The apparatus was later modified by Sultan [21] to examine the active site distribution and bubble flux density over the heating surface, and in the present study the apparatus was modified once again, changing the bubble detection probe in order to meet the requirements for studying the interaction of the nucleation phenomena at adjacent sites. The modified apparatus used was capable of:

1. Accurately determining the active site locations with the capability of locating them.
2. Accurately determining the distance between the two neighbouring active sites.
3. Allowing the measurement of the time elapsed between the start of bubble growth at two neighbouring active sites.

4. Allowing observation of the bubble formation regions.

3.1.1 Boiler Assembly

The sectional view of the complete boiler assembly is presented in figure (10). The vessel was made from schedule 40 stainless steel pipe, 45.7 cm in length by 20.3 cm inside diameter. Two stainless steel flanges 1.9 cm in thickness were welded on the outside diameter at both ends of the pipe. A stainless steel cover plate 1.3 cm in thickness by 29.2 cm in diameter was attached to the flange at the top end of the vessel with eight cap screws which compressed a rubber gasket between the flange and the cover plate. Two circular sight glass windows 2.5 cm in diameter were located diametrically opposite, on the axis of a high intensity lamp at a level which permitted observation of the two bubble probes over the heating surface.

The heater block was made from a copper cylinder 15.0 cm in diameter reduced to 5.0 cm at the boiling surface. Thirteen "Firerod" cartridge heaters (Watlow Electric Manufacturing Company) with a total power rating of 4000 Watts were installed in symmetrically located holes in the base of the copper heater. A stainless steel skirt 0.3 cm in thickness was brazed flush with the top of the copper block to provide a continuous extension of the boiling surface. A stainless steel flange welded inside the vessel supported the skirt and positioned the heater block within the vessel. Eight cap screws served to compress an "O" ring seal which provided

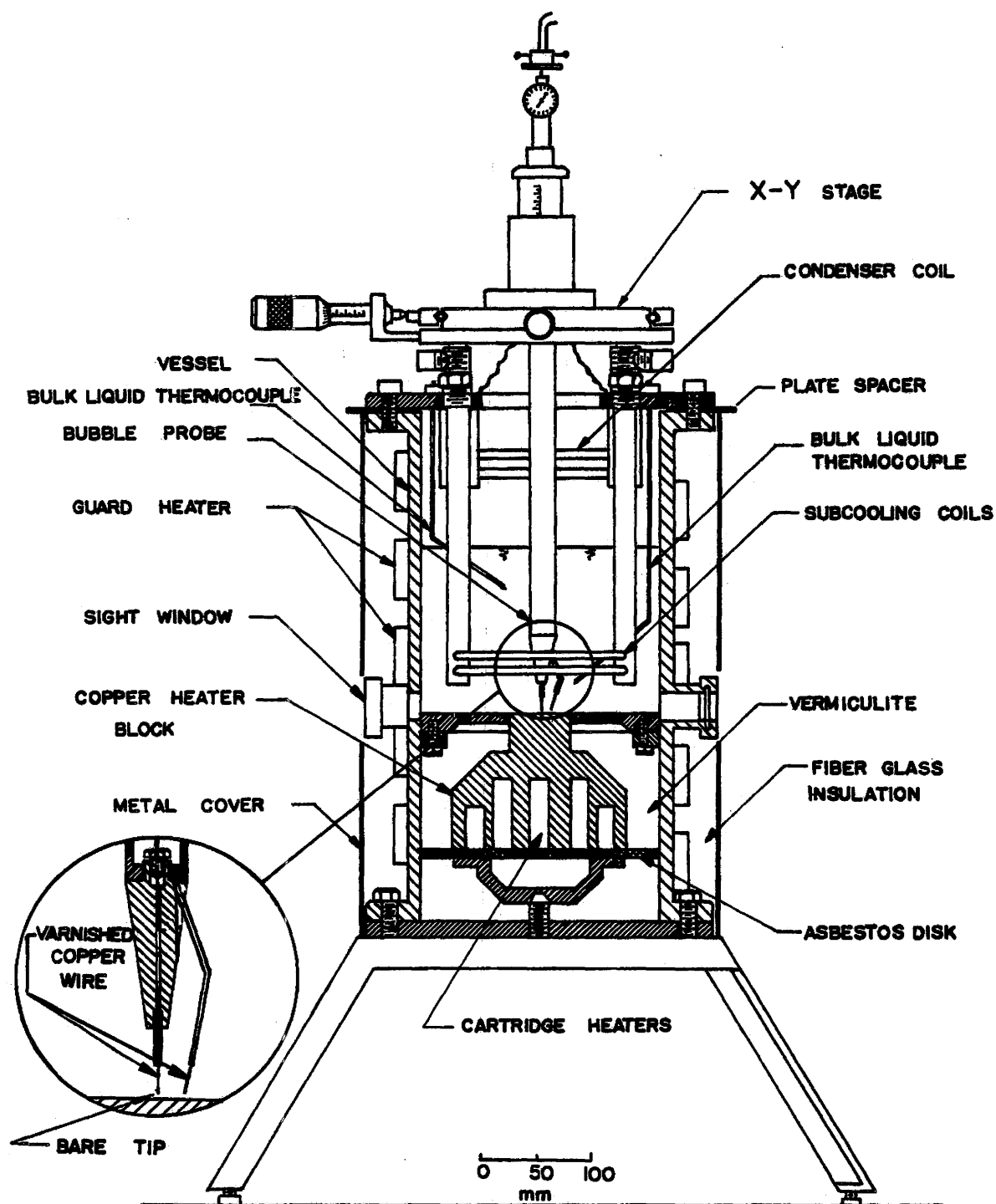


Figure (10). Section of Boiler Vessel

a water tight joint at the flange.

The present investigation required that the sub-cooling in the bulk liquid be varied. This condition was satisfied by using a single pass heat exchanger comprised of eight 0.5 cm diameter stainless steel tubes, semi-circular in shape, brazed between two stainless steel pipes and located 2.5 cm from the skirt to provide the bulk subcooling. Appendix (B) shows the locations of the two thermocouples used to measure the bulk liquid temperature. To condense the vapour which formed at the free surface of water, a single pass condenser comprised of two 0.5 cm diameter of stainless steel tubes arranged in a semi-circular form between two stainless steel pipes was positioned 2.5 cm below the cover plate. The cooling water flow rate through each of the coils was controlled by needle valves. The vessel was fitted with a vent located on the cover plate to allow any non-condensed vapour to escape to the atmosphere and also to keep the applied pressure at the atmospheric level.

To minimize the heat flow in the radial direction through the heater block, vermiculite was located between the heater block and the vessel. Furthermore, to minimize the heat loss from the outer wall of the vessel, 3.6 m of 7.5 cm wide heating tape (Electrothermal Engineering Limited, Model HT 362) with the capacity of 500 Watts was helically wrapped around the vessel to serve as a guard heater. Fiberglass insulation 3.8 cm in thickness covered the guard heater and the vessel, which was then covered with light

gauge galvanized steel sheet. An asbestos disc was attached to the bottom of the heater block to minimize the heat loss in the downward direction.

The bubble probe assembly described in Appendix (G) was mounted on a vertical positioning mechanism to control the vertical distance between probe tips and the heating surface.

Photographs showing three different views of the test assembly and associated equipment are presented in figures (11), (12) and (13).

3.1.2 Temperature Measurement System

Chromel constantan thermocouples were selected because the EMF characteristic for this combination of materials is large, approximately $36 \mu \text{ Volts}/^{\circ}\text{F}$. Two 36 gauge nylon insulated chromel constantan thermocouples inserted in stainless steel tubes were used to measure the bulk liquid temperature. Both thermocouples were introduced into the vessel through "Swagelok" fittings in the cover plate at 5.0 cm radius from the vessel centerline and were located at levels of 5.0 cm and 10.0 cm respectively above the heating surface. Eleven additional thermocouples were used to measure the temperature at various other locations. To determine the axial temperature gradient in the copper block near the heating surface, three thermocouples A, B and C as shown in figure (14) were inserted in the block centerline at approximately 0.6 cm intervals from the heating surface. The radial temperature distribution in

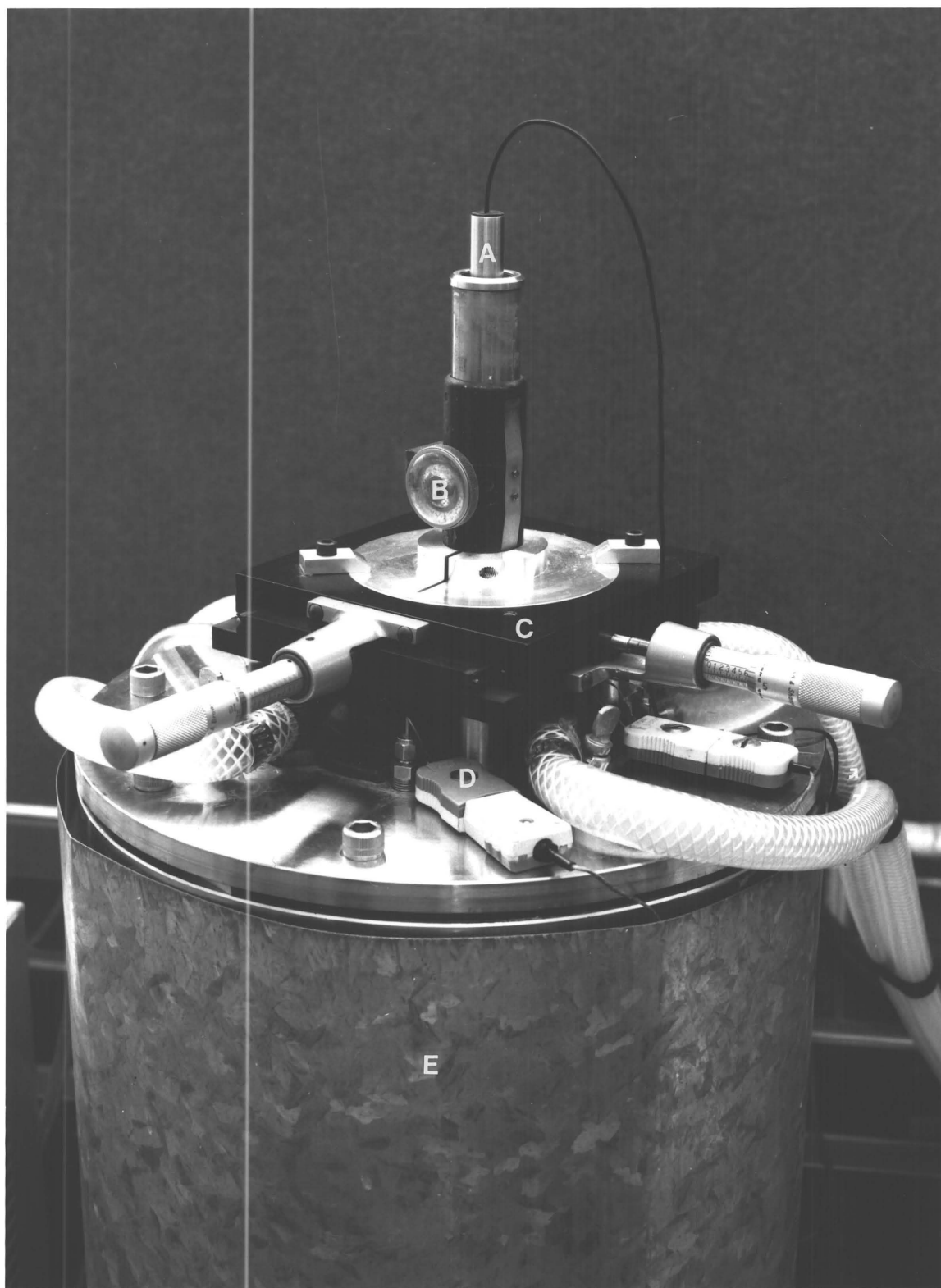


Figure (11) Nucleation Site Location System



Figure (12) Experimental Arrangement

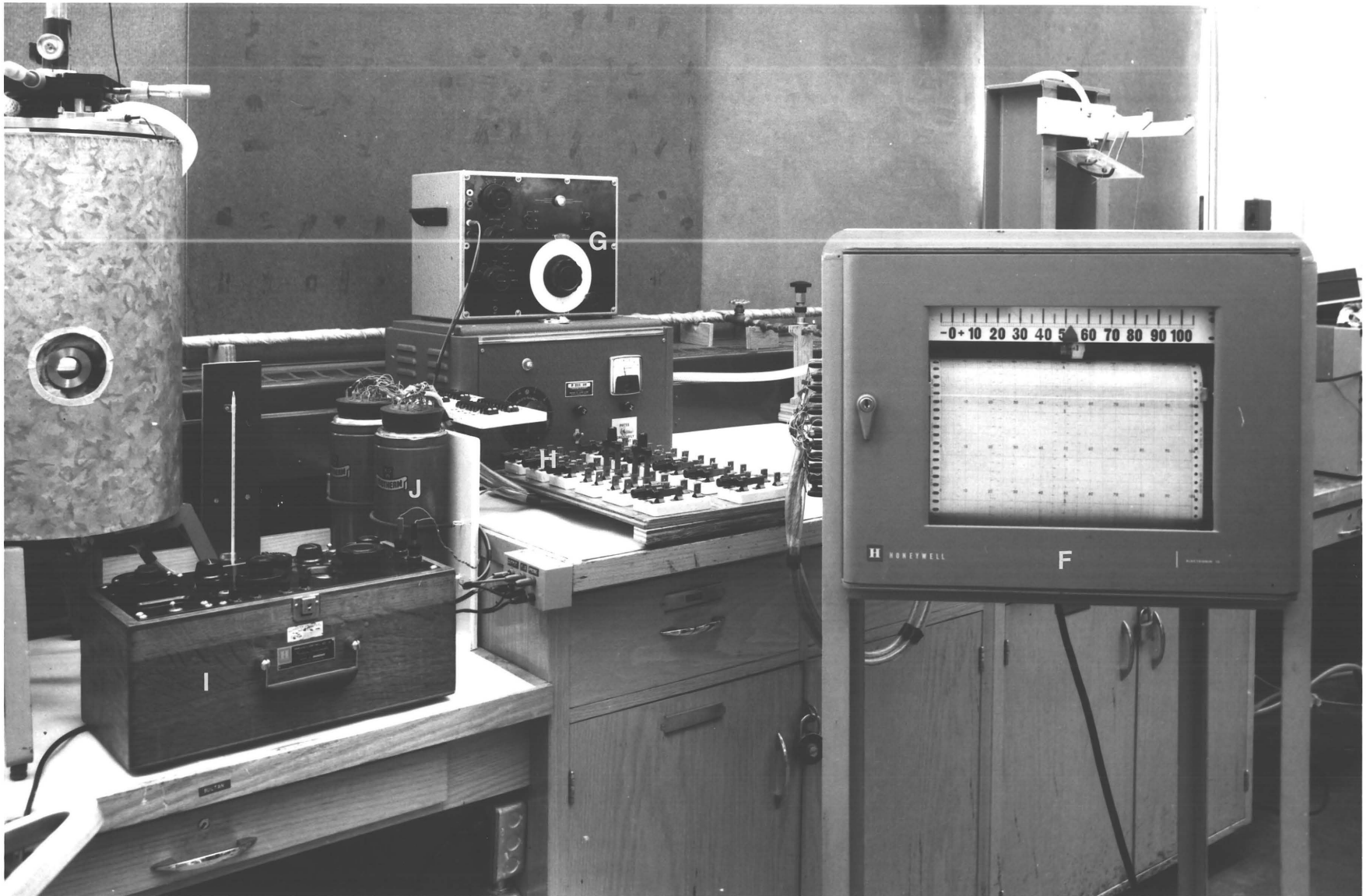


Figure (13) Experimental Arrangement

LEGEND

A	Bubble Detection Probe Assembly
B	Probe Vertical Positioning Mechanism
C	X-Y Stage
D	Bulk Liquid Thermocouple Connectors
E	Boiling Vessel
F	Thermocouple Recorder
G	Function Generator
H	Thermocouple Switches
I	Potentiometer
J	Ice Bath
K	Sight Glass Window
L	Power Supply
M	Oscilloscope
N	Signal Conditioning Unit
O	Input Power Measurement
P	Dial Indicator
Q	Telescope
R	Digital Computer DECLAB 11/03

the neck of the copper block was measured by three thermocouples D, E and F as shown in figure (14) located at 0.6 cm, 1.3 cm and 1.9 cm radii from the axis in the plane perpendicular to the axis 1.3 cm below the heating surface which included thermocouple B as well. These six thermocouples were constructed of 30 gauge thermocouple material as shown in figure (15). Bare 30 gauge thermocouple wire was threaded through lengths of 0.16 cm diameter two-hole ceramic insulators. A drop of Epoxy cement was used to hold the wires in place in the insulator. A small lipped collar of brass was cemented to the ceramic insulator in such a position that when the thermocouple was fully inserted into the positioning hole, the sensing junction was pressed firmly against the bottom of the hole. Three spring loaded wires were used to hold the six thermocouple assemblies snugly in place. Another thermocouple was located in the center of the cartridge heater cluster to provide a check on the maximum block temperature. Two more thermocouples were placed at different radii one on the copper block, the other on the vessel wall in the vermiculate insulation in order to check on radial heat loss from the copper block and two thermocouples were soldered to the underside of the skirt in 0.3 cm deep holes at 4.5 cm and 5.7 cm radii respectively. A typical thermocouple circuit is shown in figure (16). To conserve chromel constantan wire, a transition was made to single strand nylon insulated thermocouple grade copper wire at ice baths in all thermocouple

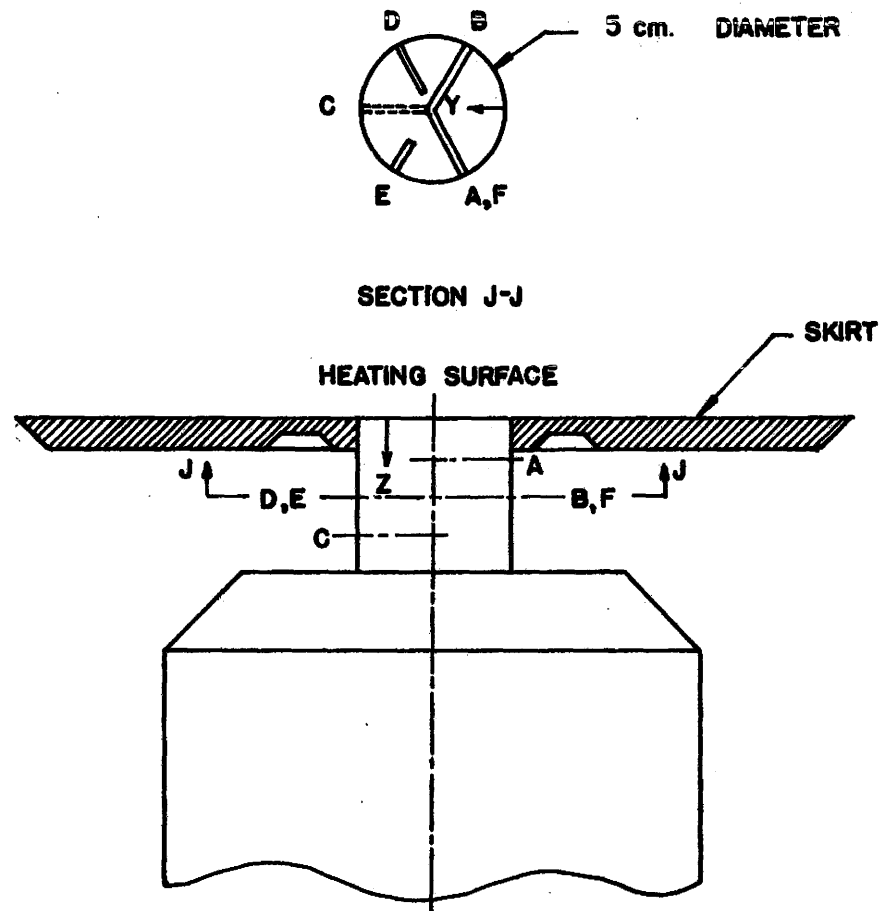


Figure (14). Thermocouple Locations

TABLE (1)

**LOCATION OF THERMOCOUPLES IN THE NECK
OF THE COPPER HEATING BLOCK**

HOLE	HOLE DEPTH Y cm	VERTICAL DISTANCE Z cm
A	2.5	0.6
B	2.5	1.2
C	2.5	1.8
D	1.8	1.2
E	1.2	1.2
F	0.6	1.2

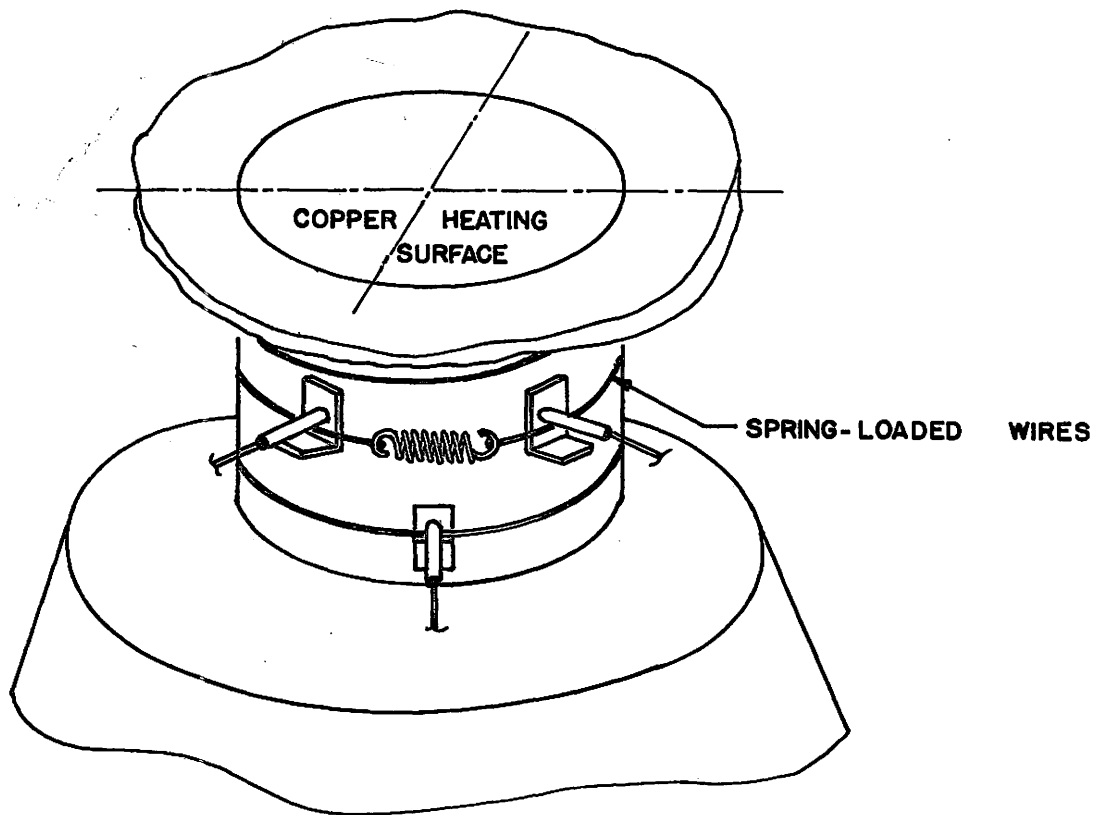
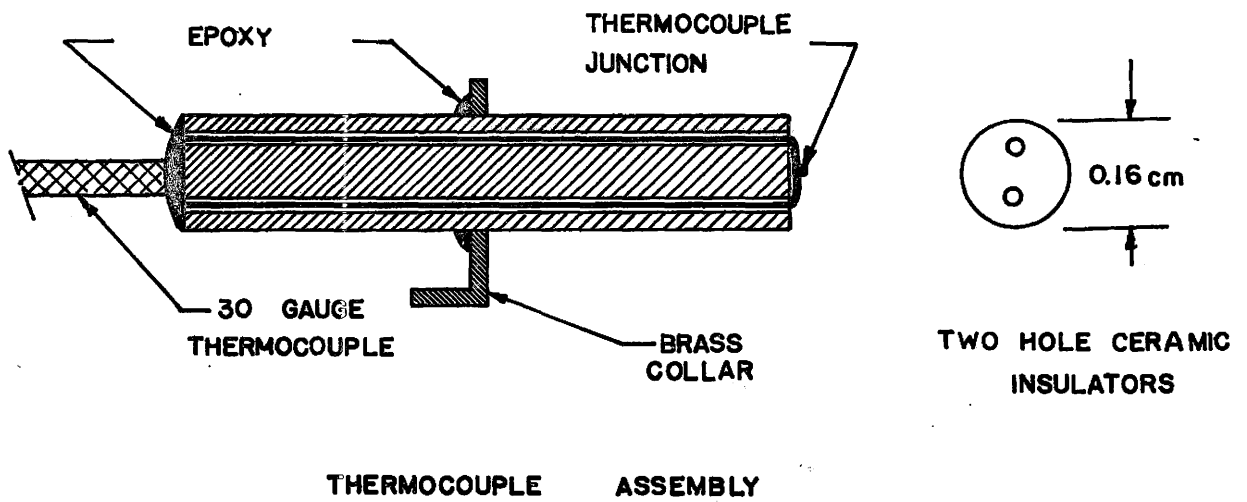


Figure (15). Thermocouple Assembly

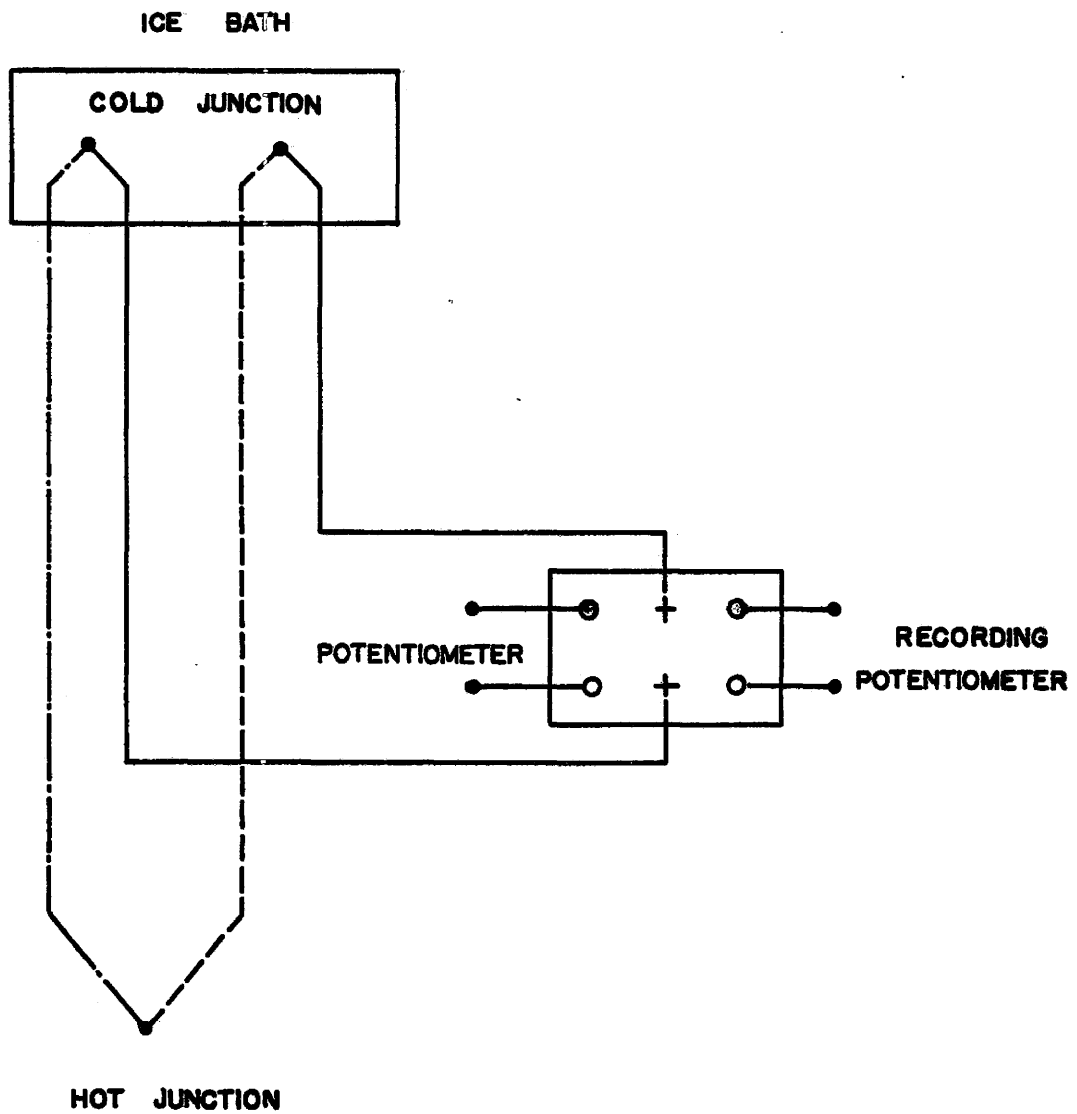


Figure (16). Thermocouple Circuit

circuits. The leads were connected to the center post of copper knife switches which directed the output in either of two directions. The first direction connected to the twelve channel Honeywell recorder (Model #15303836) capable of reading with an accuracy of ± 0.1 millivolt. The second direction connected to a single channel manual balanced Honeywell potentiometer (Model #2745) capable of reading with an accuracy of ± 0.01 millivolt. Figure (17) shows the thermocouple switching arrangement in both directions. In one direction, ten thermocouples were connected to ten channels of the twelve channel recorder. In the other direction, fourteen terminals were connected in parallel to allow connection to the manually balanced potentiometer to obtain the reading of each thermocouple individually.

3.1.3 Power Circuitry and Measurement

Two separate circuits were used to power the apparatus. The first circuit controlled the block heaters as shown in figure (18.a). The line voltage was applied directly to a 110 Volt, 2.1 maximum KVA (Superior Electric Company, type 226T) "Powerstat" variable output autotransformer, which controlled the power input to the thirteen "Firerod" block heaters. A wattmeter was used to measure the power dissipated in the heaters which were connected in parallel. A 10 Ampere fuse was used as indicated for protection and an indication lamp was installed in the circuit to show that the line voltage was applied to the primary windings of the "Powerstat".

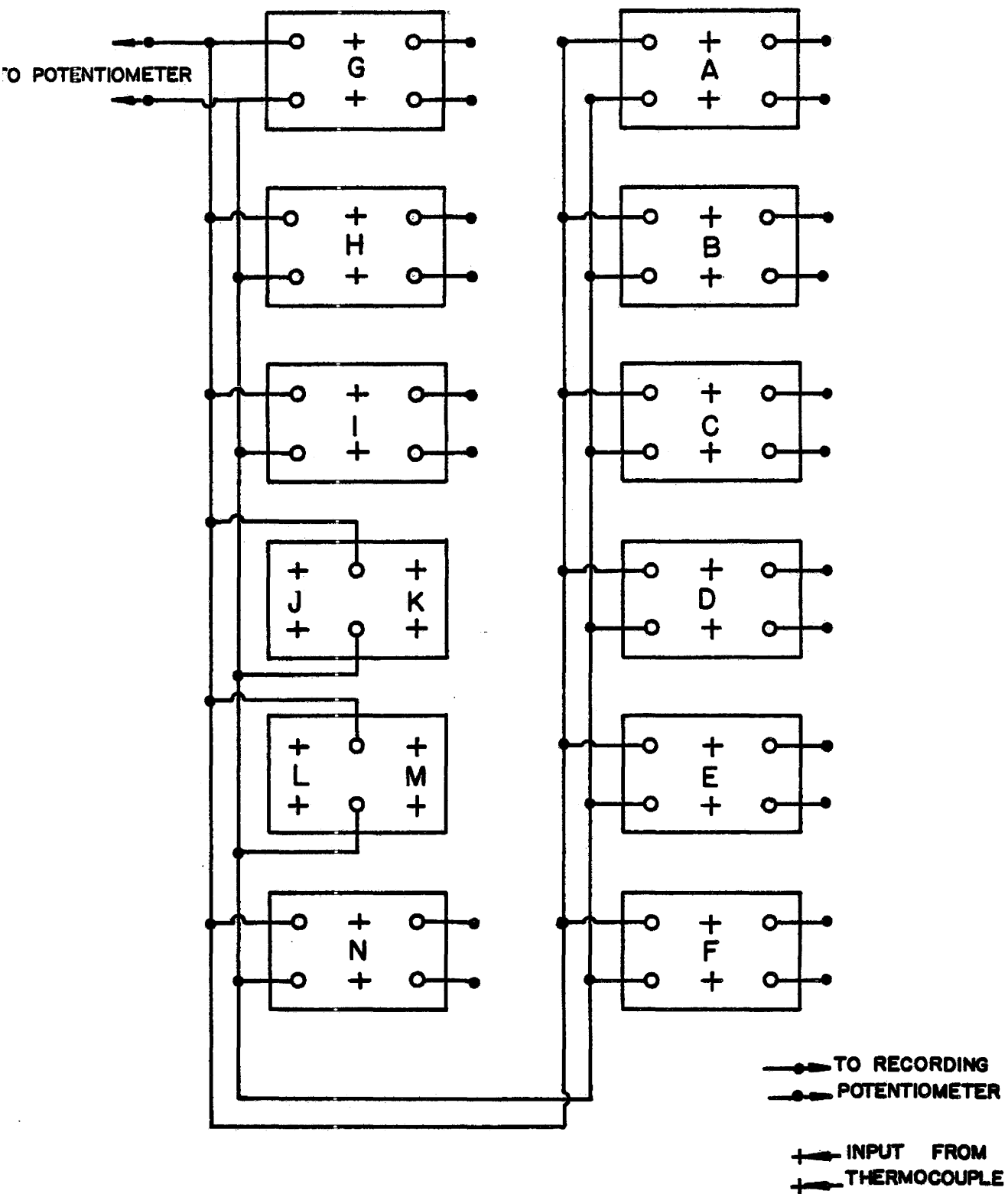
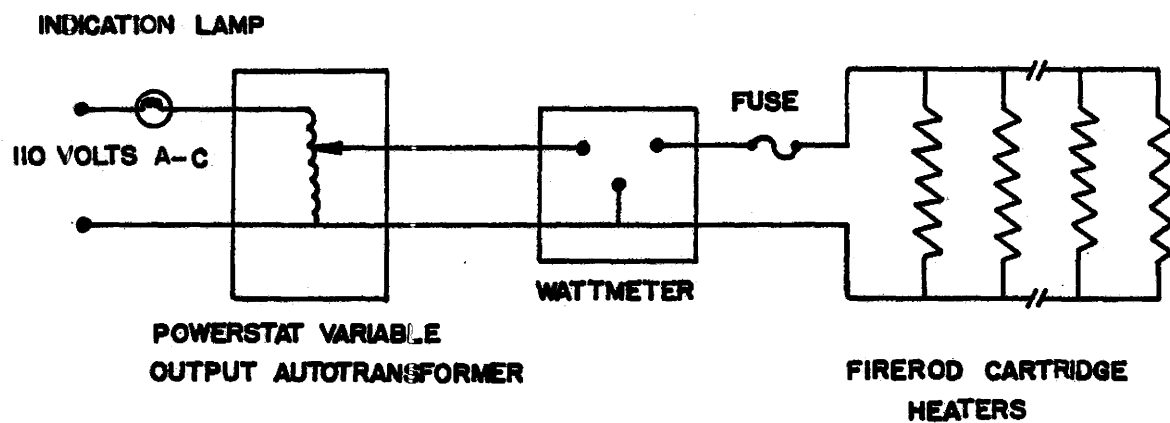
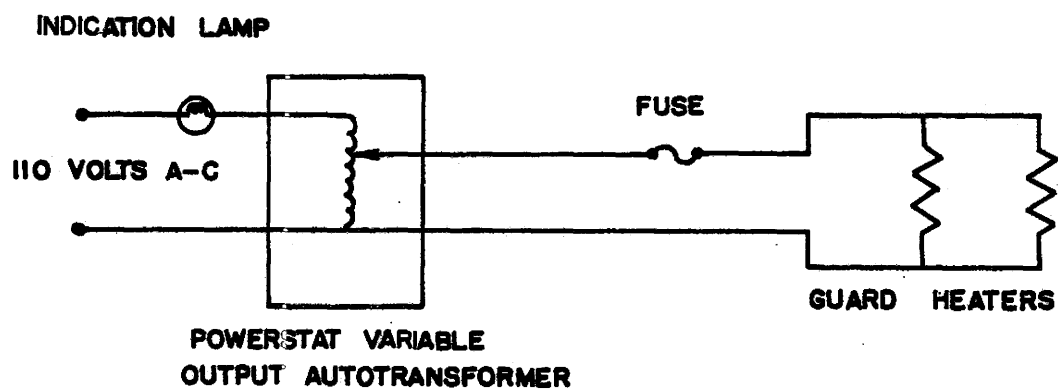


Figure (17). Thermocouple Switching Arrangement



BLOCK HEATER ELECTRIC CIRCUIT
(a)



GUARD HEATER ELECTRIC CIRCUIT
(b)

Figure (18). Power Circuit Diagram

The second circuit controlled guard heaters as shown in figure (18.b). The line voltage was applied directly to a 110 Volt, 1.4 KVA "Powerstat" variable output autotransformer, which controlled the power input to the guard heaters. A 3 Ampere fuse was used as indicated also for protection and an indication lamp was installed in the circuit to show that the line voltage was applied to the guard heaters. A wattmeter was connected before the commencement of testing and a graph representing the relationship between the output from the autotransformer and dial indicator was obtained. Afterward, during the test program, the wattmeter was disconnected from electric circuit of the guard heaters, and the graph was used while adjusting the power setting of the guard heaters.

3.1.4 Bubble Detection Probes

Electrical probes are widely used for obtaining information on the flow structure in two-phase gas-liquid flows as indicated in reference [17]. The conductance probes, which depend for their operation on the fact that the electrical conductivity of a two phase mixture is strongly dependent on the phase distribution, can be used for flow regime detection, void fraction measurement, bubble and drop size determination and film thickness measurement, since the electrical conductivity of the vapour phase is significantly different from that of the liquid phase.

Two electrical probes were used in the present investigation as shown in figure (19) to determine the

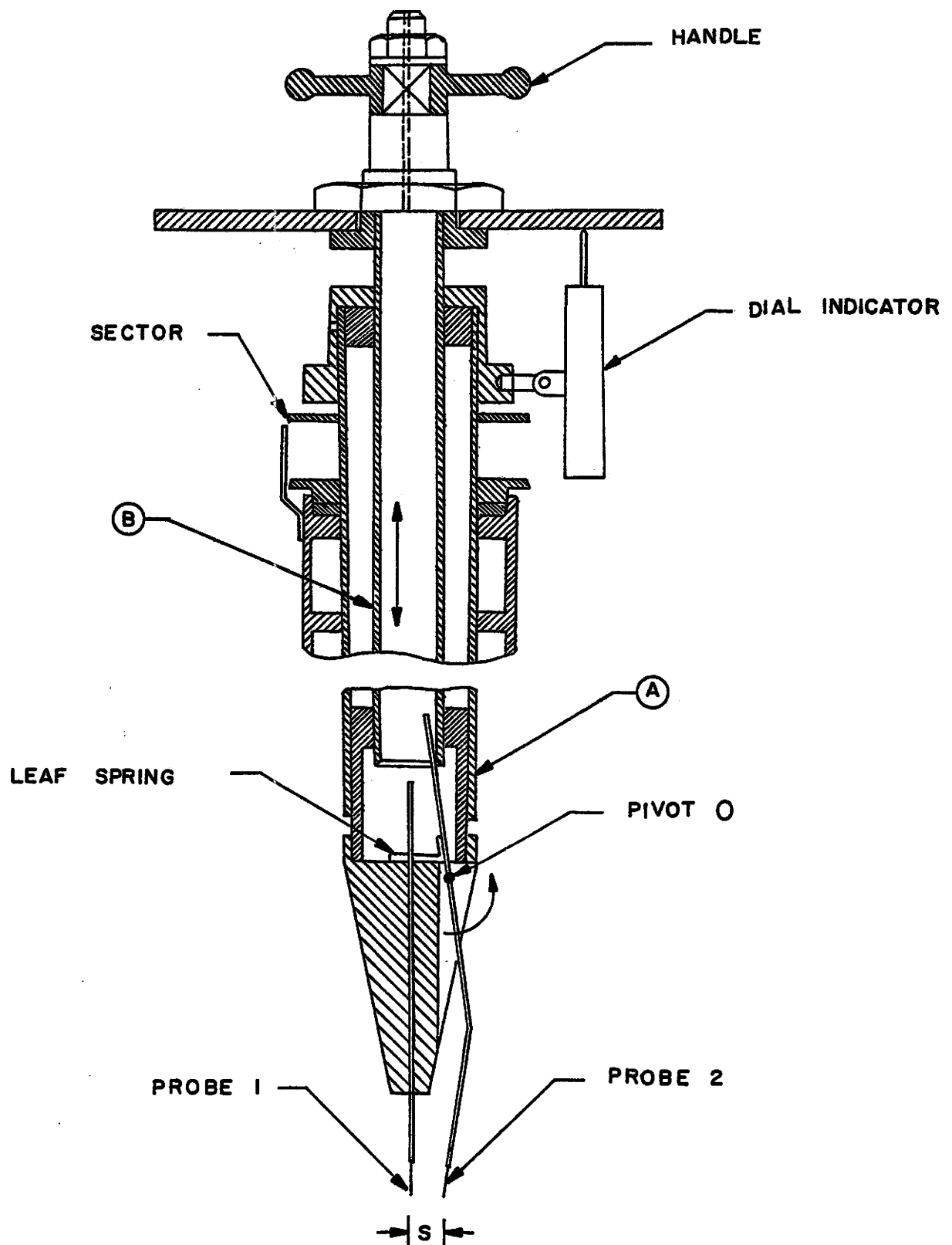


Figure (19). Bubble Detection Probe Assembly

horizontal distance between the two neighbouring active sites and also to obtain the time elapsed between the start of bubble growth at the same active sites.

The tip of each probe represents one electrode while the other electrode is the boiling surface itself. In spite of the fact that direct current excitation might seem easier to control, electrochemical phenomena occur at the electrodes which interferes with the measurement of conductivity. Therefore, alternating current excitation was used instead. Appendix (G) presents design details of the bubble detection probe assembly.

A schematic diagram of the electric circuit designed to obtain the output signal for one probe is shown in figure (20). A function generator, Phillips model Z906069, capable of generating stable signals up to 11000 Hz was used to generate a high frequency carrier signal which was modulated by low frequency signals from the probes. The modulated signals were detected and filtered through a low pass filter and then the two output signals were amplified. Figure (21.a) which represents typical probe response at some considerable distance from the nucleation site, shows that there was a bridge of water between the bubble detection probe and the heating surface. The conductance of the medium within the probe-heating surface gap decreases as vapour is generated and thus, figure (21.b) shows the probe response at a horizontal distance of approximately 0.25 mm from the nucleation site which yielded the signal shown in figure (21.c). The observa-

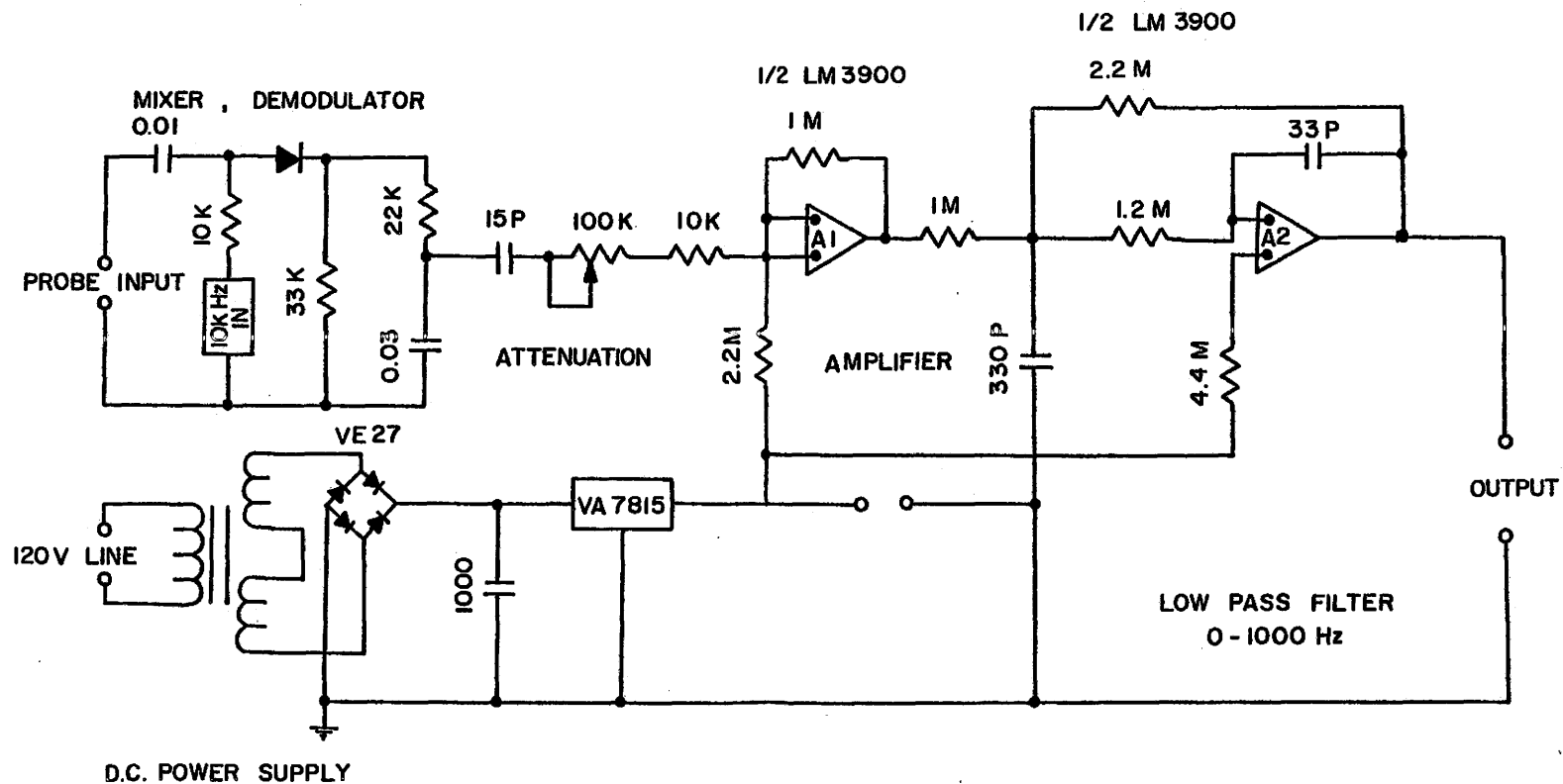


Figure (20). Signal Conditioning Unit (One Channel)

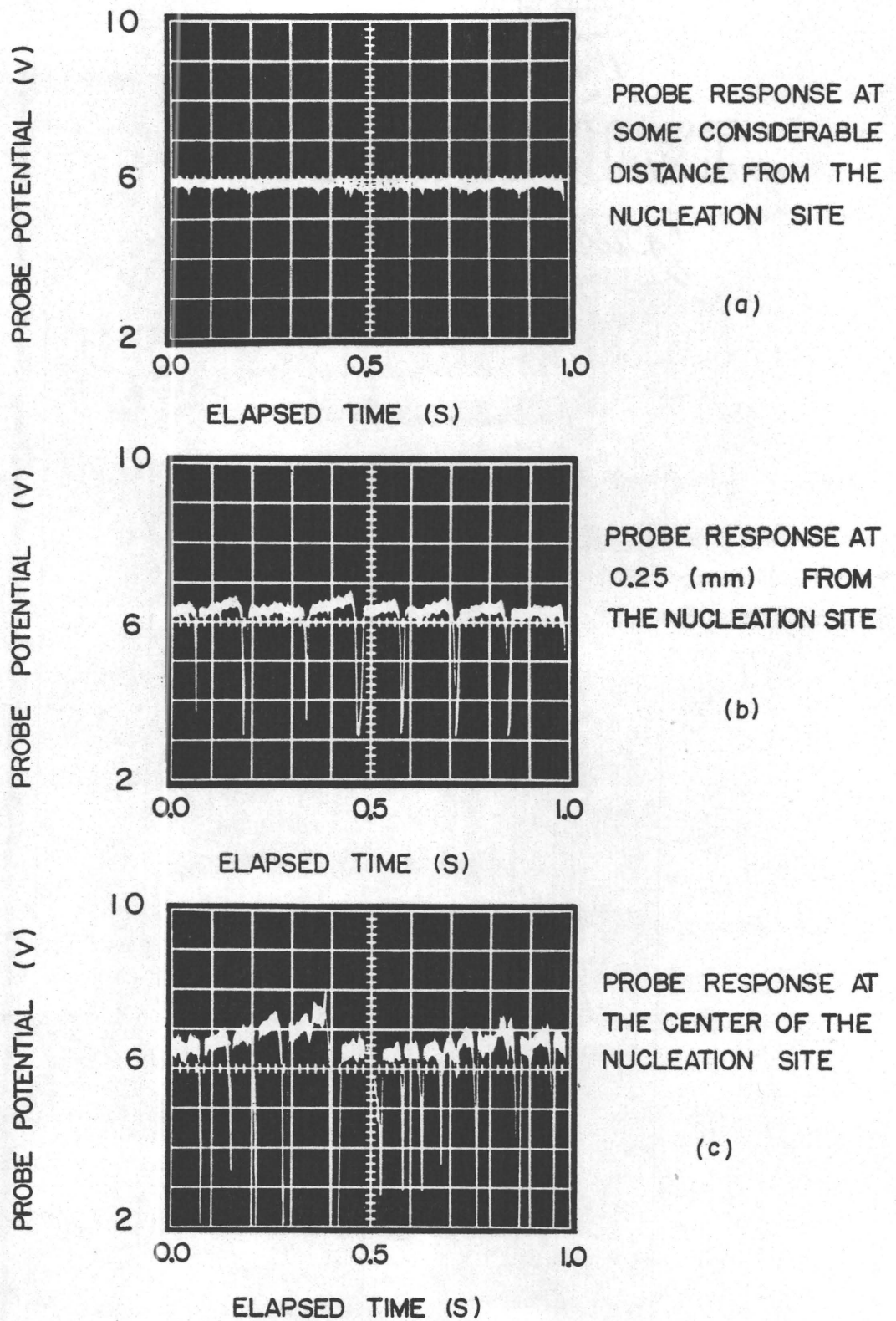


Figure (21). Influence of Probe Displacement from Nucleation Site

tion of "strong" fluctuations identified the location of the active site.

3.1.5 Nucleation Sites Locating System

An "X-Y Stage" provided with two micrometers capable of reading $\pm 2.5 \times 10^{-3}$ mm was fixed to the cover plate on four supports. The stage provided a controlled and accurate travel of the bubble probe assembly in two normal directions. The bubble probe assembly described in Appendix (G) was mounted on a vertical positioning mechanism to control the vertical distance between probe tips and the heating surface.

A telescope was designed as shown in figure (22) with 10 cm equivalent focal length. The telescope was mounted at the top of the vessel to enable fine adjustment of the probes over the active sites when the distance between them was very small.

3.2 Test Conditions

The experimental part of the present investigation was performed for water boiling at atmospheric pressure on a single copper heating surface. Two different levels of heat flux were investigated. For both the lower level of heat flux (92.11 kW/m^2) and the higher level of heat flux (192.11 kW/m^2), two different levels of subcooling ($0, 7.5^\circ\text{C}$) were studied. For the higher level of heat flux (192.11 kW/m^2), different sets of active sites were studied individually at each level of subcooling, each set consisting of one active

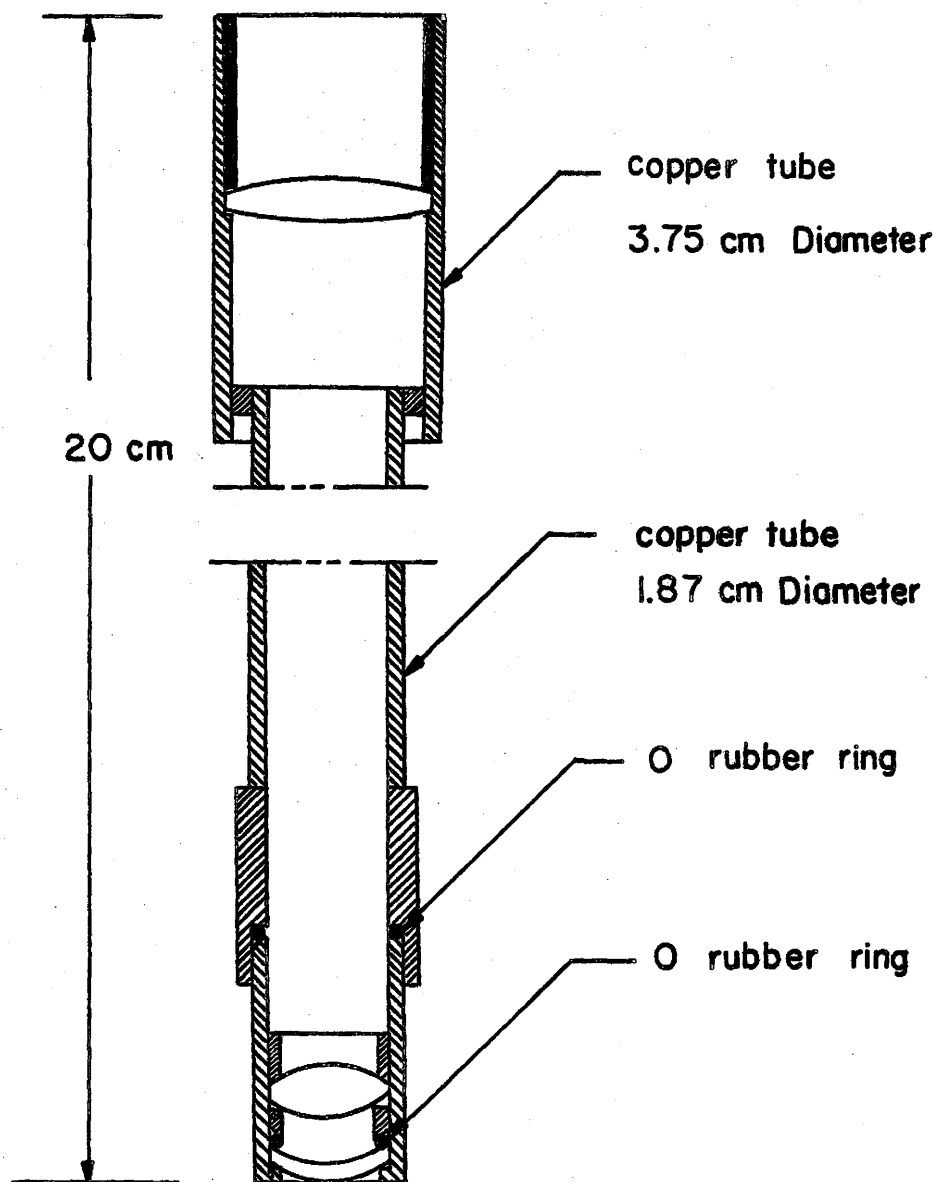


Figure (22). Telescope

site and its surrounding active sites at various distances (S_1, S_2, \dots). The separating distances S were varied from 2.5 mm up to 6 mm. For the lower level of heat flux one set of active sites was studied at each level of subcooling.

A single additional set consisting of an active site and its surrounding active sites was studied in detail at the lower level of heat flux (92.21 kW/m^2) at three different levels of subcooling (0, 6.5, 12°C).

It was experimentally difficult to distinguish the location of active sites over the heating surface due to the large number of active sites present for heat flux levels greater than 192.11 kW/m^2 or due to the decrease of bubble departure diameter for levels of subcooling greater than 12°C .

The nominal values of the various parameters investigated in the experimental tests described above are listed in Table (2) which follows.

3.3 Test Procedures

The vessel was filled approximately to a depth of 15 cm with deionized distilled water containing 0.1 gm of salt/litre. At the beginning of each test, the level of water inside the vessel was checked to confirm the appropriate water level. The cooling water valves which were used to control the flow rate to the subcooling and vapour condenser coils were completely closed. The high intensity lamp, the signal generator, the oscilloscope and the signal conditioning units were turned on. The signal generator output was adjusted

TABLE (2)
NOMINAL VALUES OF TEST CONDITIONS

Set No.	Heat Flux Q/A (kW/m ²)	Subcooling ($T_s - T_\infty$) °C
A1	192.11	0.0
A2	192.11	0.0
A3	192.11	0.0
A4	192.11	0.0
B1	192.11	7.5
B2	192.11	7.5
B3	192.11	7.5
B4	192.11	7.5
C	92.21	0.0
D	92.21	7.5
E	92.21	0
F	92.21	6.5
G	92.21	12

to 11 kHz and 10 Volts. The oscilloscope time scale was adjusted to 0.05 second/division and voltage scale to 1.0 Volt/division. The amplifiers located in the signal conditioning units were set to the lowest amplification values. The bubble detection probe assembly with a separation distance S equal to zero was lowered until the tips came in contact with the heating surface, after which it was raised a very small distance. The gap between the tips of the bubble detection probes and the heating surface was maintained at approximately 0.25 mm. The X-Y stage was used to move the bubble detection probe assembly in different directions to check that there was no contact between the probe tips and the heating surface.

A copper block heater setting of approximately 470 kW/m² was established to heat up the boiler assembly quickly. In all the tests, the guard heaters were set to yield a heat input of 125 Watts. All the thermocouples were switched in the direction of the recorder after which the recorder was turned on. A warm up time of approximately two hours was allowed to elapse in order to achieve steady state conditions, and ensure that the nucleation sites were properly activated at the beginning of each test, after which the heat input was reduced to the desired level. Appendix (A) shows how the rate of heat transfer was calculated. Two hours were required for the system to regain steady state after a change in heat flux or subcooling took place. The attainment of thermal equilibrium was indicated by invariant measurements of the different

thermocouples which were located at different places in the boiler assembly. It was found that the water bulk temperature was sensitive to the vapour condenser and the subcooling systems especially at lower level of heat flux. Consequently, care was taken to set the cooling water flow rate to minimize the interdependence. Once conditions had attained steady state, the individual temperature readings were measured by the manually balanced potentiometer. The individual temperatures were measured twice, once at the beginning and again at the end of each test. The average of each set of measurements was recorded. The reading of the barometric pressure was obtained in order to compute the saturation temperature of the water corresponding to the atmospheric pressure.

In order to place the first probe on an active site, the X-Y stage was used as indicated below. The Y micrometer was fixed at one position and the X micrometer was moved very slowly until a significant deflection in the signal appeared in the first channel of the oscilloscope screen. X and Y micrometers were moved very small increments in both directions until a strong deflection in the signal appeared. The second bubble detection probe was moved horizontally relative to the first probe, establishing a small separation distance S by advancing the mechanism as described in Appendix (G) after which the second probe was moved along the periphery of circular with a radius S until another active site was encountered.

The separating distance S between the probes was equal to the distance between the two bubble centers when a strong signal appeared on the second channel of the oscilloscope screen. Similarly other surrounding active site locations were determined. The distance separating the probe tips was measured after each test with an optical comparator to a precision of $\pm 2.5 \times 10^{-3}$ mm in order to obtain an accurate value for the separating distance S .

As the signals from the two probes were transmitted to the oscilloscope, the signals were also transmitted to the DECLAB 11/03 digital computer. The process of digitizing consists of converting continuous data into discrete data numbers. For each signal, a 1000 value data sample was stored in the digital computer memory for subsequent analysis to calculate the time elapsed between the start of bubble growth at two neighbouring active sites using cross-spectral density function analysis and cross-correlation function coefficient analysis. The experiment was repeated for the same test conditions and each time a new set of 1000 values for each signal was stored in the computer memory for similar analysis. The signals were assumed stationary and consecutive cumulative averages for the power spectrum, amplitude and phase of the cross-spectrum and the cross-correlation function coefficient were taken until invariant distinct peaks were observed.

CHAPTER 4

STATISTICAL SIGNAL PROCESSING

The following chapter describes the methods used in calculating the time elapsed between the start of bubble growth at two neighbouring active sites. The first method was based upon the analysis of the cross-spectral density function and the second method was involved with analysis of the cross-correlation function coefficient. As mentioned previously in Chapter 3, the signals from the two probes were transmitted to an oscilloscope in order to assist in locating the probes over two neighbouring active sites. At the same time the signals were transmitted to the DECLAB 11/03 digital computer for subsequent analysis.

4.1 Digitizing of Continuous Data

The computer signal processing consisted of digitizing each of the two continuous signals depicted in figure (23) into discrete numbers and arranging them into consecutive records. An illustration of equispaced sampling that converts continuous data into discrete data is shown in figure (24).

The sampling interval (h) for both signals was chosen such that

$$h = 1/2 f_c \quad (4.1)$$

where f_c is the cutoff frequency.

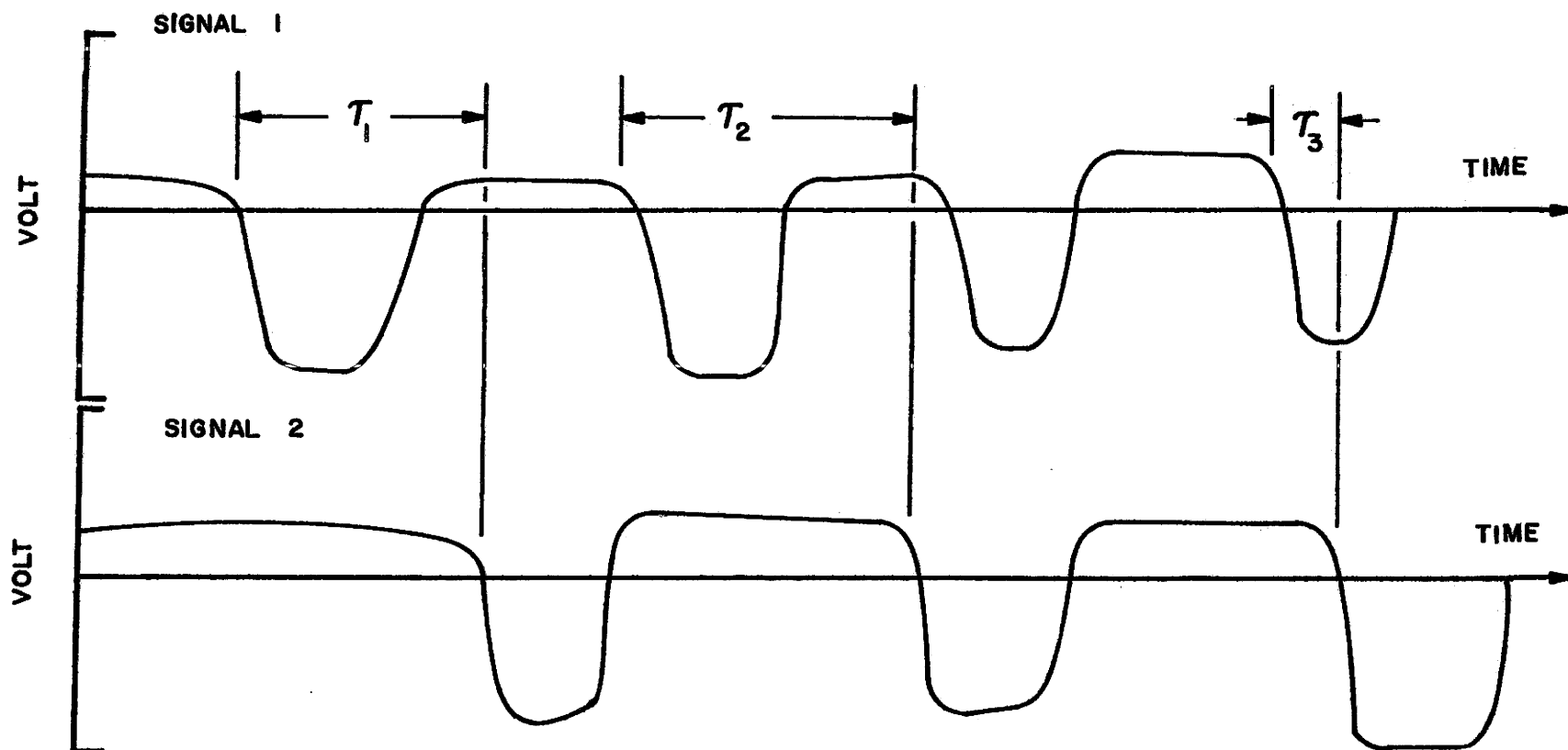


Figure (23). Output of the Conductance Probes
Situated at Two Neighbouring Active Sites

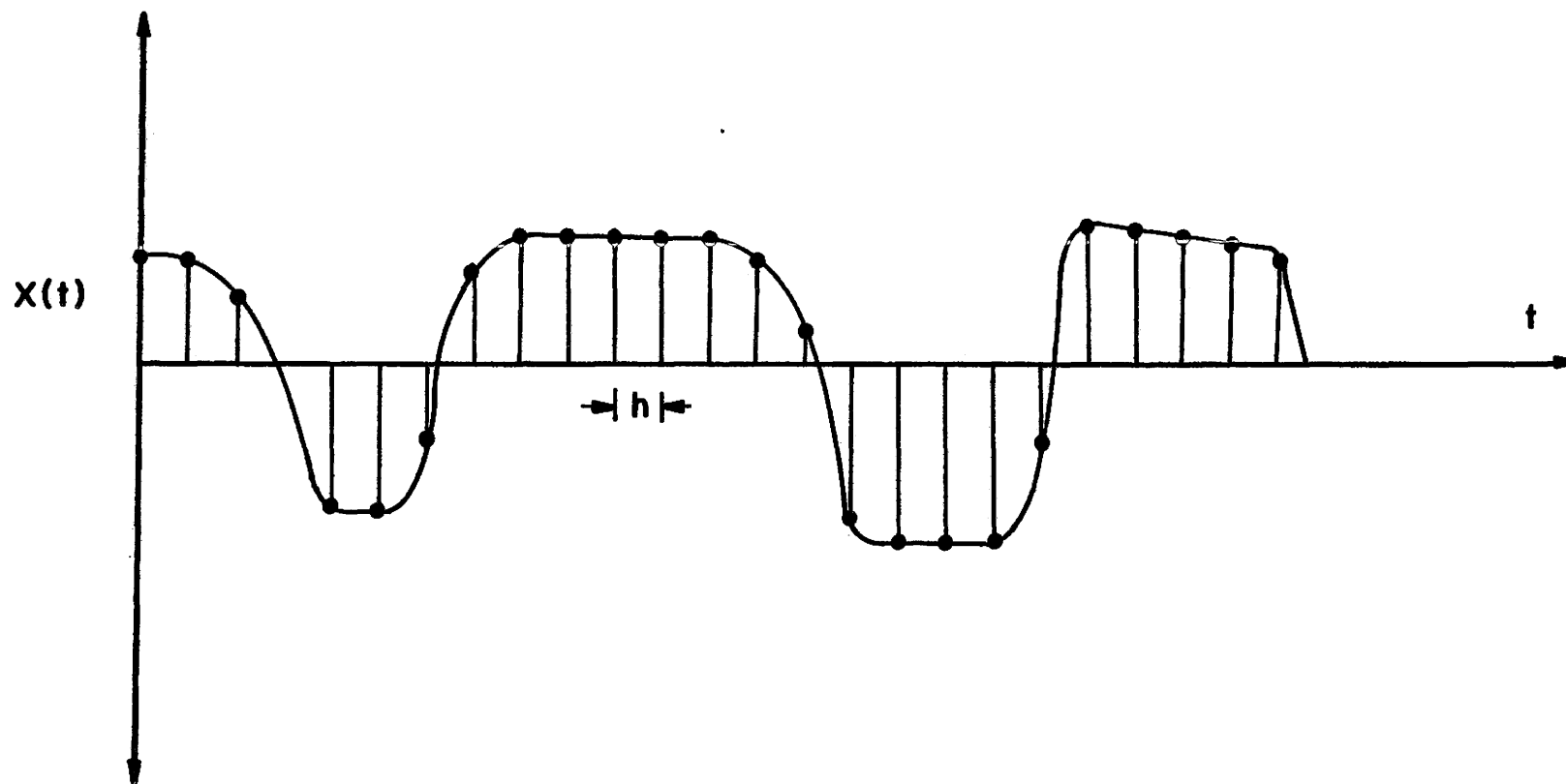


Figure (24). Sampling of Continuous Record

In the process of digitizing continuous signals the sampling interval h must be small enough so that "aliasing" will not be a problem. For example, suppose that we are observing some response signal that contains both high and low frequency components. If this response contains a 100 Hz sine wave and another signal of, say, 50 Hz, the sampling rate must be enough to pick up details from both signals. According to the sampling theorem, we must sample a sine wave twice per cycle to define it unambiguously. Thus we must sample the 50 Hz sine wave which has a period of 20 milliseconds, at least once every 10 milliseconds. This requires a sampling rate of 100 samples per second. The consequences of not sampling at a high enough rate are shown in the following figures. Figure (25.a) shows a sine wave sampled at just the cutoff frequency f_c . Figure (25.b) shows a frequency somewhat higher than the cutoff frequency, which may be represented as $f_c + \Delta f$. Figure (25.c) shows a third frequency $f_c - \Delta f$ which is just the same amount below f_c . Each of these three frequencies is sampled at just the cutoff frequency, f_c .

It is clear from either tracing or inspection that the data which the computer digitizes at the frequency $f_c + \Delta f$ and $f_c - \Delta f$ are identical. In fact, the points have exactly the same amplitude in the two cases, leading to the misidentification of a frequency $f_c + \Delta f$ as being $f_c - \Delta f$. This phenomenon is known as "fold-back", or "aliasing", and can be avoided only by choosing a sampling rate which is at least twice the cutoff

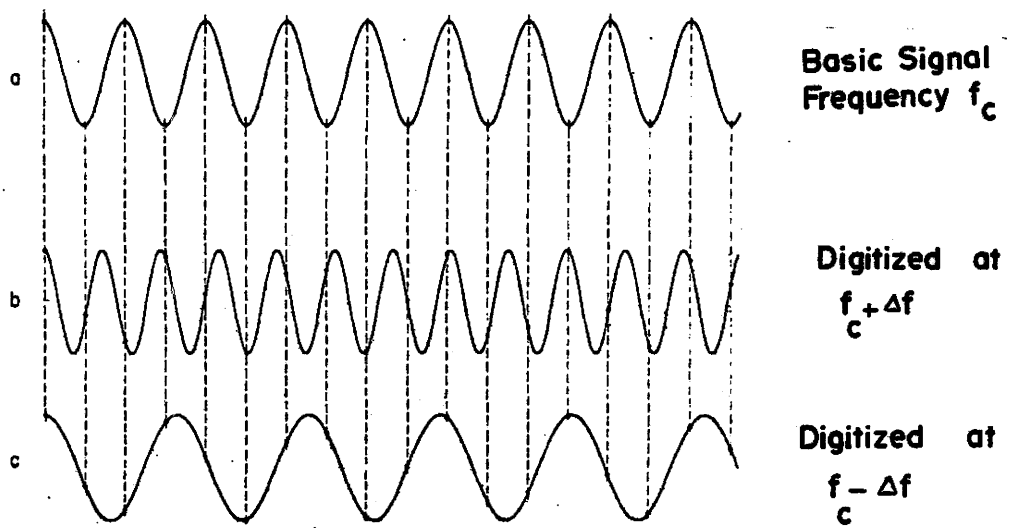


Figure (25). Sampling Near the Cutoff Frequency

frequency. In the present study, neither signal contained frequencies greater than 250 Hz and the cutoff frequency was taken as 500 Hz for the sake of accuracy in the subsequent analysis. The resulting sampling rate as 1000 samples per second and the sampling interval was equal to 1 millisecond.

For each set of data, the mean value \bar{u} as represented by equation (4.2) was calculated

$$\bar{u} = \frac{1}{N} \sum_{n=1}^N u_n \quad (4.2)$$

where

N is the number of data samples

u_n are the data values

1st signal $u_n = x_n$ ($n = 1, 2, \dots, N$)

2nd signal $u_n = y_n$ ($n = 1, 2, \dots, N$)

and subtracted from each data point. Accordingly the two sets of data were stored in the digital computer memory in a difference form for subsequent analysis. The advantage of using this difference technique is that the cross-correlation function coefficient goes to zero very quickly after a significant peak has occurred, and then oscillates about zero with a well defined period.

4.2 Measurement of the Time Elapse

Two methods of data processing have been used in the present study to obtain the time difference between the start of bubble growth at two neighbouring active sites involving

measurement of the time difference between the activity in two sets of signals caused by the formation of vapour bubbles. These methods are based on the cross-spectral density function and the cross-correlation function coefficient respectively. Two IMSL subroutines (FTFREQ and FTAUTO) have been used to calculate the mean, variance, autocovariance, autocorrelation and power spectrum of the individual series, as well as the cross-covariance, cross-spectrum, amplitude and phase of the cross-spectrum and coherence square of the two time series. The distinct peak locations in both cross-spectral density function and cross-correlation function coefficient have been noted. The experiment was repeated for the same test conditions and each time a new set of 1000 samples for each series was stored in the computer memory for similar analysis. Consecutive cumulative averages have been taken for the power spectrum, amplitude and phase of the cross-spectrum, cross-correlation function coefficient and coherence function until invariant distinct peaks were observed. The number of 1 millisecond correlation lag or lead values was specified equal to 100 in order to cover the bubble cycle time (growth and waiting time).

The two methods for determining the elapsed time τ are outlined in detail below.

4.2.1 Determination of Time Elapse by Cross-Spectral Density Function Analysis

The cross spectral analysis of two simultaneously

recorded time series provides information on the relationships between them in the form of estimates of amplitude and phase shift as functions of frequency. The cross-spectrum is simply defined as the Fourier transform of the cross-covariance for the two sets of time series $x(t)$ and $y(t)$. The cross-covariance for nonzero mean values can be defined by

$$C_{xy}(t, t+\tau) = E\{[x_n(t) - \mu_x(t)][y_n(t+\tau) - \mu_y(t+\tau)]\} \quad (4.3)$$

and in the case of zero mean values the cross-covariance becomes

$$R_{xy}(\tau) = E[x_n(t) y_n(t+\tau)] \quad (4.4)$$

The cross-spectral density function for a continuous signal is defined as

$$S_{xy}(f) = \int_{-\infty}^{\infty} R_{xy}(\tau) e^{-j2\pi f\tau} d\tau, \quad f \geq 0 \quad (4.5)$$

The cross-spectral density function for discrete data processes is defined as

$$S_{xy}(f) = h \sum_{\tau=-\infty}^{\infty} R_{xy}(\tau) e^{-j2\pi f\tau}, \quad -\frac{1}{2h} \leq f < \frac{1}{2h} \quad (4.6)$$

This cross-spectrum is a complex quantity such that:

$$S_{xy}(f) = L_{xy}(f) - j Q_{xy}(f) \quad (4.7)$$

where the real part, $L_{xy}(f)$, is called the co-spectral density

function and the imaginary part, $Q_{xy}(f)$, is called the quadrature spectral density function. Therefore it is more convenient to express the cross-spectral density function in complex polar notation such that:

$$S_{xy}(f) = |S_{xy}(f)| e^{-j\theta_{xy}(f)} \quad (4.8)$$

where:

$|S_{xy}(f)|$ is the cross-spectral amplitude and $\theta_{xy}(f)$ is the cross-spectral phase shift.

The cross-spectral amplitude $|S_{xy}(f)|$ shows whether the frequency components in one series are associated with large or small amplitudes at the same frequency in the other series. Similarly, the cross-spectral phase shift $\theta_{xy}(f)$ shows whether the frequency components at any frequency in one series lags or leads the components at the same frequency in the other series. Accordingly

$$|S_{xy}(f)| = \sqrt{L_{xy}^2(f) + Q_{xy}^2(f)} \quad (4.9)$$

$$\theta_{xy}(f) = \arctan \left[-\frac{Q_{xy}(f)}{L_{xy}(f)} \right] \quad (4.10)$$

The measurement of time difference between the start of bubble growth at two neighbouring active sites is one of the possible applications for a cross-spectral density function analysis. The time difference between the activity in the two time series $x(t)$ and $y(t)$ at any frequency f will be given by

$$\tau = \theta_{xy}(f)/2\pi f \quad (4.11)$$

In the computer analysis of the present investigation, the phase shift is represented in fractions of a circle between 0 and 1 and the amplitude is represented in fractions of the ratio of the amplitude at any frequency f to the largest amplitude in the cross-spectral density function.

The values of the spectral density function for each signal $x(t)$ and $y(t)$ and the cross-spectral density function have an undesirable property that their variances are dominated by a constant term which does not tend to zero as the record length increases. Hence the auto-power spectrum and the cross-power spectrum must be smoothed using a spectral (lag) window. The Hanning lag window method was used to eliminate discontinuities at the ends of the signal record. Multiplying the signal by the function $|\frac{1}{2} - \frac{1}{2} \cos(\frac{2\pi n}{N-1})|$, where $0 \leq n \leq N-1$, a modified signal was obtained, which has zero values at both ends of the signal.

4.2.2 Determination of Time Elapse by Cross-Correlation Function Coefficient Analysis

The cross-correlation function $R_{xy}(\tau)$ for two sets of data describes the general dependence of the values of one set of data on the other. An estimate for the cross-correlation function of the values of a continuous signal $x(t)$ at time t and a continuous signal $y(t)$ at time $(t+\tau)$ may be obtained by taking the average product for the two zero mean values

over the observation time T as T approaches infinity.

$$R_{xy}(\tau) = \lim_{T \rightarrow \infty} \frac{1}{T} \int_0^T x(t) y(t+\tau) dt \quad (4.12)$$

Estimates for the cross-correlation function are computed from discrete values of the signals $x(t)$ and $y(t)$. For the case where the series $x_n(t)$ leads the series $y_n(t)$ by time increment τ , where $\tau = 0, 1, \dots, N-1$, the cross-correlation function is given by

$$R_{xy}(\tau) = \frac{1}{N} \sum_{n=0}^{N-\tau-1} x_n(t) y_n(t+\tau) \quad (4.13)$$

For the case where series $y_n(t)$ leads $x_n(t)$ by time increment τ , where $\tau = -1, -2, \dots, -N+1$, the cross-correlation function is given by

$$R_{xy}(\tau) = \frac{1}{N} \sum_{n=|\tau|}^{N-1} x_n(t) y_n(t+\tau) \quad (4.14)$$

The cross-correlation function coefficient can be defined as

$$\rho_{xy}(\tau) = \frac{R_{xy}(\tau)}{\sqrt{R_x(0) R_y(0)}} \quad (4.15)$$

where

$R_x(0)$ is the auto-correlation function for series $x(t)$ at a displacement $\tau = 0$ (variance of $x(t)$ series).

$R_y(0)$ is the auto-correlation function for series $y(t)$ at a displacement $\tau = 0$ (variance of $y(t)$ series),

and
$$-1 \leq \rho_{xy}(\tau) \leq 1$$

The function $\rho_{xy}(\tau)$ measures the degree of linear dependence between series $x(t)$ and series $y(t)$ for displacement of τ in the $y(t)$ series relative to the $x(t)$ series. The measurement of the time elapsed between the start of bubble growth for the two neighbouring active sites is one of the possible applications for a cross-correlation function coefficient analysis.

4.3 Confidence Limit on the Cross-Correlation Function Coefficient

A crude check was used to see whether the peak values of the cross-correlation function coefficient $\rho_{xy}(\tau)$ were significant which was done by comparing the corresponding cross-correlation estimates with their approximate standard errors obtained from a formula by Bartlett [78] as mentioned in reference [22] given by:

$$\text{Var} [\rho_{xy}(\tau)] = \frac{1}{N-\tau} \sum_{v=-\infty}^{\infty} \rho_{xx}(v) \rho_{yy}(v) \quad (4.16)$$

on the hypothesis that the two processes have no cross-correlation.

The confidence limit is calculated for the unknown

variance of $\rho_{xy}(\tau)$ to find a region within which we can be 95% confident that the true value of $\rho_{xy}(\tau)$ equal to zero lies.

The 95% C.I. on $\rho_{xy}(\tau) = 0$ can be calculated for 99 degrees of freedom by

$$\text{C.I.} = 0 \pm t_{2.5,99} \sqrt{\text{Var}[\rho_{xy}(\tau)]} \quad (4.17)$$

In the calculation of the time elapsed between the start of growth at two neighbouring active sites, all the values of $\rho_{xy}(\tau)$ within the confidence interval have been ignored and only those which exceed the confidence interval have been considered to be significant.

4.4 Signal Processing Flowchart

A flowchart of the data processing technique is presented in figure (26).

4.5 Representative Example

The experimental data for the elapsed time (τ) was obtained using cross-spectral density function analysis and cross-correlation function coefficient analysis as discussed previously. Figure (27.a,b) shows an example of the data which was obtained from $S = 4.2$ mm after several cumulative averages had been taken for the results. The autopower spectrum of the signal $x(t)$ indicates that the predominant frequency in this series is approximately 18 Hz and the autopower spectrum of the signal $y(t)$ indicates that the

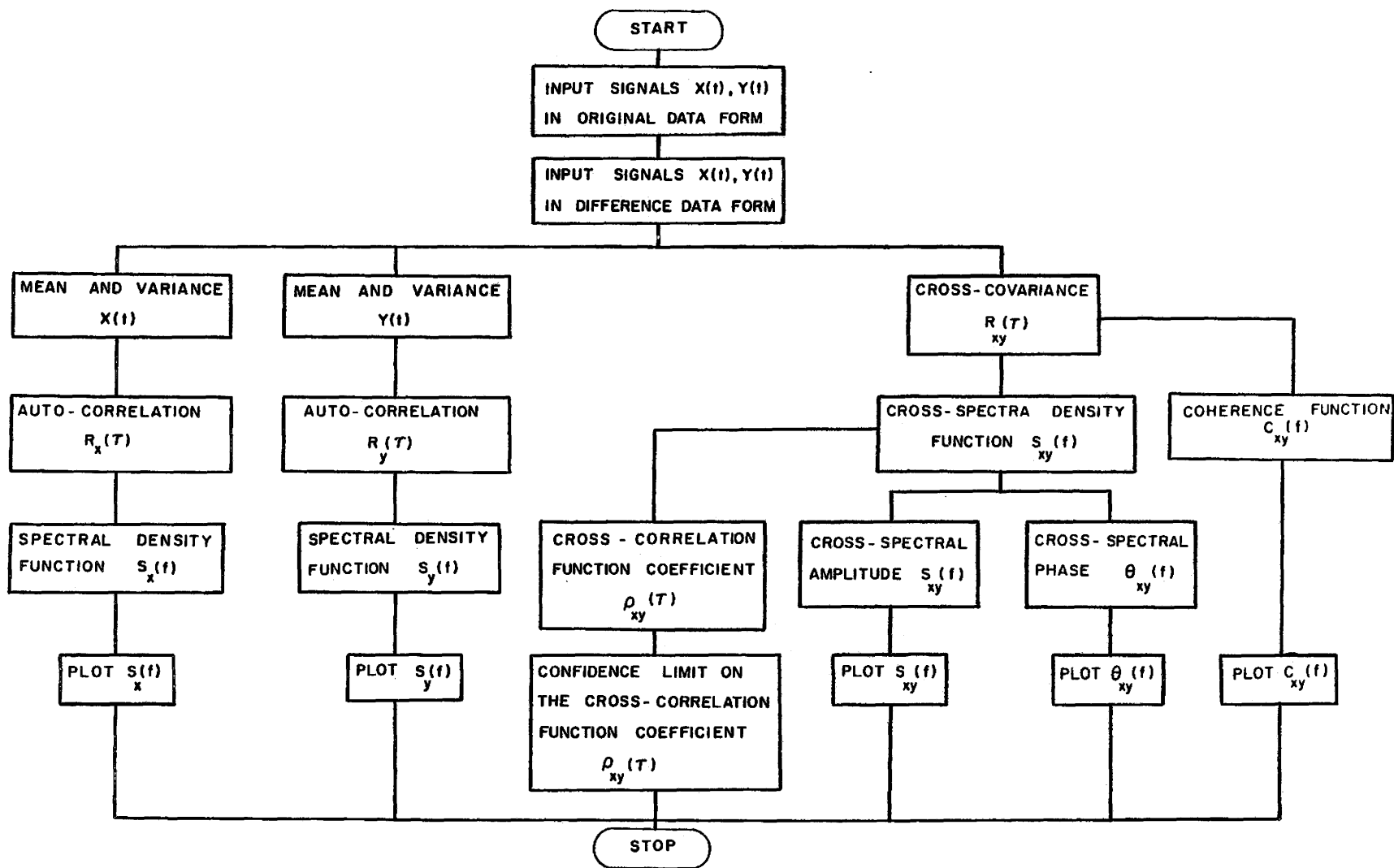


Figure (26). Signal Processing Flowchart

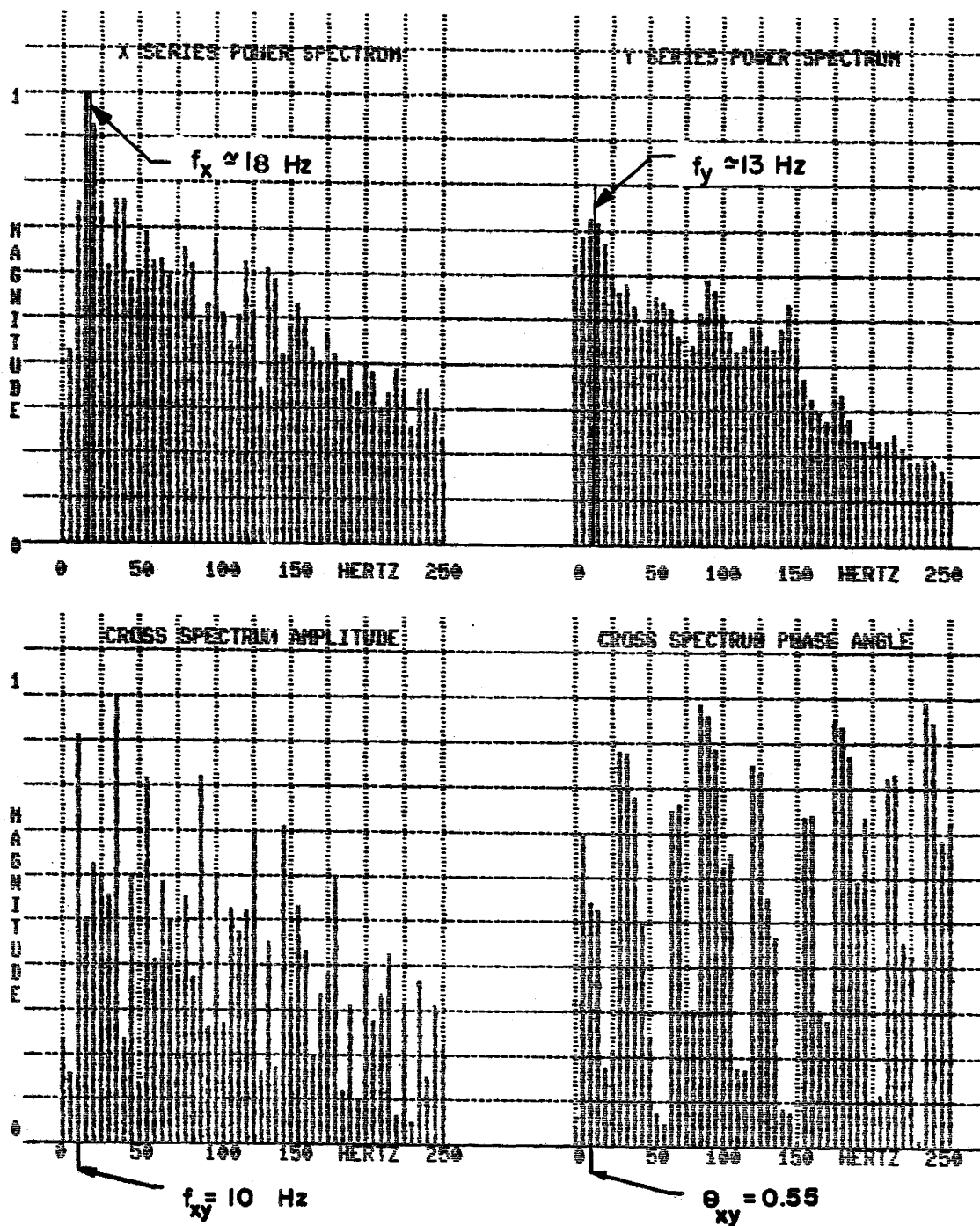


Figure (27.a). Example of the Data Obtained in the Present Study

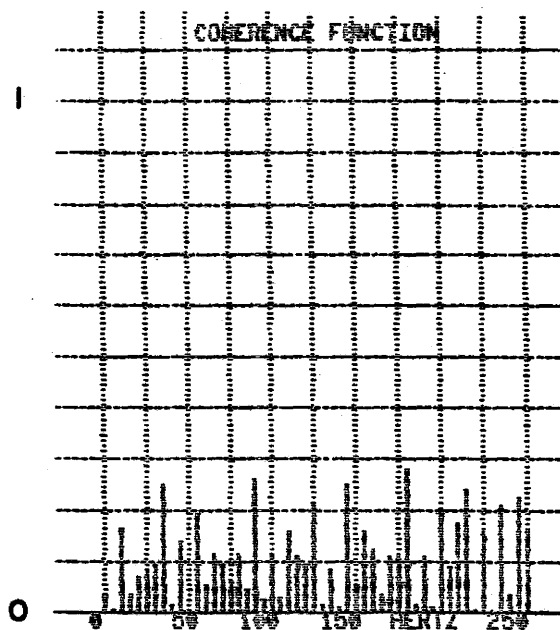
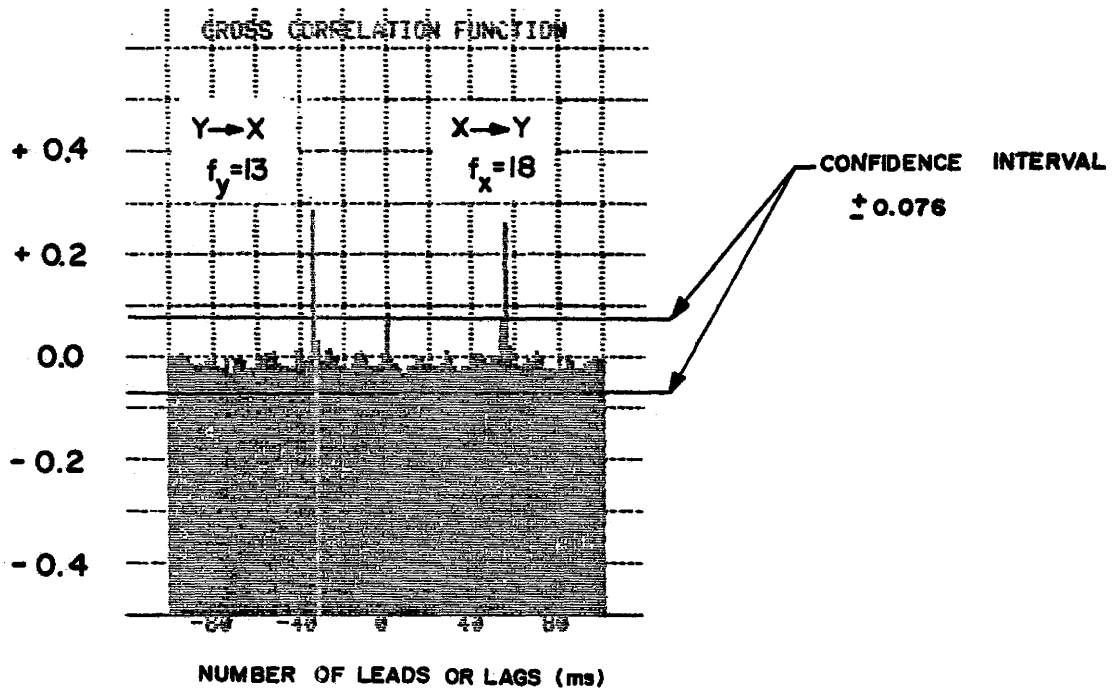


Figure (27.b). Example of the Data Obtained in the Present Study

predominant frequency in this series is approximately 13 Hz. Analysis of the cross-spectrum amplitude indicates that the first significant spike which is present in the correlation between the activity in $x(t)$ and $y(t)$ where $x(t)$ leads $y(t)$ occurs at $f_{xy} = 10$ Hz. Analysis of the cross-spectrum phase shift at $f_{xy} = 10$ Hz indicates that the phase shift θ_{xy} is approximately 0.55. Since the computed value of the phase shift was expressed in fractions of a circle between 0 and 1, therefore $\theta_{xy} = 0.55 * 2 \pi$ radians so that by substitution of the values of f_{xy} and θ_{xy} in equation (4.11), the time elapsed between the start of bubble growth at the two neighbouring active sites turned out to be 55 milliseconds.

The analysis of the cross-correlation function indicates a strong correlation between the activity in both signals $x(t)$ and $y(t)$ at 55 milliseconds, consistent with the value obtained by cross-spectral analysis in which case it may be concluded that site x causes the activation of site y .

Similarly a strong correlation can also be seen at -34 ms in which case site y causes the activation of site x as shown in figure (27.b). As far as the present investigation is concerned, in order to study the effect of one active site on its surrounding active sites, only the peaks corresponding to the case in which signal $x(t)$ leads the signal $y(t)$ were considered. The coherence function didn't play any significant role in the present investigation.

CHAPTER 5

RESULTS AND DISCUSSION

This chapter is devoted to the analysis of the experimental data obtained and comparison of the proposed theoretical models with the experimental findings.

In general, during stable nucleation and boiling of a liquid at an active site on a surface, a periodic stream of bubbles is emitted. The time elapsed between two subsequent bubble emissions is defined as the bubble time period. This time is comprised of two components, the waiting time τ_w which is the time from the last bubble departure to the beginning of the next bubble growth and the growth time τ_g which is the time from the beginning of bubble growth until its departure from the surface.

The present study concerns time τ which is the time elapsed between the start of bubble growth at two neighbouring active sites. Because this is an original investigation, three different theoretical models have been devised in an attempt to explain the experimental findings. The first model involves heat diffusion through the water, the second model is based upon the disturbance caused by the propagation of a pressure pulse in a mixture of water and vapour and the third model involves heat diffusion through the heating surface.

5.1 Experimental Results

The characteristic boiling curve for the heating

surface used in the present study is shown in figure (28). The boiling curve represents the relationship between the surface superheat ($T_w - T_s$) and the heat flux Q/A . The experimental part of this investigation was performed for boiling water at atmospheric pressure on a single copper surface for two different levels of heat flux (92.21 and 192.11 kW/m²) and two different levels of subcooling (0, 7.5°C). Since the present investigation was performed to study the interaction of the nucleation phenomena at the adjacent sites, the relationship between the time elapsed between the start of bubble growth at two neighbouring active sites τ and the separating distance S was examined.

Different sets of active sites were studied individually at each level of heat flux and subcooling, each set consisting of one active site and its surrounding active sites at various distances (S_1, S_2, \dots) as shown in figure (29). The time elapsed between the start of bubble growth at two neighbouring active sites was determined by cross-spectral density function analysis and cross-correlation function coefficient analysis as discussed previously in Chapter 4. The high heat flux level (192.11 kW/m²) was tested first at saturation conditions; due to the vertical and horizontal bubble interactions as reported by Moissis and Berenson [23] and Kirby and Westwater [24] it was not possible to detect any cross-correlation between the two probe signals $x(t)$ and $y(t)$. The vertical and horizontal interactions can be reduced by increasing subcooling at the same heat flux

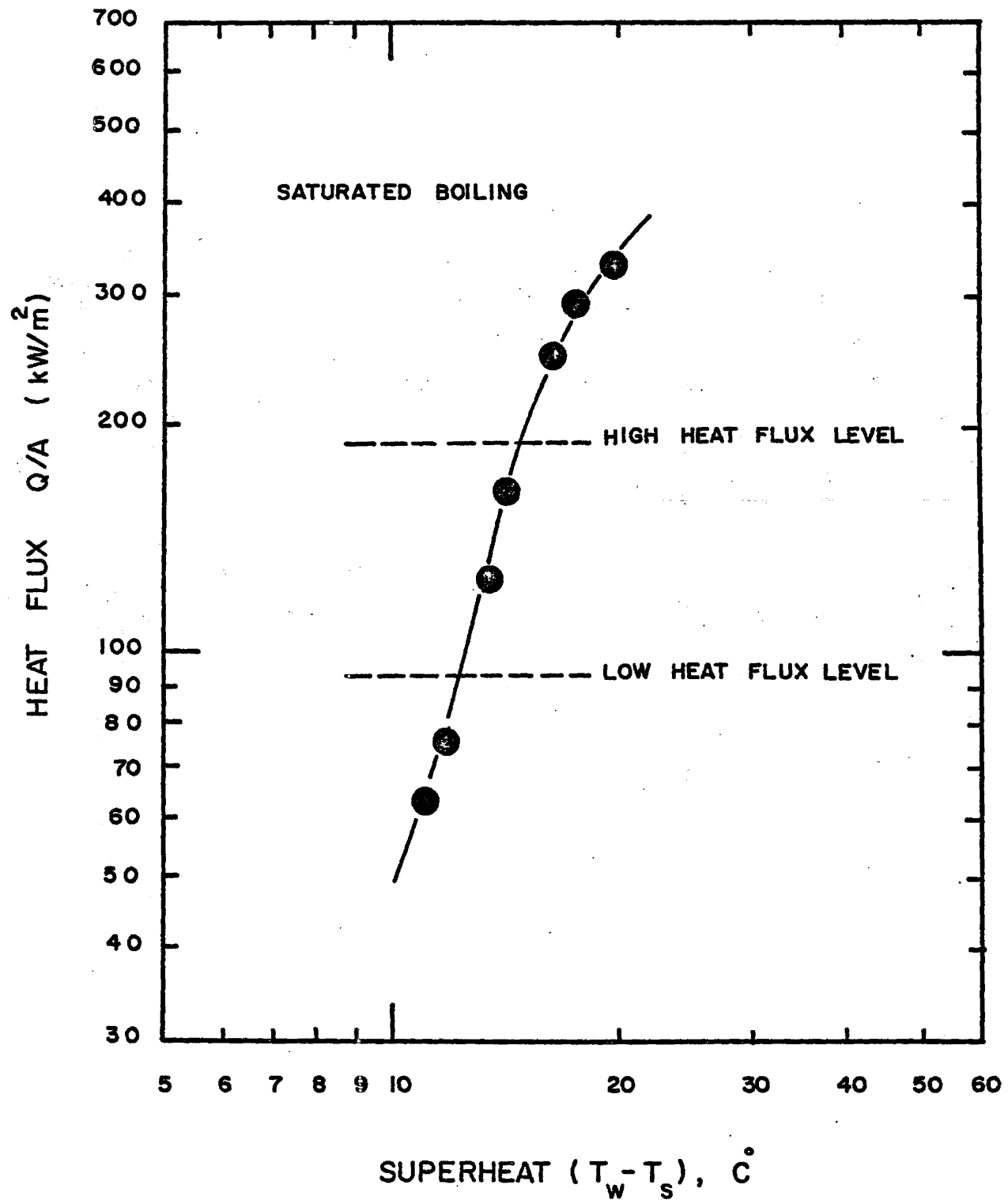


Figure (28). Characteristic Boiling Curve for Present Investigation

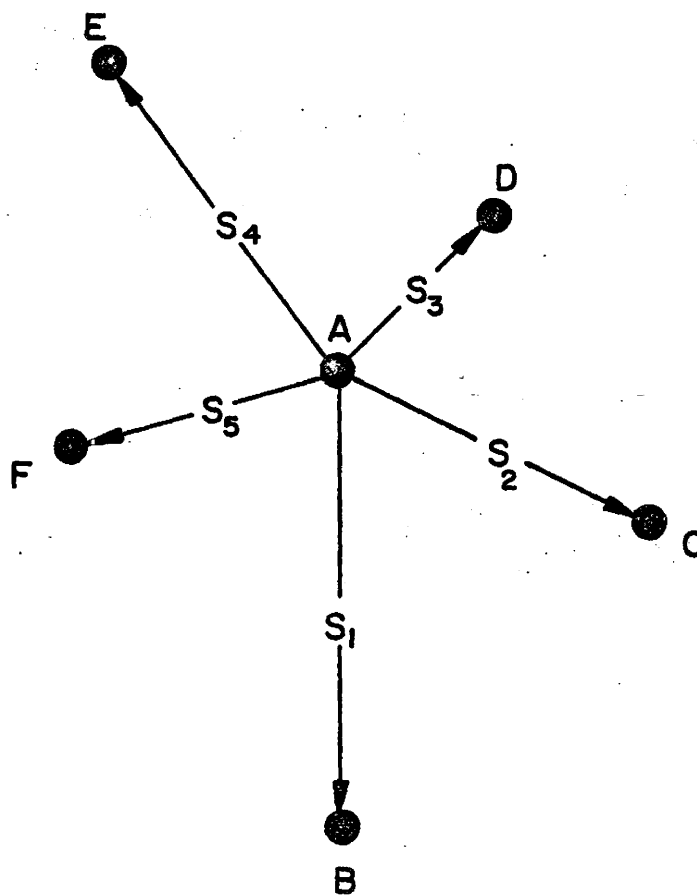


Figure (29). Arrangement of Active Nucleation Site (A) and Its Surrounding Active Nucleation Sites (B, C, D, E, F)

level. For the (7.5°C) subcooling condition at the same level of heat flux (192.11 kW/m^2) it was possible to detect a cross-correlation between the two probe signals. The regression analysis for the results obtained as shown in figures (30, 31, 32, 33) indicates that a weak correlation existed between the elapsed time (τ) and the separating distance (S). Different sets were examined as a preliminary study for the lower level of heat flux (92.21 kW/m^2) and subcooling ($0, 7.5^{\circ}\text{C}$) for which it was possible to detect a stronger cross-correlation between the two probe signals. The regression analysis for the results obtained as shown in figures (34) and (35) indicates a significant correlation between the separating distance (S) and the time elapsed (τ), such that the time elapsed between the start of bubble growth at the two neighbouring active sites increases with increasing separating distance between two active sites. In light of this significant correlation, a single set consisting of an active site and its surrounding active sites was studied in detail at the lower level of heat flux (92.21 kW/m^2) and three different levels of subcooling ($0, 6.5, 12^{\circ}\text{C}$). The combined experimental results are presented in figure (36). The graph shows the existence of a unique relationship between the separating distance S and the time elapse τ between the start of bubble growth at two neighbouring active sites. The dependence of τ on S disappears for the three different levels of subcooling after approximately 4.5 mm which is about twice the bubble departure diameter in the

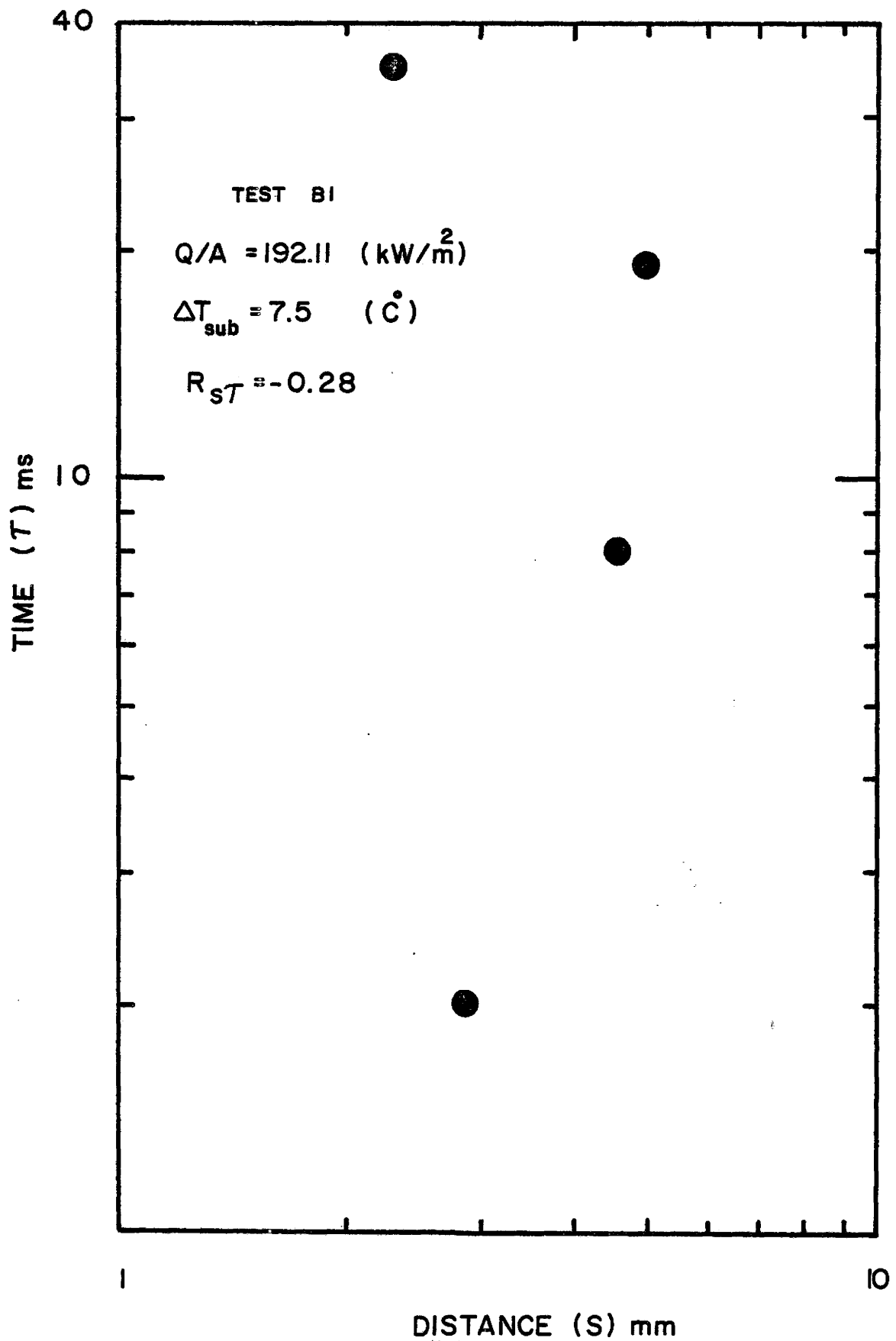


Figure (30). Relationship Between Elapsed Time (τ) and Separating Distance (S)

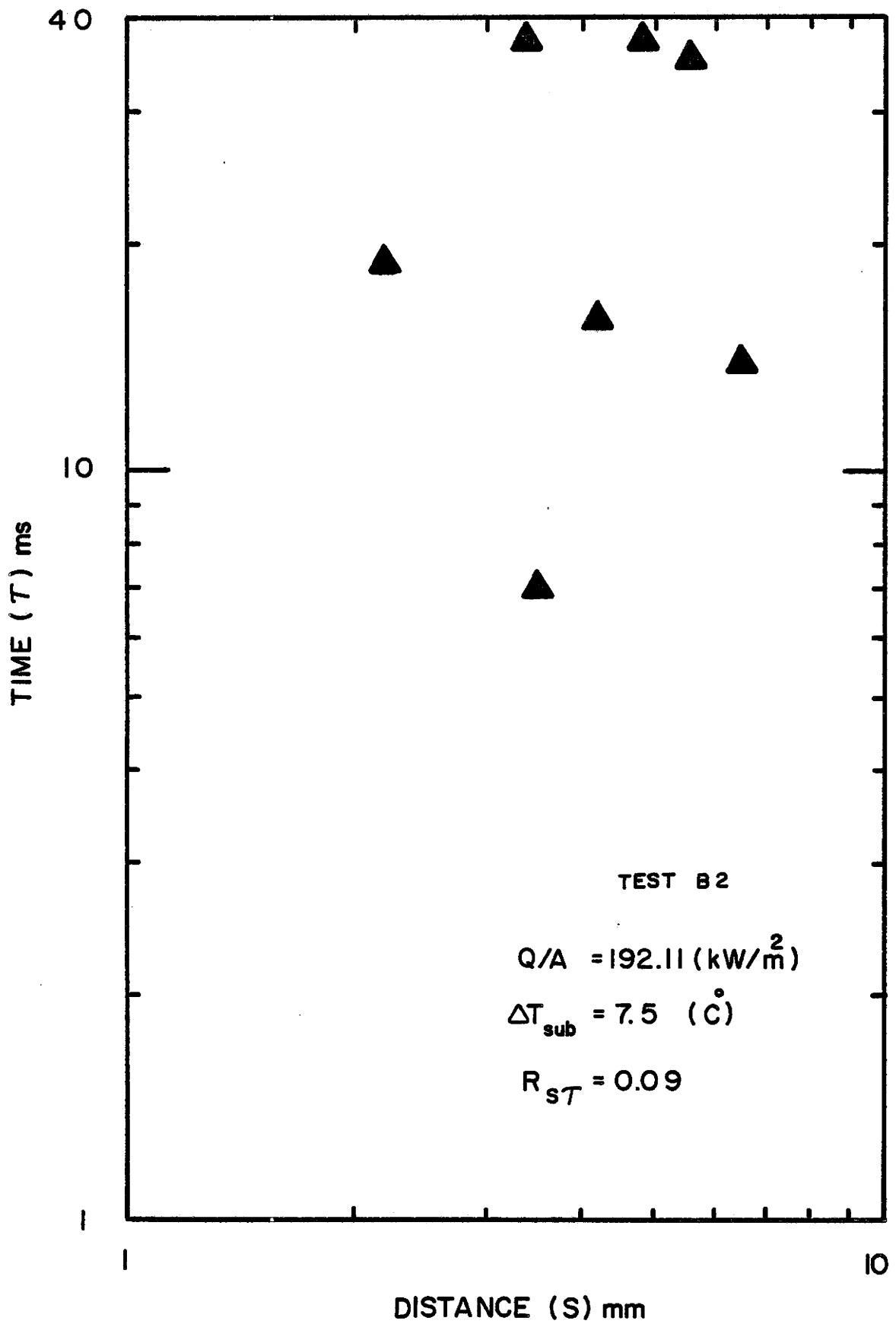


Figure (31). Relationship Between Elapsed Time (τ) and Separating Distance (S)

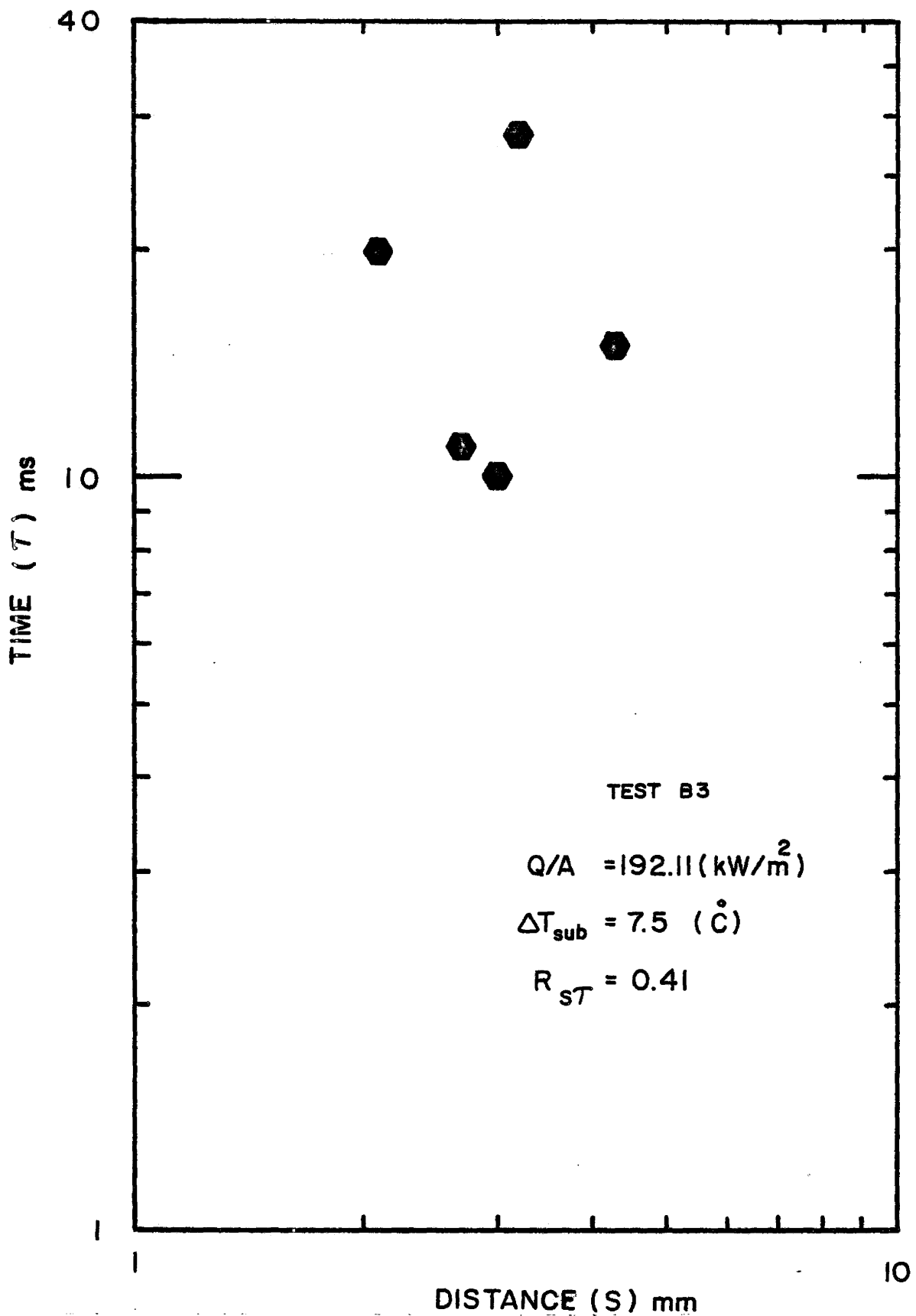


Figure (32). Relationship Between Elapsed Time (τ) and Separating Distance (S)

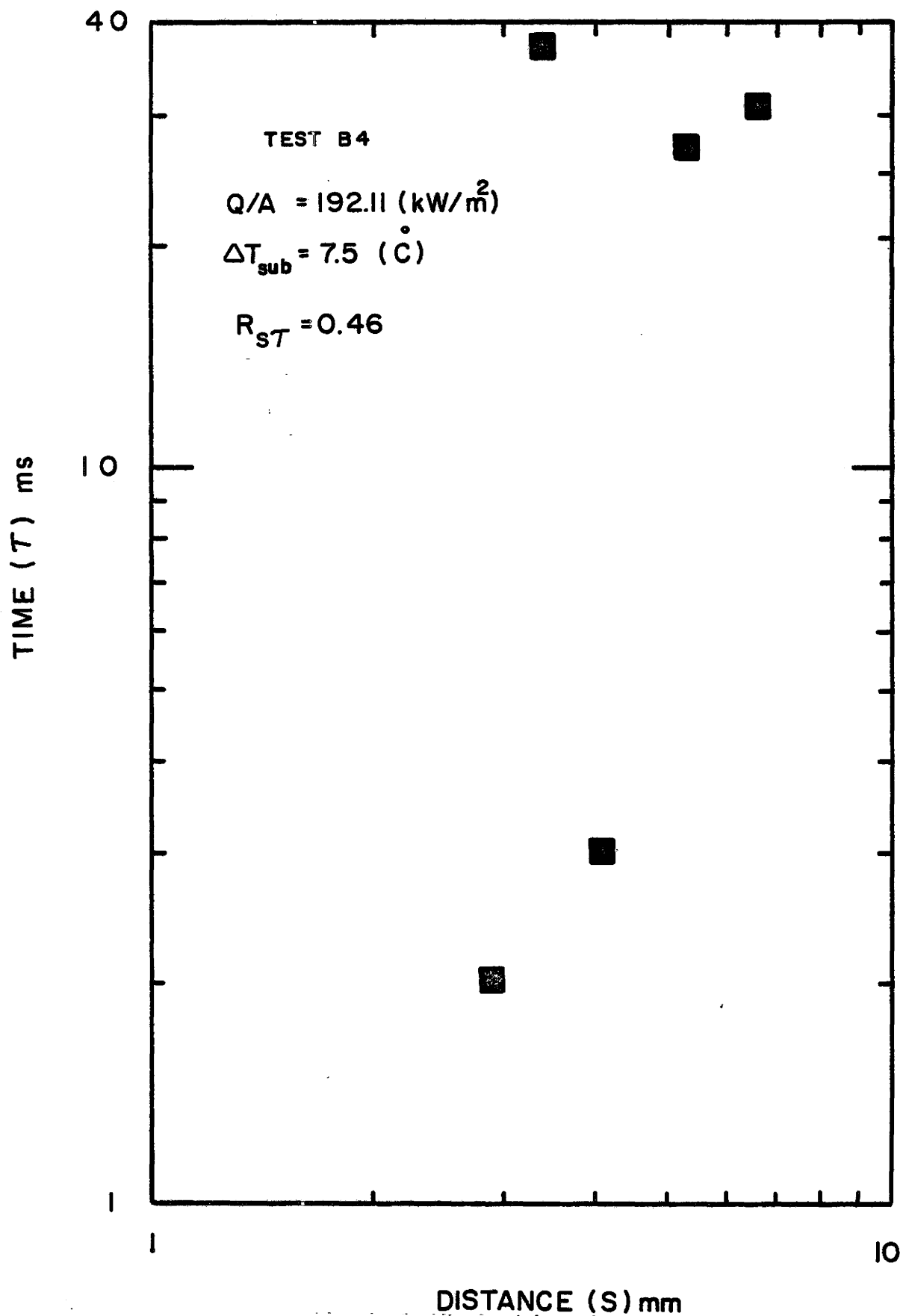


Figure (33) Relationship Between Elapsed Time (τ) and Separating Distance (S)

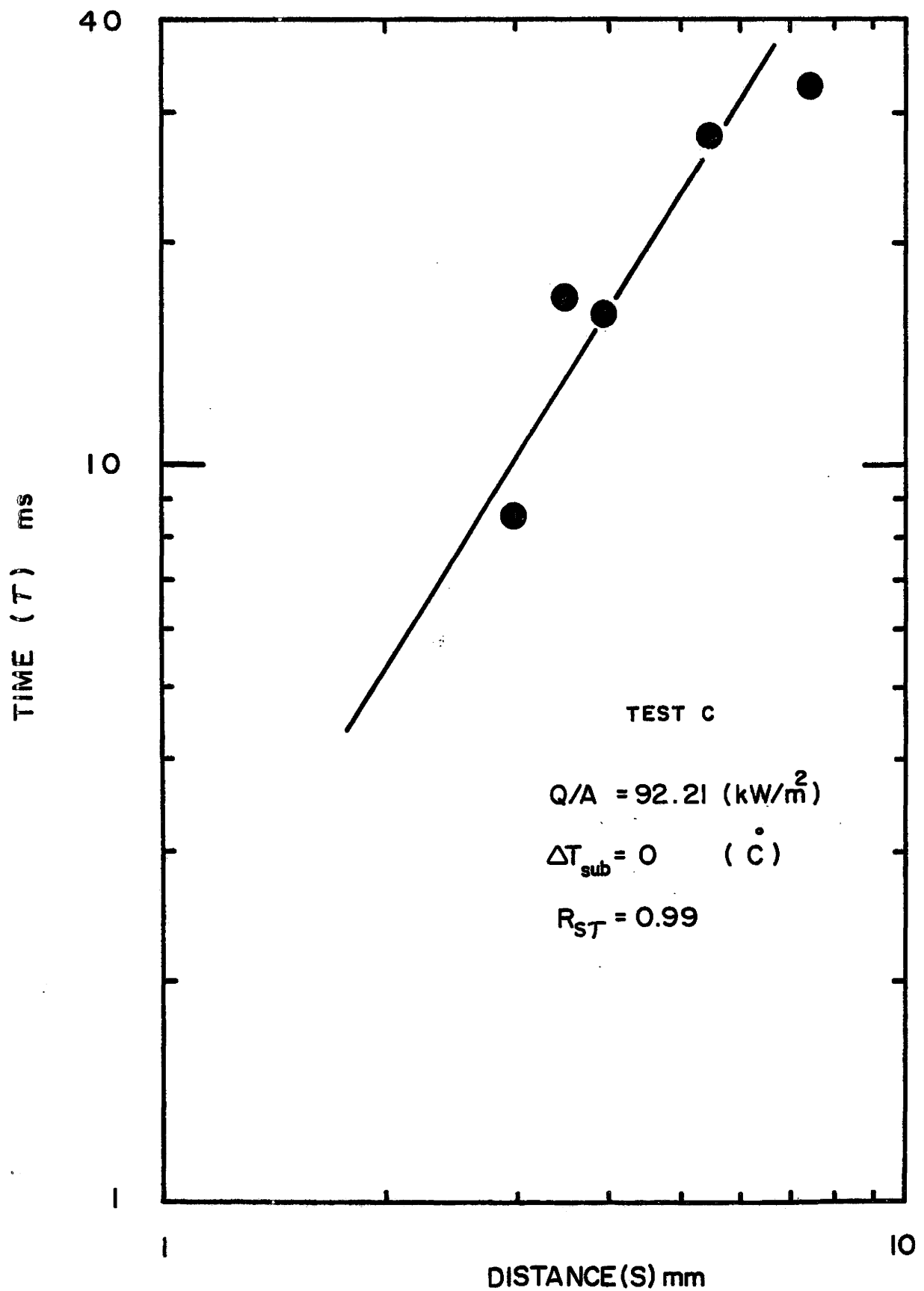


Figure (34). Relationship Between Elapsed Time (τ) and Separating Distance (S)

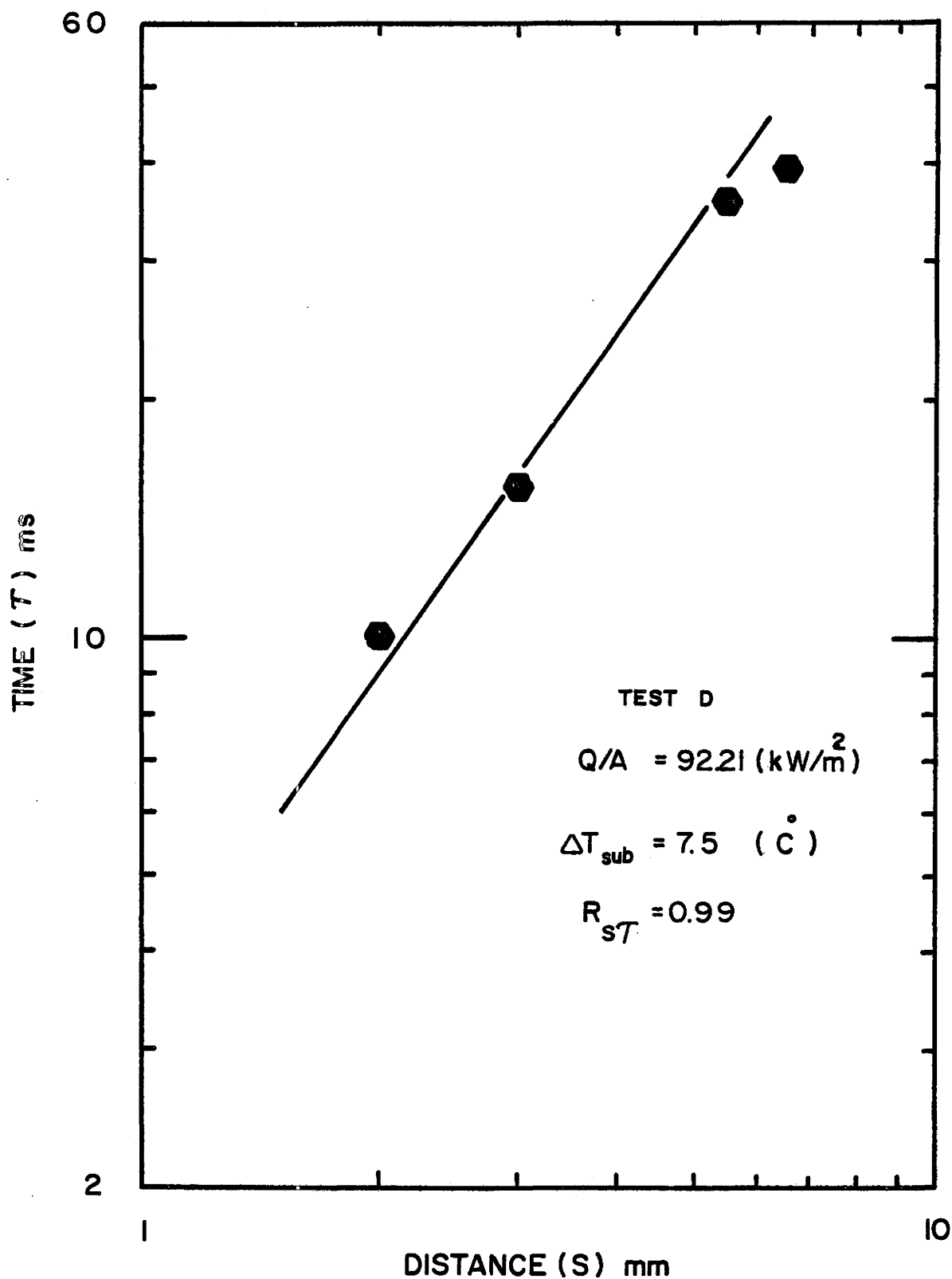


Figure (35). Relationship Between Elapsed Time (τ) and Separating Distance (S)

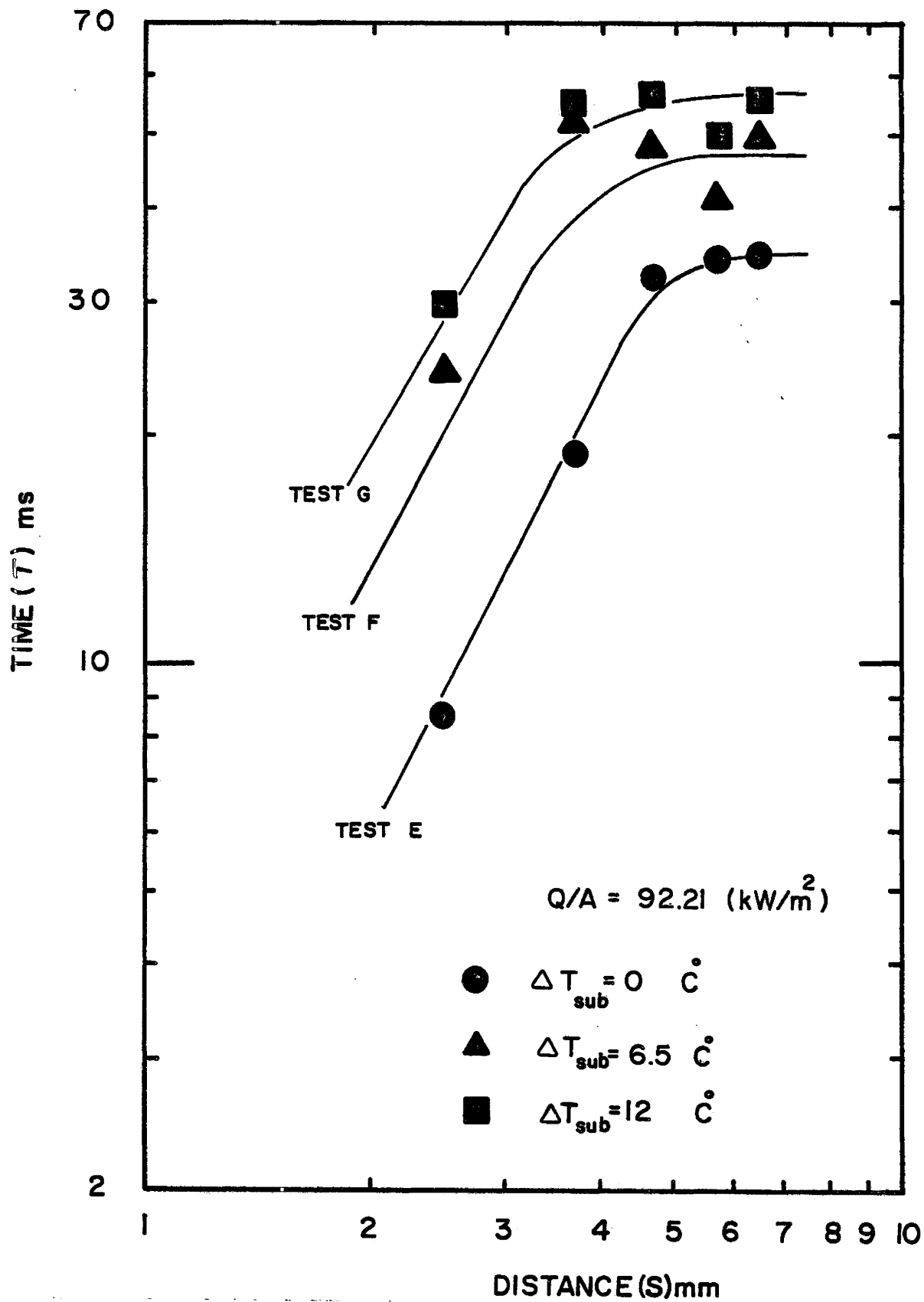


Figure (36). Relationship Between Elapsed Time (τ) and Separating Distance (S) for Three Different Levels of Subcooling

saturation condition. The values of bubble growth time and bubble departure size for the lower level of heat flux (92.21 kW/m^2) and three different levels of subcooling ($0, 6.5, 12^\circ\text{C}$) are represented in table (3). The computation of the tabulated values is presented in Appendix (H).

Although the experimental results indicate that the time elapsed between the start of bubble growth at two neighbouring active sites for the three levels of subcooling is greater than the corresponding bubble growth time, the interaction phenomena between the nucleation site and its surrounding active sites may occur after bubble detachment from the heating surface. Accordingly, the experimental results were rearranged in terms of the separating distance - bubble departure size difference ($S-R_d$) and the time elapsed between the start of the bubble growth for the two active sites minus the bubble growth period ($\tau-\tau_g$).

Plotting the data in terms of ($S-R_d$) versus ($\tau-\tau_g$) as shown in figure (37) tends to draw the experimental results together into a single curve suggesting that a single relationship might fit all the experimental data as discussed later in this chapter.

5.2 Theoretical Analysis and Discussion

As mentioned before, three different theoretical models have been devised in an attempt to explain the experimental findings; these models will be discussed in detail below.

TABLE (3)
ESTIMATED VALUES OF DEPARTURE
RADIUS AND BUBBLE GROWTH TIME

SYMBOL	BUBBLE PERIOD	ΔT_{sub}	ESTIMATED R_d	ESTIMATED τ_g
	(ms)	($^{\circ}\text{C}$)	(mm)	(ms)
●	50	0	1.17	5.9
▲	59	6.5	0.75	3.2
■	67	12	0.55	1.7

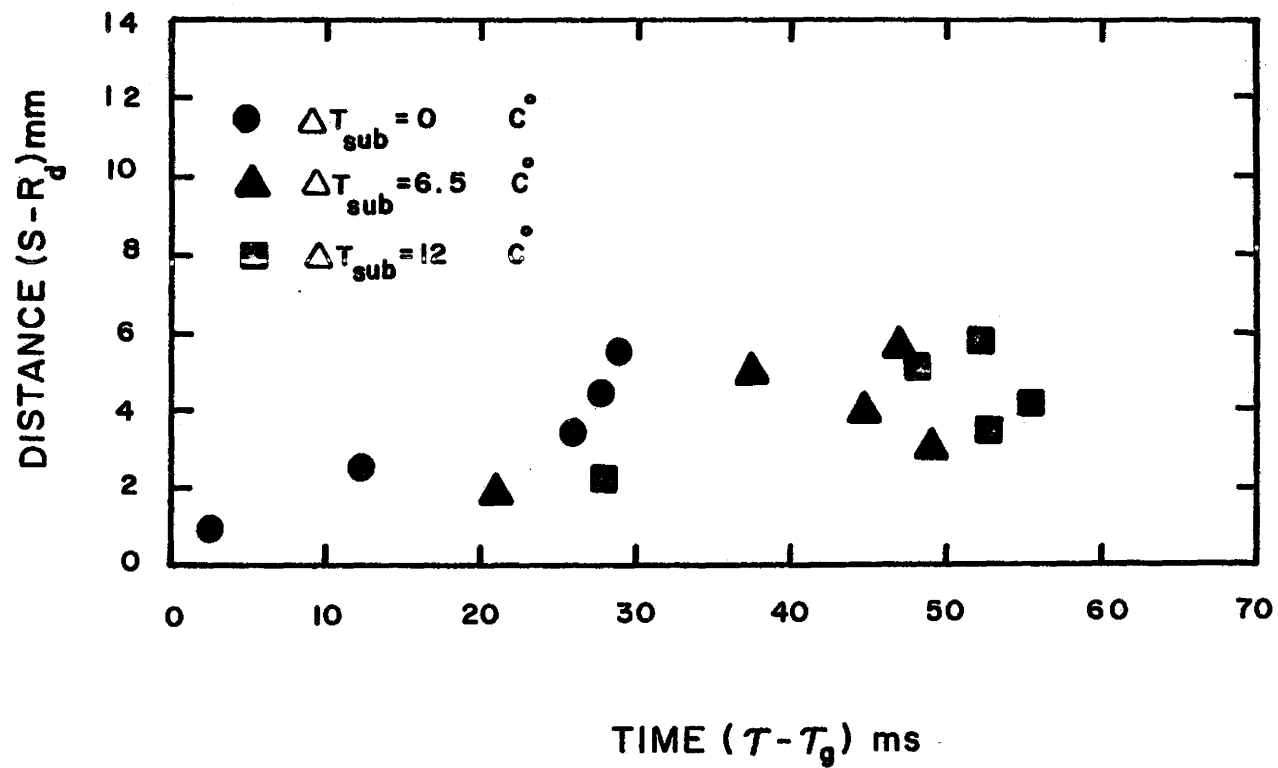
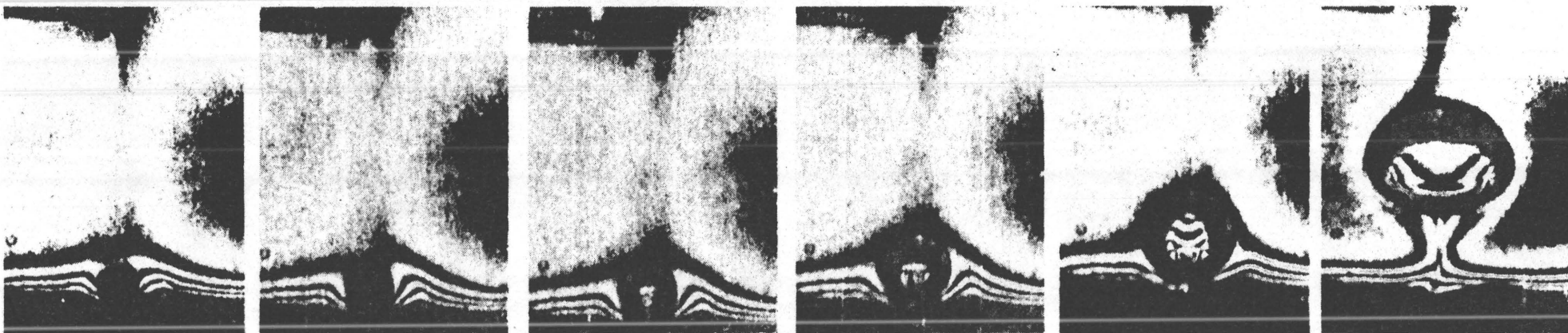


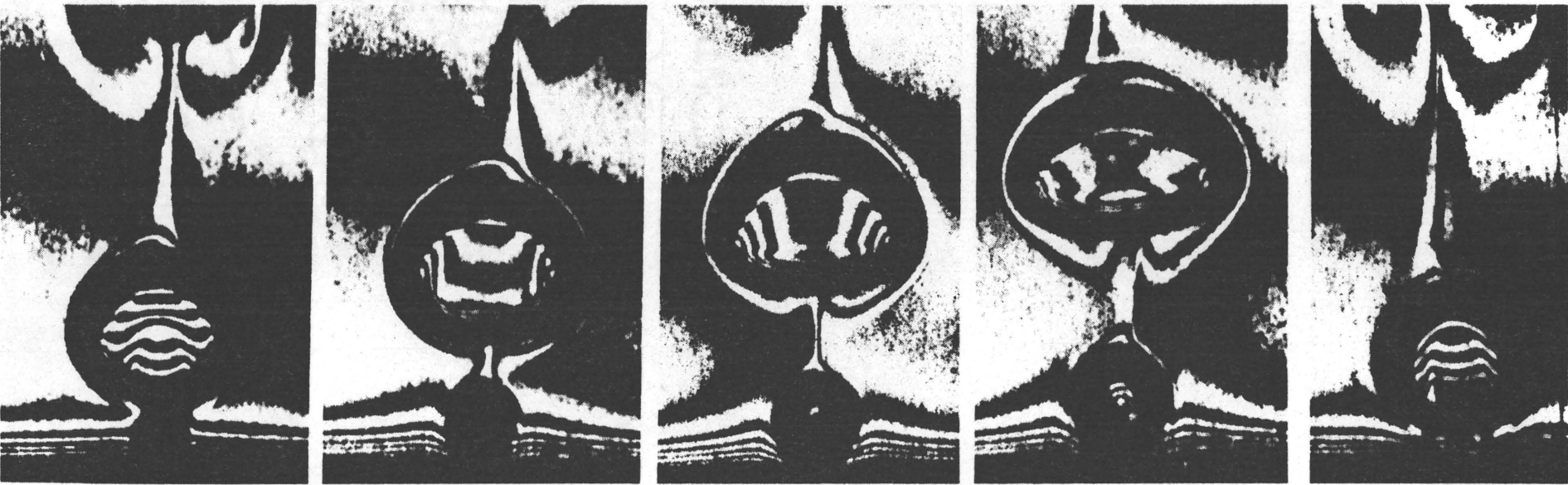
Figure (37). Distance (S- R_d) Versus Time Elapsed ($\tau - \tau_g$)

5.2.1 Heat Diffusion Through the Water

The approach used in the derivation of this model was based upon the propagation of a temperature disturbance in the water. As far as the temperature field in the region around a growing vapour bubble is concerned, very little literature is available. However the temperature field around a growing vapour bubble was discussed by Beer et al. [25] for Freon 113 (R13) boiling under atmospheric pressure conditions. High speed motion pictures (1800 and 600 frames per second) were obtained with a HeNe-Laser. The interferograms show an undisturbed temperature field above the heat surface at a considerable distance from the bubble interface. The isothermal fringe pattern formation close to the growing bubble which they observed can be seen in the photographs presented in figures (38.a) and (38.b). As the bubble starts to grow, the superheated liquid layer at the surface is pushed away from the nucleation site and high temperature liquid accumulates at the periphery of the growing bubble on the heating surface as shown schematically in figure (39). On the basis of this observation, the phenomenon in the present model has been approximated by the transfer of heat to the surrounding liquid from an instantaneous ring source with strength Q at a radius r' in the plane $Z = 0$ as shown in figure (40). The temperature disturbance which results propagates outward through the liquid in the radial direction. Throughout this derivation the following assumptions were considered:



(a) Interference fringe pattern for a growing Freon 113-steam bubble (bubble sequence, 1800 f/s) obtained with a laser Mach-Zehnder interferometer ($p_s = 1$ bar, $t_s = 46.1^\circ\text{C}$, $t_L = 45.3^\circ\text{C}$, fringe spacing corresponds to 1.32°C).



(b) Interference fringe pattern for a growing Freon 113-steam bubble (bubble sequence, 600 f/s) obtained with a laser Mach-Zehnder interferometer ($p_s = 1$ bar, $t_s = 46.3^\circ\text{C}$, $t_L = 44.2^\circ\text{C}$, fringe spacing corresponds to 1.5°C).

Figure (38) Interference Fringe Pattern for Growing Freon 113 Bubble

NUCLEUS STANDING AT THE
CAVITY MOUTH



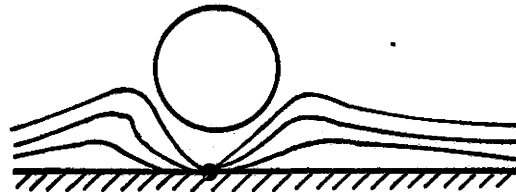
TEMPERATURE DISTRIBUTION
AROUND THE BUBBLE DURING
THE EARLY STAGES OF THE
BUBBLE GROWTH



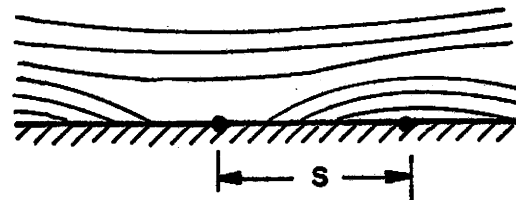
TEMPERATURE DISTRIBUTION
AROUND THE BUBBLE AT THE
END OF THE BUBBLE GROWTH



HIGH TEMPERATURE LIQUID
DISTRIBUTION AFTER BUBBLE
DETACHMENT FROM THE
HEATING SURFACE



PROPAGATION OF THE HIGH
TEMPERATURE DISTURBANCE
OUTWARD IN THE RADIAL
DIRECTION



ACTIVATION OF THE NEIGHBOURING
NUCLEATION SITE AT DISTANCE s

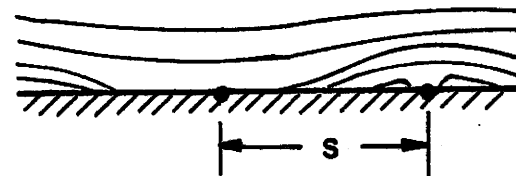


Figure (39). Distribution of High Temperature Liquid in the Vicinity of a Growing Bubble

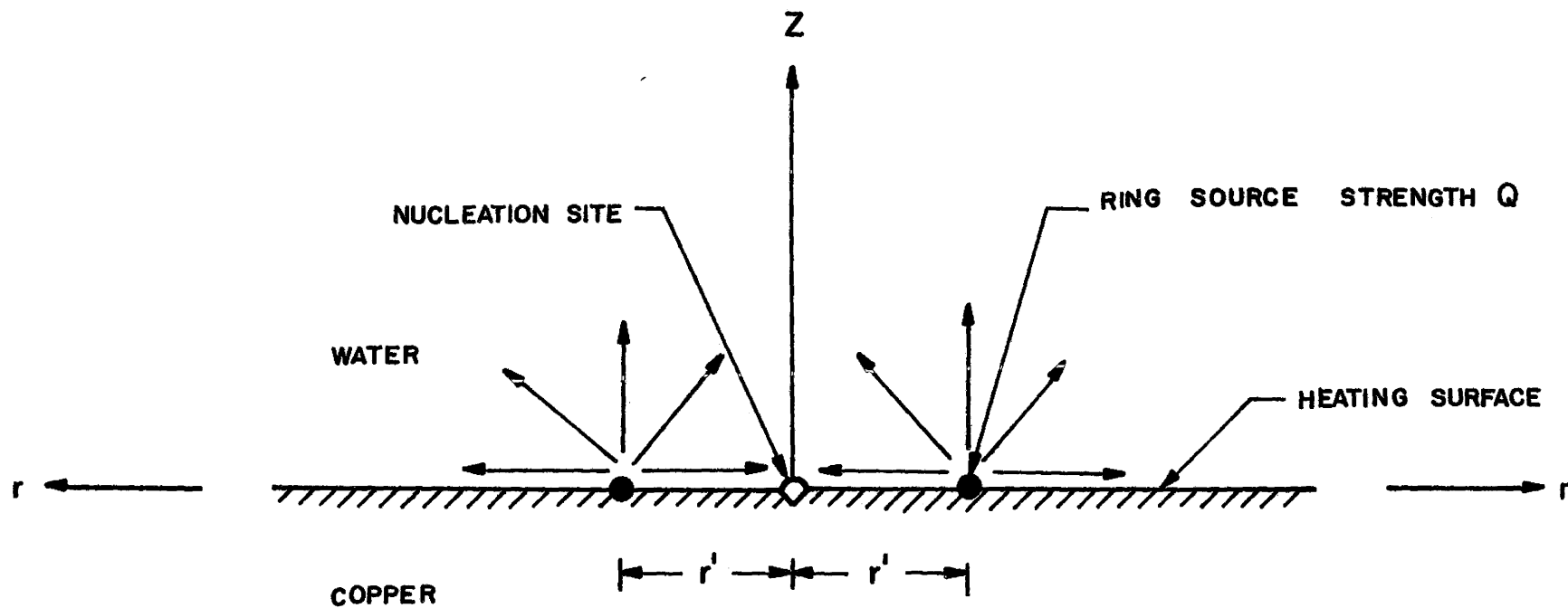


Figure (40). Idealized Model for Heat Diffusion from an Instantaneous Ring Source of Strength Q in the Surrounding Water

1. Nuclei capable of being activated exist at surrounding nucleation sites at distances S_1, S_2, \dots
2. Only the pair of sites being investigated interact with each other.
3. Heat diffusing from an instantaneous ring source through the surrounding liquid propagates in the radial direction close to the heating surface.
4. For the purpose of analysis, no heat is transferred from the ring source to the heating surface.

The temperature variation of interest occurs in the vicinity of the heating surface, so that the differential equation of heat conduction in cylindrical coordinates was considered most appropriate to describe the process. Therefore, the governing equation becomes

$$\rho_l C_l \frac{\partial T_l}{\partial t} = k_l \left[\frac{1}{r} \frac{\partial}{\partial r} \left(r \frac{\partial T_l}{\partial r} \right) \right] \quad (5.1)$$

The initial conditions are:

$$T_l(r, 0) = T_0 \quad r=r' \quad (5.2)$$

$$T_l(r, 0) = 0 \quad r \neq r' \quad (5.3)$$

The boundary conditions are:

$$\frac{\partial T_l(0, t)}{\partial r} = 0 \quad (5.4)$$

$$T_l(\infty, t) = 0 \quad (5.5)$$

Ingersoll and Zobel [26] provide the solution of equation (5.1) for the transfer of heat from a point source at $r=r'$ having strength Q such that $T_0 \rightarrow \frac{Q/\rho_l C_l}{4\pi a^3/3}$ at time $t = 0$ where a is the radius of the point source.

$$T_l(r, t) = \frac{Q/\rho_l C_l}{8(\pi \kappa_l t)^{3/2}} \exp - \left[\frac{(r-r')^2}{4 \kappa_l t} \right] \quad (5.6)$$

Carslaw and Jager [27] provide the solution of equation (5.1) for the transfer of heat from a ring source of strength Q' at a radius r' in the plane $Z'=0$ at time $t=0$ by considering the ring source as being composed of point sources of strength Q which are distributed round the circle $r=r'$

$$\theta'_l(r, z, t) = \frac{Q'/\rho_l C_l}{8(\pi \kappa_l t)^{3/2}} \exp - \left[\frac{r^2 + r'^2 + z^2}{4 \kappa_l t} \right] I_0 \left(\frac{r r'}{2 \kappa_l t} \right) \quad (5.7)$$

Interpreting this solution to suit the problem by putting:

$Z=0$, $S=r$, $\tau=t$, $R_d=r'$ and $\theta'_l = T_l - T_{sat}$, then equation (5.7) becomes

$$\theta'_l(S, \tau) = \frac{Q'/\rho_l C_l}{8(\pi \kappa_l \tau)^{3/2}} \exp - \left[\frac{S^2 + R_d^2}{4 \kappa_l \tau} \right] I_0 \left(\frac{S R_d}{2 \kappa_l \tau} \right) \quad (5.8)$$

The relationship between the time elapsed from bubble departure $(\tau - \tau_g)$ and the distance which the disturbance has moved from the ring source $(S - R_d)$ can be obtained from equation (5.8) as shown in Appendix (C). However the temperature disturbance propagated outward in the radial direction through the surrounding liquid close to the heating surface can be approximated by

$$(S-R_d) = 2 \sqrt{\kappa_l (\tau - \tau_g)} \quad (5.9)$$

Equation (5.9) can be rewritten for water by substituting the value of the thermal diffusivity $\kappa_l = 1.685 \times 10^{-4} \text{ mm}^2/\text{ms}$ for boiling water at atmospheric pressure to obtain the relationship

$$(S-R_d) = 0.026 \sqrt{(\tau - \tau_g)} \quad (5.10)$$

A comparison between the experimental findings and the predictions of the theoretical model based upon heat diffusion through the water represented by equation (5.10) is shown in figure (41). The predicted values of the relationship represented by equation (5.10) imply very slow heat propagation because the water has a low value of thermal diffusivity.

5.2.2 Propagation of Pressure Pulse

The interaction of the nucleation phenomena at adjacent sites was treated in this model by considering the disturbance of a pressure pulse caused by the rapid growth of a bubble as shown schematically in figure (42). After the bubble detaches from the heating surface, the pressure pulse starts to propagate outward in a radial direction. The disturbance created consists of compression and rarefaction pressure pulses.

Throughout this derivation the following assumptions were considered:

1. Nuclei capable of being activated exist at surrounding

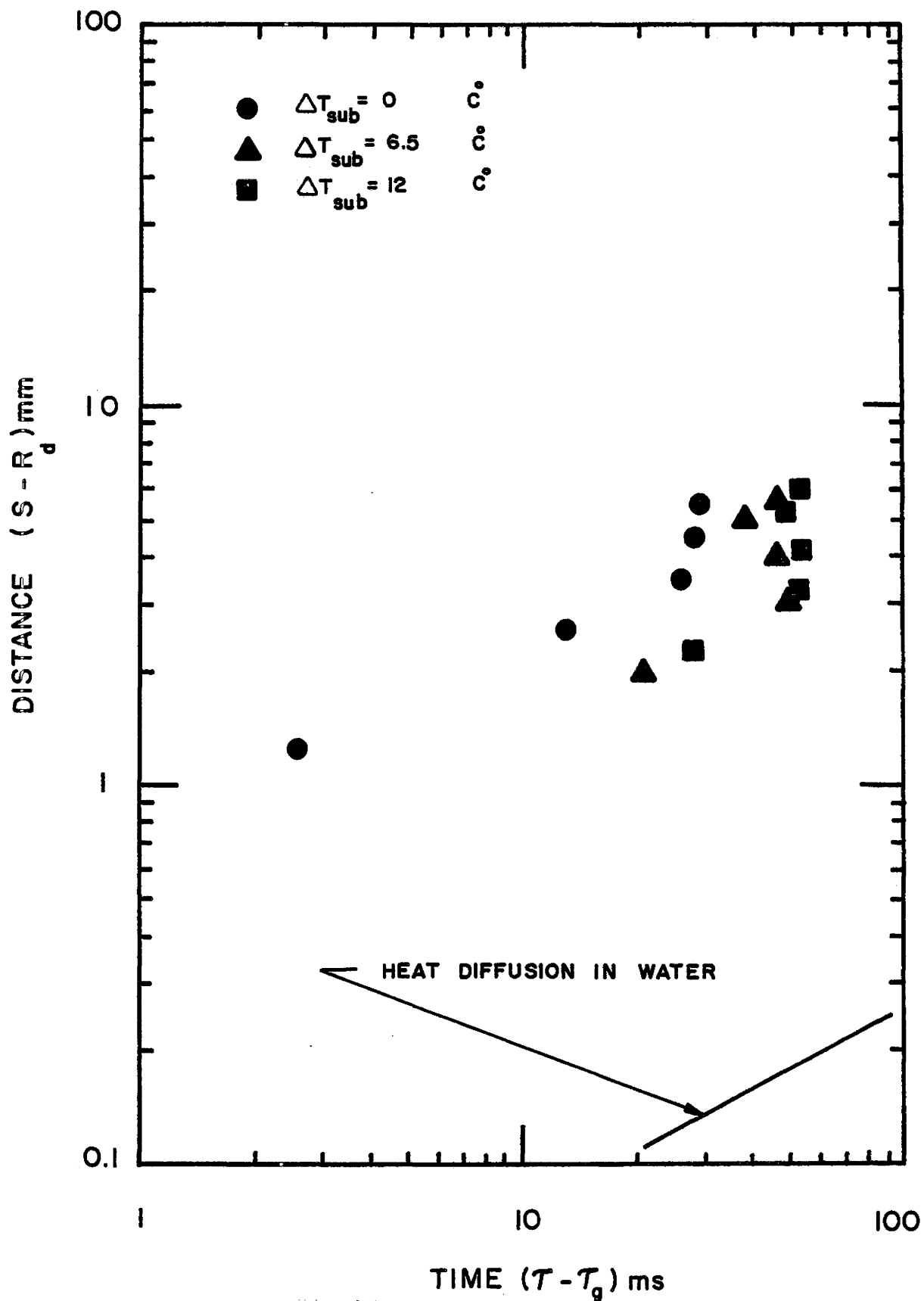


Figure (41). Comparison Between the Theoretical Prediction for Heat Diffusion in the Water and the Experimental Findings

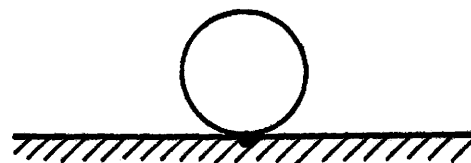
NUCLEUS STANDING AT THE
CAVITY MOUTH



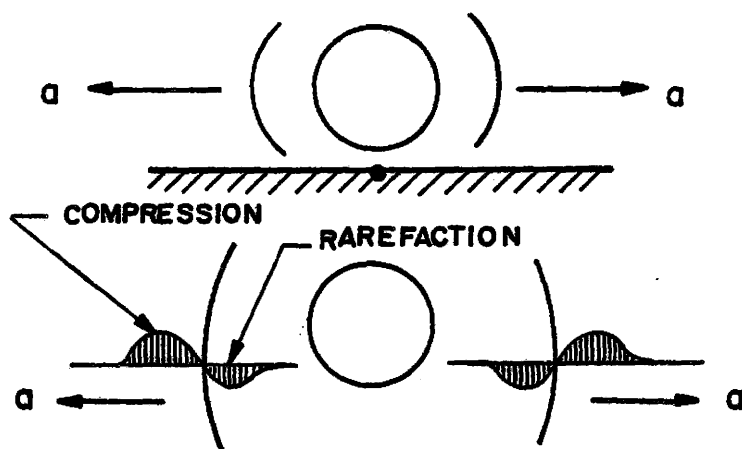
EARLY STAGE OF BUBBLE
GROWTH PERIOD



END OF BUBBLE GROWTH
PERIOD



BUBBLE DETACHMENT AND
THE FORMATION OF A
PRESSURE PULSE



PRESSURE PULSE PROPAGATION

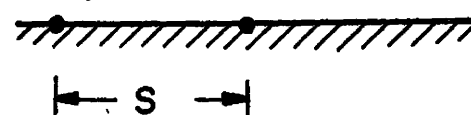


Figure (42). Pressure Pulse Propagation Originating from an Active Nucleation Site

nucleation sites at distances S_1, S_2, \dots

2. Only the pair of sites being investigated interact with each other.
3. The pressure pulse propagation has been assumed to start at the end of the bubble growth period.
4. The liquid pressure around the nucleus at the neighbouring active site decreases as the pressure pulse passes it.

For a nucleus to become a seed for subsequent bubble growth, the size of the nucleus must exceed that of thermodynamic equilibrium corresponding to the state of the liquid. The condition for thermodynamic equilibrium at a vapour-liquid interface in a liquid can be written as

$$P_v - P_l = \sigma \left(\frac{1}{R_1} + \frac{1}{R_2} \right) \quad (5.11)$$

where R_1 and R_2 are the principal radii of curvature of the interface. For a spherical nucleus of radius R , equation (5.11) becomes

$$P_v - P_l = \frac{2\sigma}{R} \quad (5.12)$$

When the liquid pressure around the nucleus decreases due to the pressure pulse propagation effect, $\Delta P_l < 0$ the force created by the difference in pressure between the vapour and the liquid exceeds the surface tension force, $P_v - P_l > \frac{2\sigma}{R}$ and causes the bubble to start to grow.

The propagation velocity in a single component two-phase mixture has been studied by Karplus [28], Davies [29], Gouse

and Brown [30] and Grolmes and Fouske [26]. Their experimental and theoretical results show that although the velocity of the pressure pulse for the liquid state was high, the velocity of the pressure pulse in a single-component two-phase mixture containing a small amount of vapour was extremely low. The velocity of pressure pulse propagation for a pure substance is usually found by evaluation of the thermodynamic derivative

$$a^2 = g_0 \left(\frac{\partial P}{\partial \rho} \right)_s \quad (5.13)$$

where a is the pressure pulse propagation velocity.

Grouse and Brown [30] determined the velocity of pressure pulse propagation in a single-component mixture (water-vapour) using a finite difference form

$$a^2 = g_0 \left(\frac{\Delta P}{\Delta \rho} \right)_s \quad (5.14)$$

A state (quality) was selected in the two-phase region along a given constant pressure line. A second pressure was chosen, and a second state, having the entropy of the first state was found. The derivative in equation (5.14) could then be evaluated. Some general characteristics can be obtained from a log-log plot of pressure and density values as shown in figure (43). Two typical constant-entropy lines are presented in figure (43) for conditions near the saturated liquid and the saturated vapour states. Two general conclusions can be drawn; the constant entropy lines have a continuous slope in both the single-phase and the two-phase regions, with a

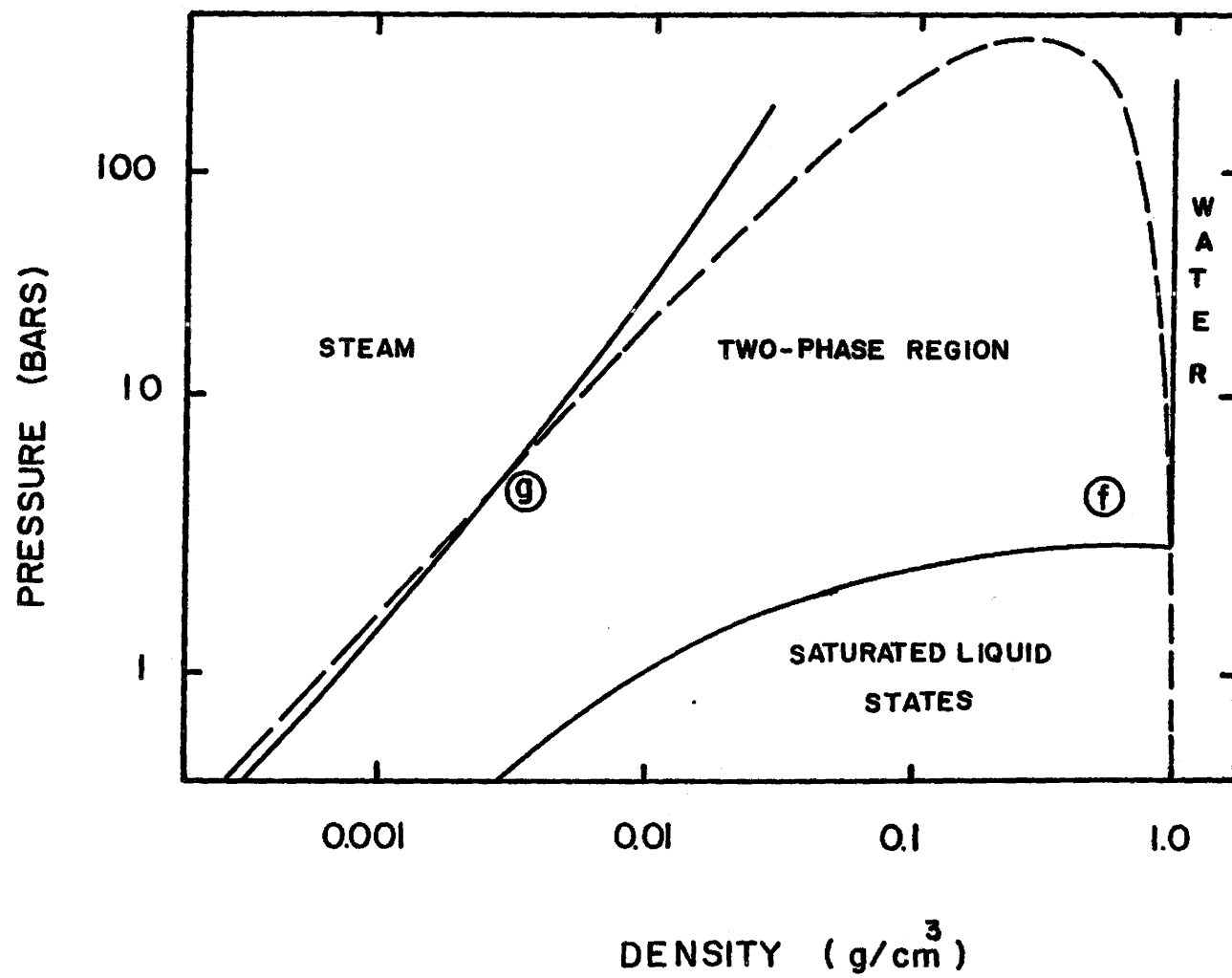


Figure (43). Pressure-Density Diagram for Water

discontinuity of slope at the phase boundaries. For the saturated liquid state there is an extremely large change in slope across the phase boundary. This indicates that although the velocity of sound for the liquid state is high, the velocity of sound for a two-phase state which contains a small amount of vapour will be extremely low. Accurate thermodynamic data are an obvious prerequisite. Since thermodynamic data are usually given in terms of specific volume rather than density, equation (5.13) can be rewritten as

$$a^2 = - g_o v^2 \left(\frac{\partial P}{\partial v} \right)_s \quad (5.15)$$

It is of interest to consider an alternate form of equation (5.15). Using classical thermodynamics, equation (5.9) becomes

$$a^2 = g_o v^2 \left(\frac{\partial s}{\partial v} \right)_p \left(\frac{\partial s}{\partial v} \right)_T \left(\frac{\partial T}{\partial s} \right)_v \quad (5.16)$$

Since constant-pressure and temperature lines are coincident in the two-phase region, it follows that

$$\left(\frac{\partial s}{\partial v} \right)_p = \left(\frac{\partial s}{\partial v} \right)_T \quad (5.17)$$

and

$$\left(\frac{\partial s}{\partial v} \right)_p = \frac{s_g - s_f}{v_g - v_f} = \frac{s_{fg}}{v_{fg}} \quad (5.18)$$

Thus, equation (5.6) becomes

$$a^2 = g_o \left(\frac{v}{v_{fg}} \right)^2 (s_{fg})^2 \left(\frac{\partial T}{\partial s} \right)_v \quad (5.19)$$

The finite-difference forms of equation (5.19) requires the evaluation of an entropy change for a constant-volume process between two saturation temperatures in the two-phase region. The mass quality of a two-phase state, x is defined as

$$x = \frac{m_v}{m_v + m_l} \quad (5.20)$$

The specific volume for such a state can be written in terms of quality x ,

$$v = v_f + x \cdot v_{fg} \quad (5.21)$$

so that equation (5.19) becomes

$$a^2 = g_o \left[\frac{v_f}{v_{fg}} + x \right]^2 (s_{fg})^2 \left(\frac{\partial T}{\partial s} \right)_v \quad (5.22)$$

The results of the pressure pulse propagation velocity obtained by Karplus [28] are shown in figures (44) and (45). In figure (44) the velocity of the pressure pulse propagation is shown as a function of saturation temperature and quality in the two-phase region. Along the saturated-vapour line, the values of the velocity of the pressure pulse propagation are generally between 300 and 600 m/s, consistent with normal expectations for the velocity of propagation in pure steam. As the quality of the two-phase state decreases, the velocity of the pressure pulse propagation decreases rapidly. For states along the saturated-liquid line the propagation velocity increases from the value of 0.3 m/s at low temperature to a

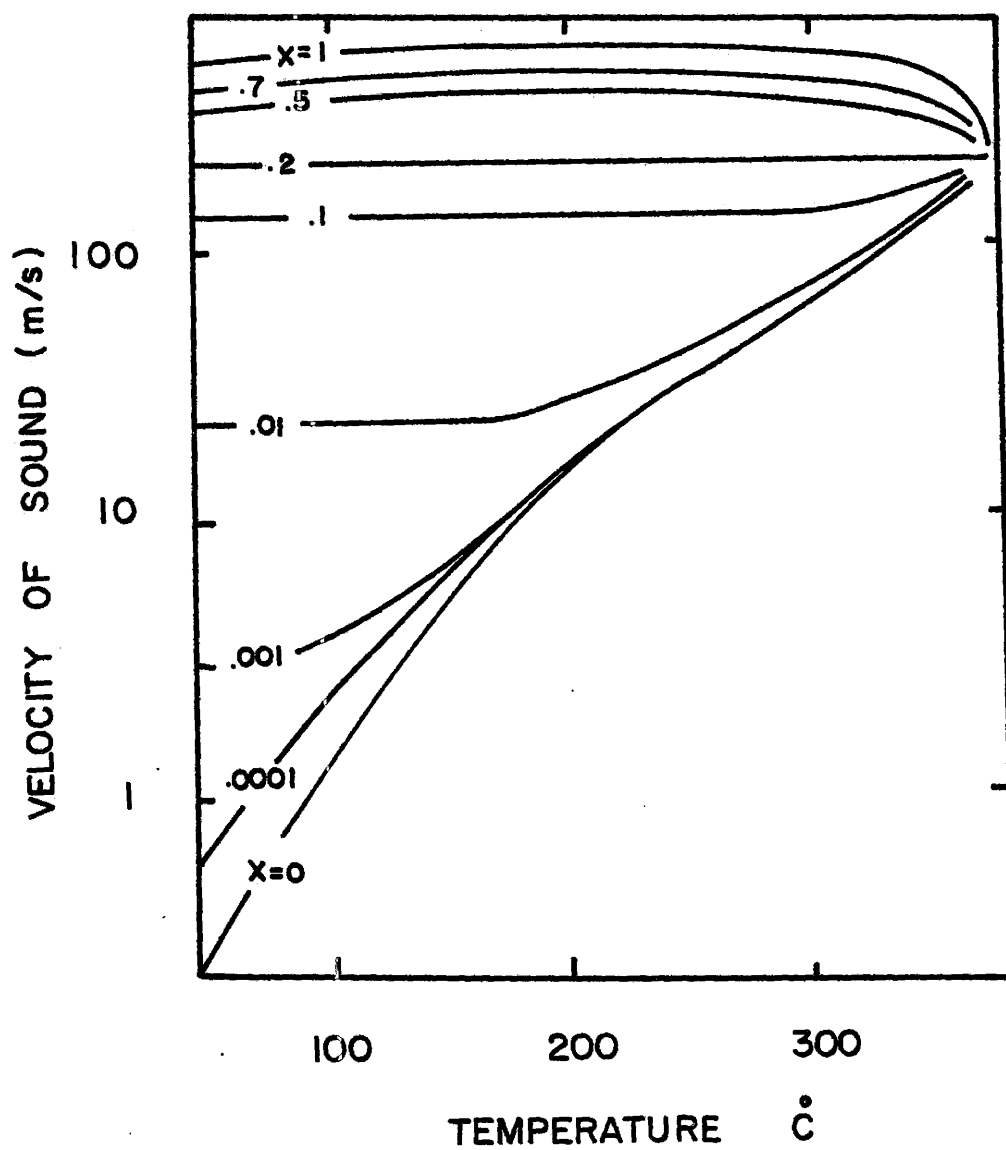


Figure (44). Velocity of Sound in Two-Phase Region for Water

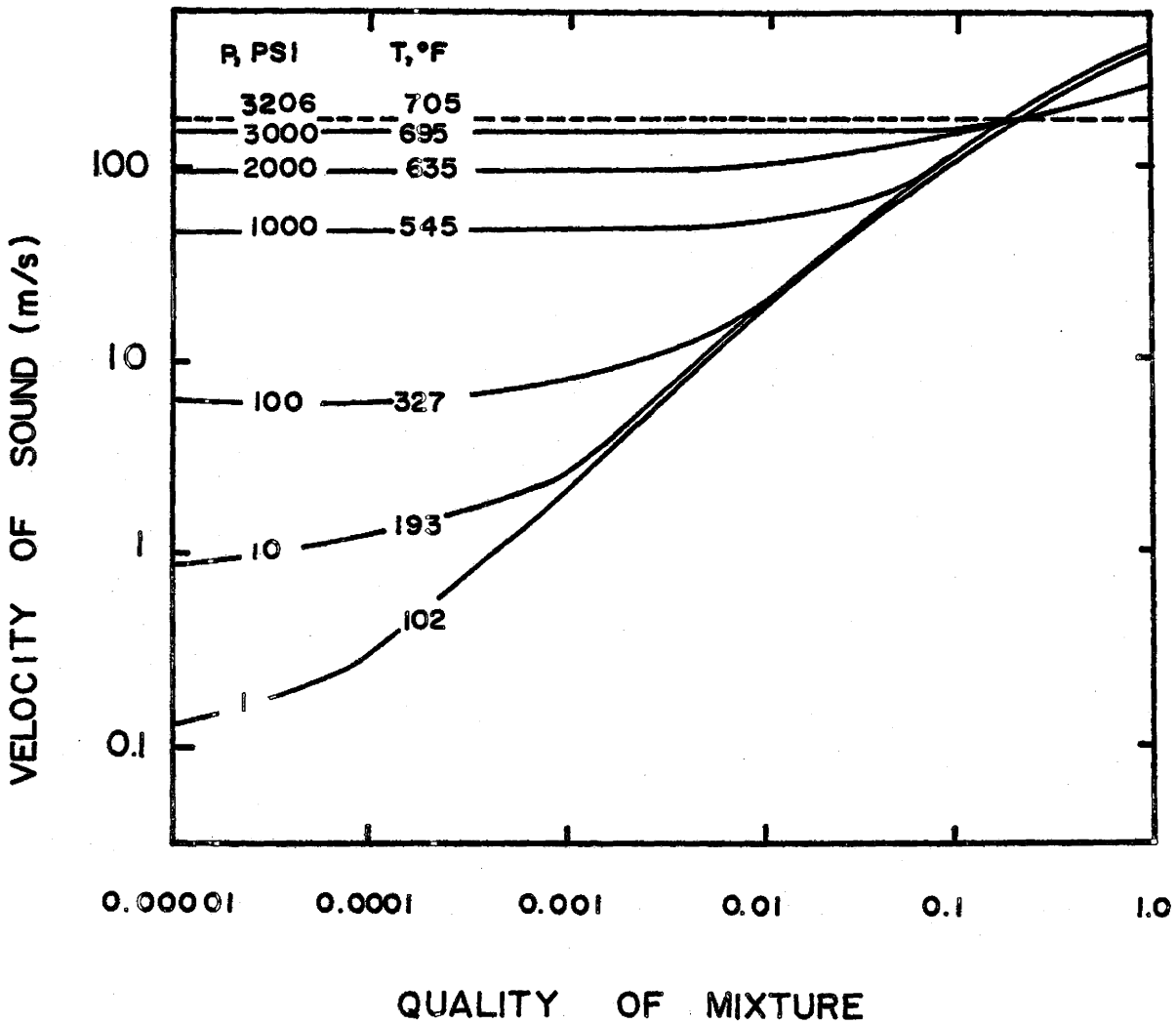


Figure (45). Effect of Quality on Velocity of Sound in Two-Phase Region for Water

maximum at about 150 m/s near the critical state. For the two-phase mixture at the atmospheric pressure the velocity of the pressure pulse propagation at quality 0.001 is 3 m/s.

In the present study the calculation of the pressure pulse propagation velocity was based on equation (5.22). All physical properties for boiling water were considered at the atmospheric pressure. The quality x was calculated as follows.

$$x = \frac{1}{1 + \frac{\rho_l}{\rho_g} \frac{v_l}{v_v}} \quad (5.23)$$

where

$$\frac{v_g}{v_l} = \frac{1}{B-1} \quad (5.24)$$

and

$$B = \frac{15}{\pi D_d^2 \frac{N}{A_T} \frac{\tau_g}{\tau_T}} \quad (5.25)$$

The details pertaining to the computation of the quality x are presented in Appendix (E).

In the experimental apparatus used it was not possible to measure the bubble departure size D_d or the bubble growth period τ_g and therefore these parameters had to be predicted. The details of the determination of bubble departure size, bubble growth period, bubble cycle time and the active site density at the lower level of heat flux can be found in Appendix (D).

For the value of quality obtained ($x = 0.000075$), the pressure pulse propagation velocity is 1.3 m/s. A comparison

between the experimental findings and the predictions of the pressure pulse propagation model is presented in figure (46). The predicted values of the relationship $(S-R_d)$ versus $(\tau-\tau_g)$ using the pressure pulse propagation model gave higher values than the experimental findings.

5.2.3 Heat Diffusion Through Surface

The approach used in the derivation of the present model was based upon heat diffusion through the surface. The local instantaneous heat transfer coefficient on a heat transfer surface has been studied by Barakat and Sims [31]. One of their curves is represented in figure (47), and shows that during the early stages of bubble growth, while there is an outward movement of the flow field around the bubble interface as shown in figure (48.a), the local heat transfer coefficient \bar{h} increases to maximum (at $\tau/\tau_g \approx 0.5$) and then decreases as the bubble interface velocity decreases. The heat transfer coefficient goes through a minimum at R ($\tau/\tau_g \approx 0.7$). When the bubble leaves the heating surface the liquid moves inward as shown in figure (48.b), causing the heat transfer coefficient at the heating surface in the vicinity of the bubble periphery to attain another maximum (at $\tau/\tau_g \approx 1.0$) at a period approximately equal to the bubble growth time. After the bubble detachment from the heating surface, the heat transfer coefficient decreases monotonically to its original value. The interesting stage in Barakat and Sims' [31] studies as far as the present investigation is concerned occurs when the bubble leaves the

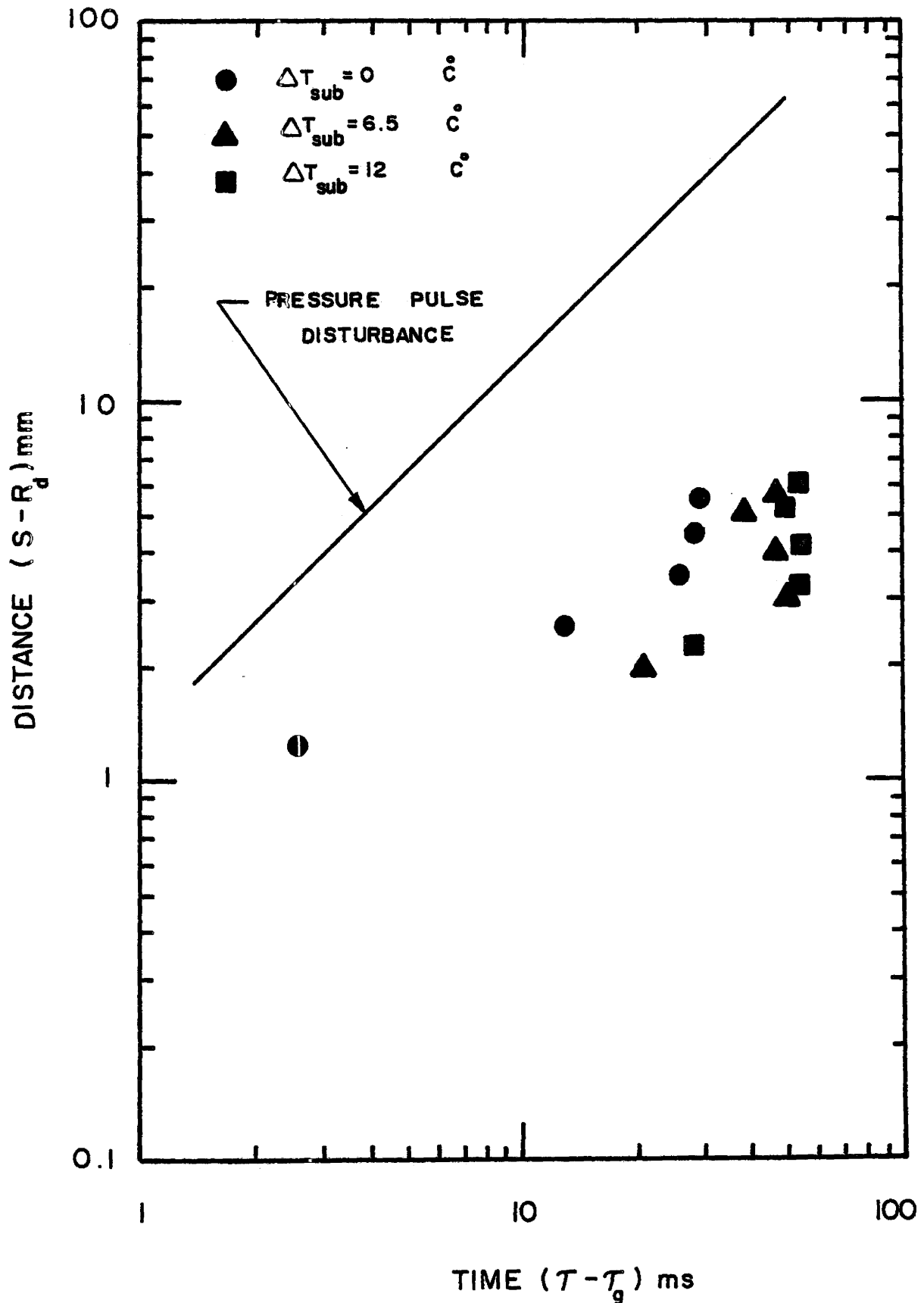


Figure (46). Comparison Between the Theoretical Prediction of the Pressure Pulse Disturbance and the Experimental Findings

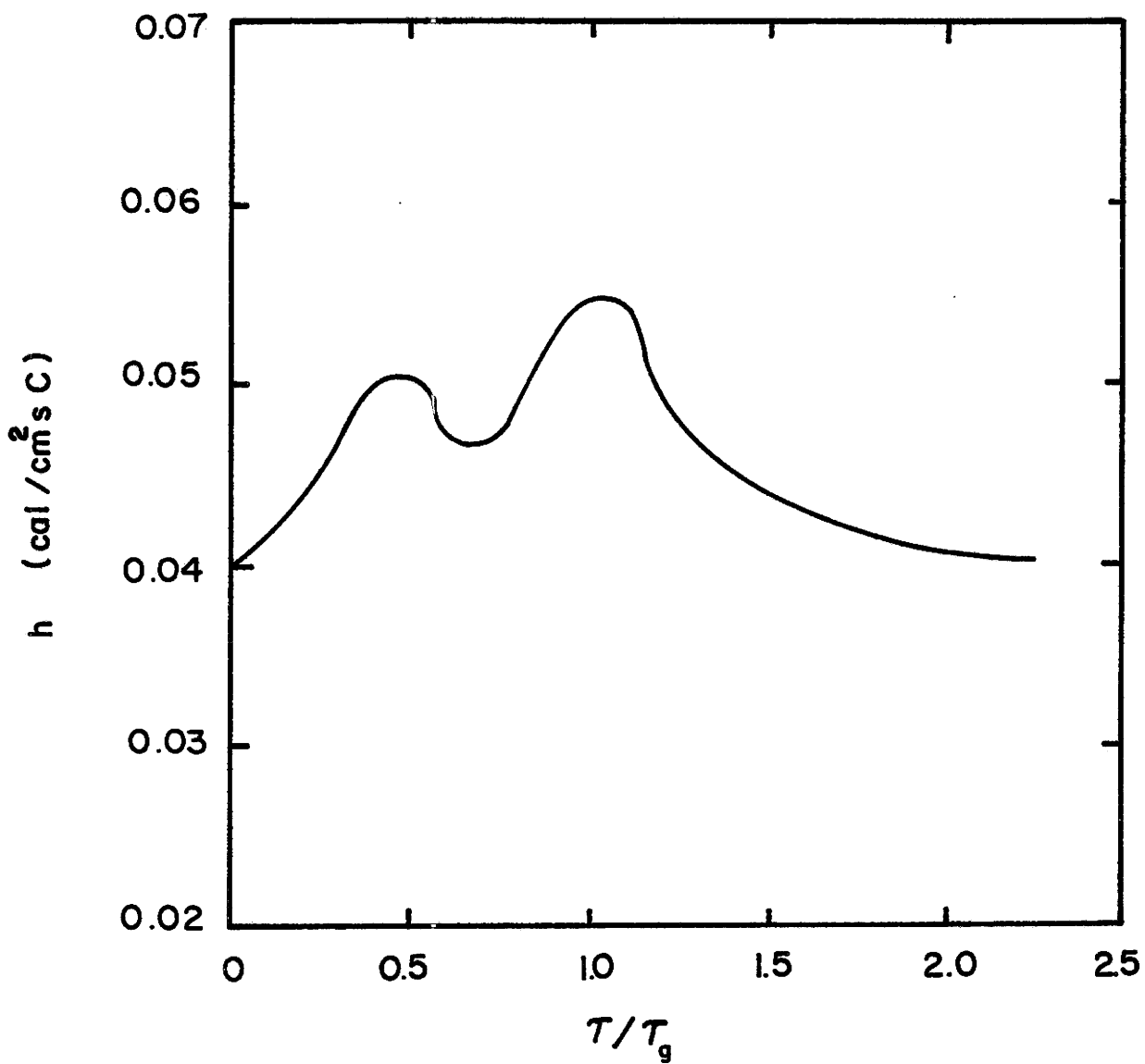


Figure (47). Heat Transfer Coefficient Obtained by Barakat and Sims

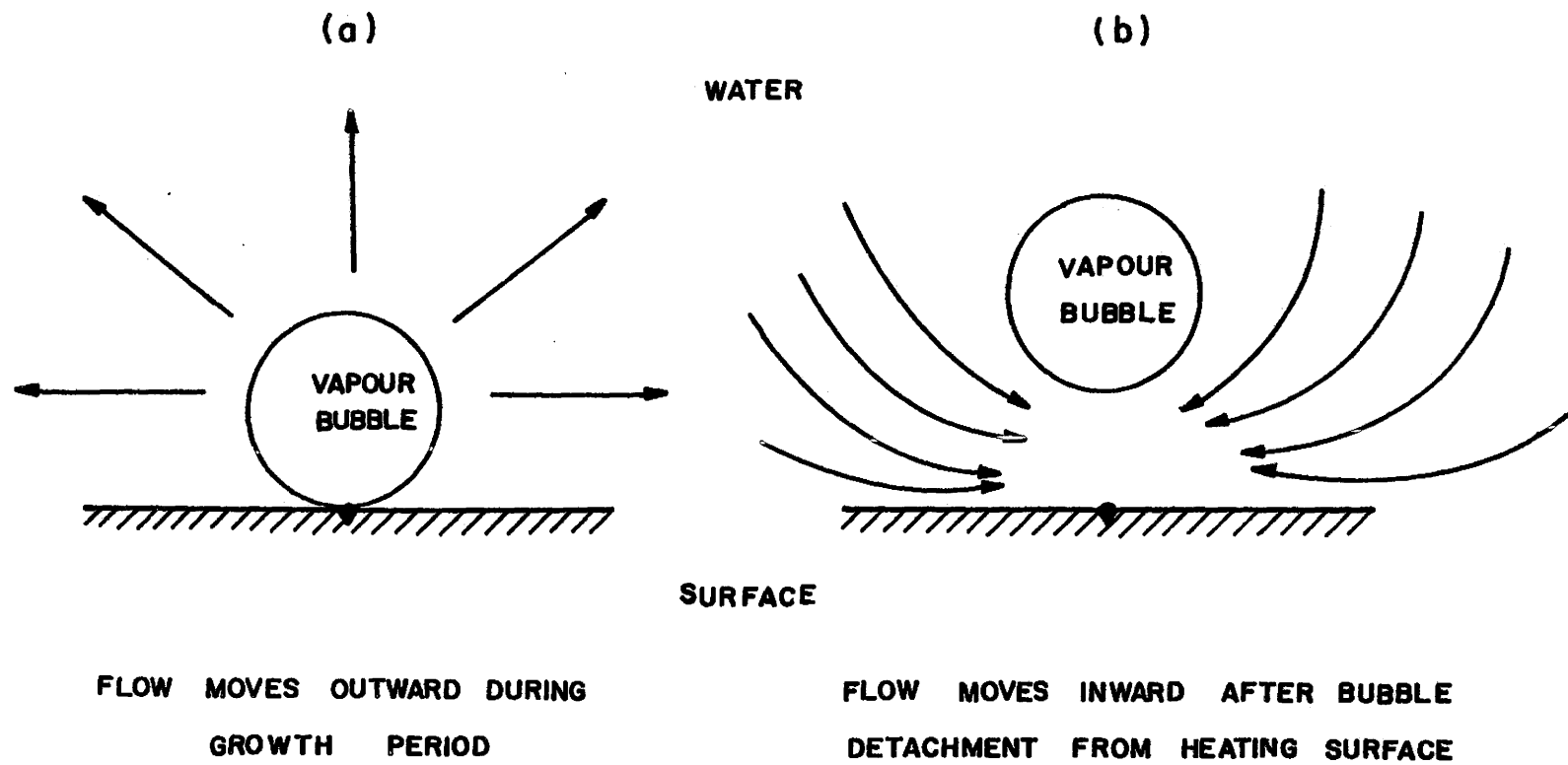


Figure (48). The Directions of the Flow Around a Bubble During Growth and After Bubble Detachment

heating surface.

The temperature field around a growing vapour bubble was presented by Beer et al. [25] as discussed in 5.2.1. When the bubble starts to grow, the superheated liquid layer at the heating surface is pushed away from the nucleation site and high temperature liquid accumulates at the periphery of the growing bubble. The corresponding temperature field in the surface (copper and steel) around an active site were computed by Beer et al. [25] as well. The temperature of the surface was distorted as shown in figures (49) and (50), at $\tau_w = 0$ ms, because most of the heat transfer to the growing bubble comes from the heating surface. Figure (49) shows that at 20 ms after bubble detachment from the copper heating surface, there has not been enough heat conducted in the axial direction to achieve surface temperature recovery. On the basis of these observations, the phenomenon in the present model has been approximated by an instantaneous transfer of heat to the surface in the form of a ring source surrounding the bubble base. The temperature disturbance which results propagates outward through the heating surface in the radial direction, and the differential equation of heat conduction in cylindrical coordinates was considered most appropriate to describe the heat conduction process adjacent to the surface. The idealized model for the heat conduction in the surface is represented in figure (51) and figure (52) shows the superposition of the temperature distribution resulting from the instantaneous heat source and the temperature

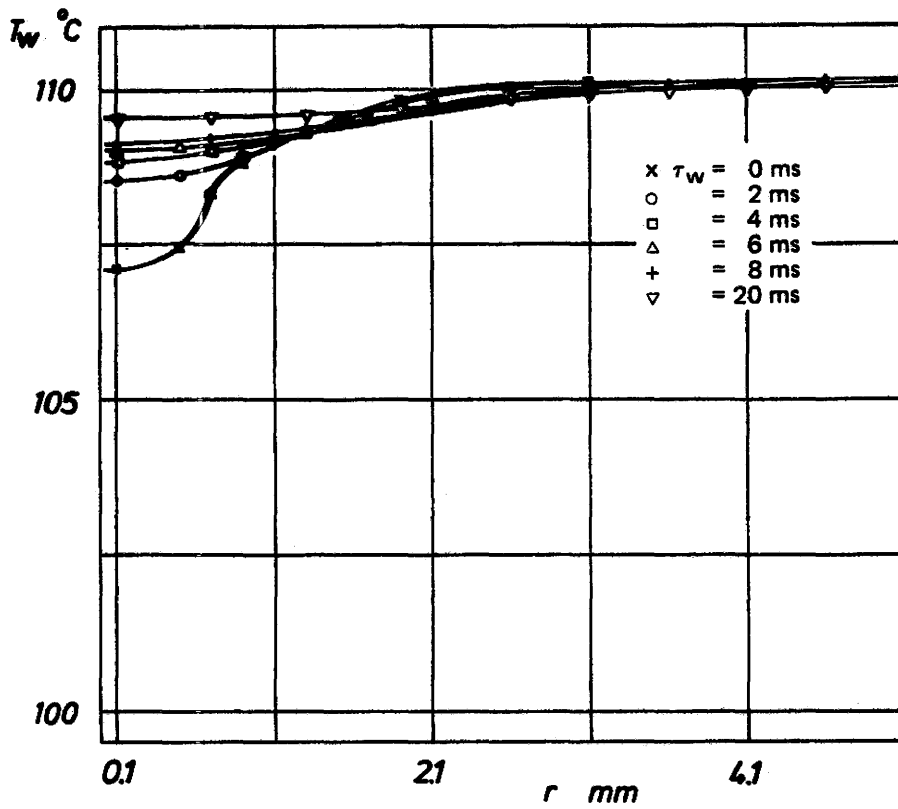


Figure (49). Temperature Distribution in a Copper Heating Wall After Bubble Detachment

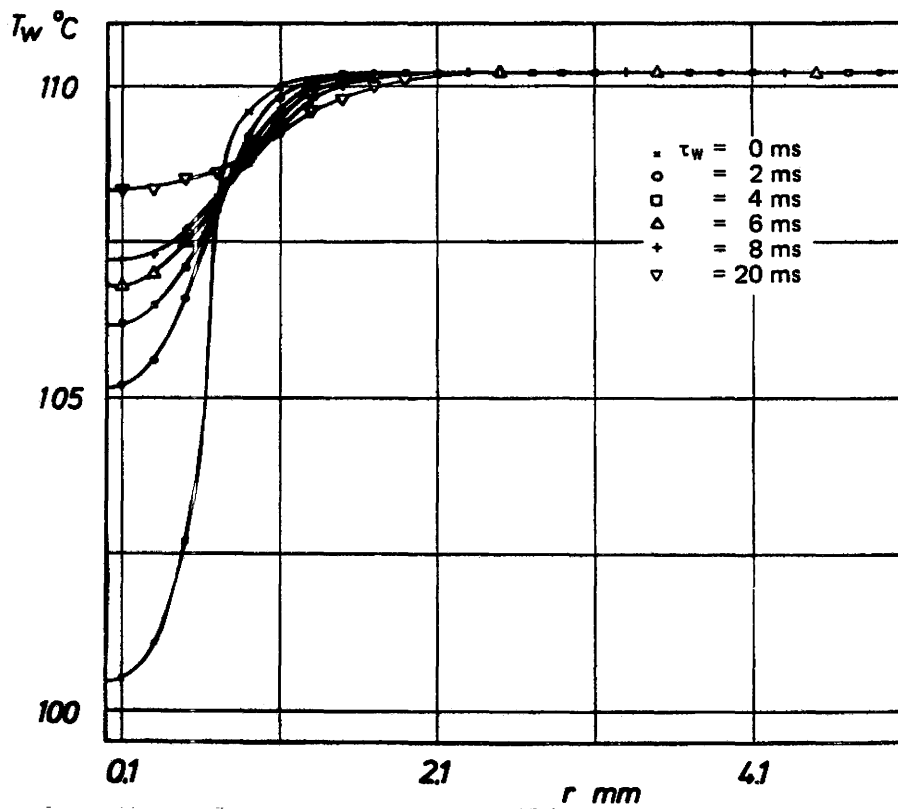


Figure (50). Temperature Distribution in a Steel Heating Wall After Bubble Detachment

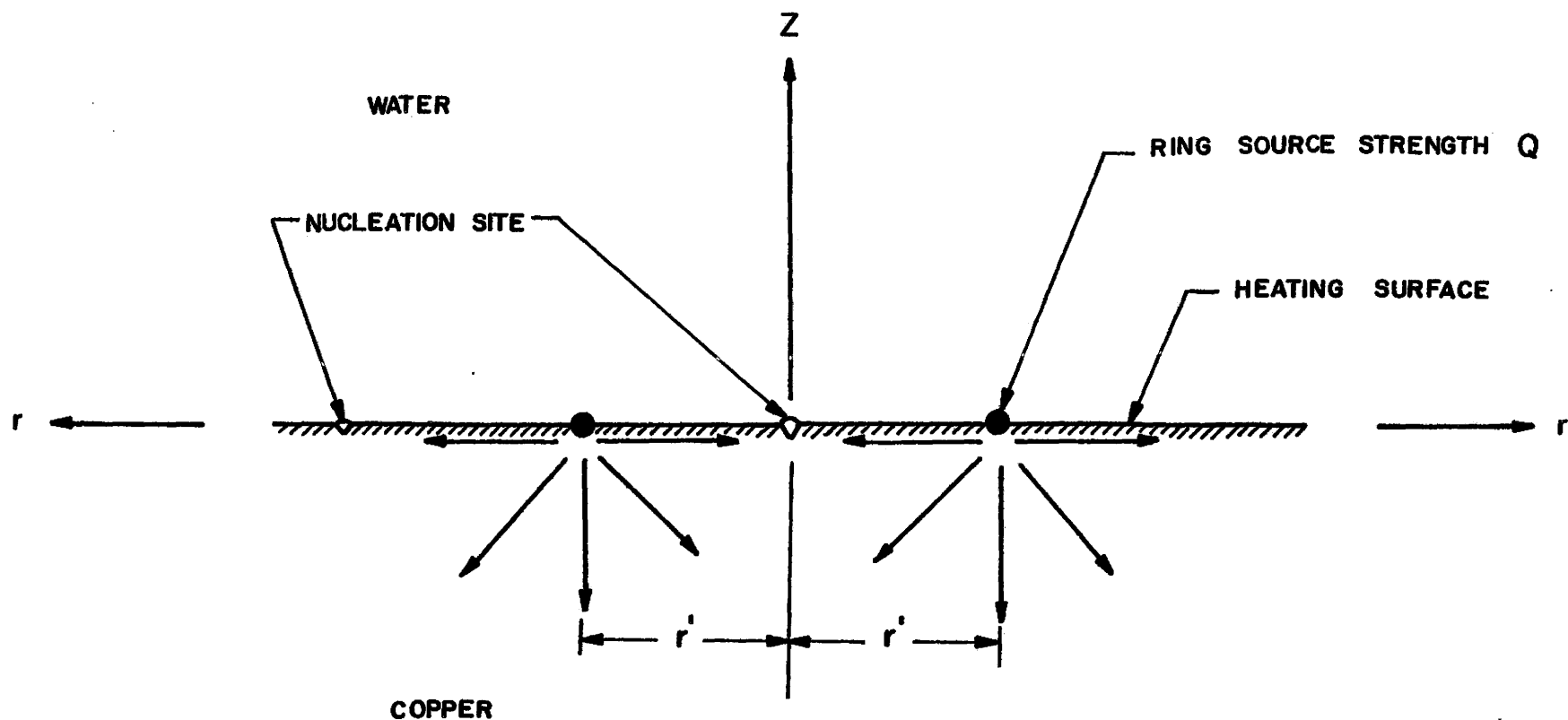


Figure (51). Idealized Model for the Transfer of Heat from an Instantaneous Ring Source to the Heating Surface

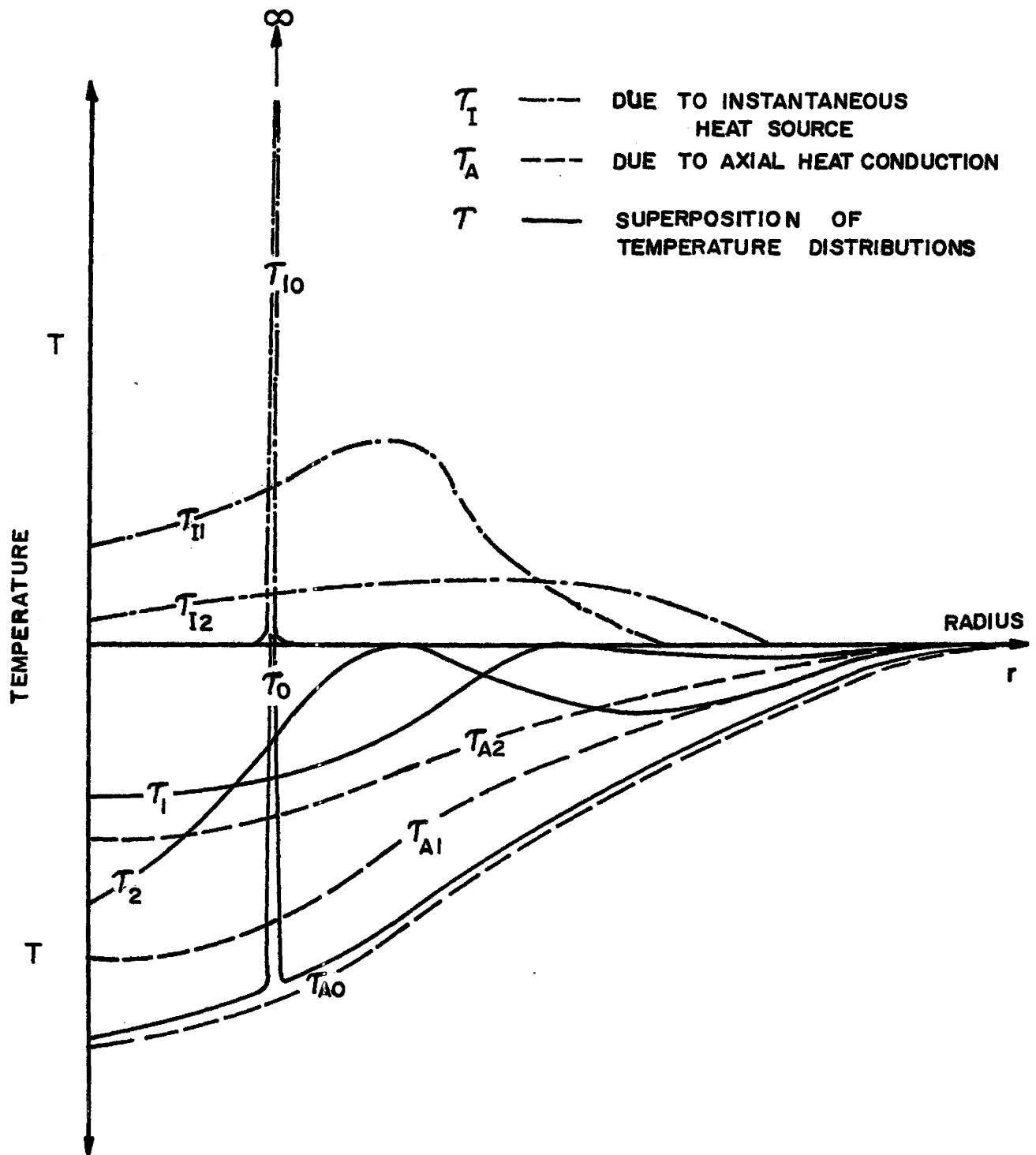


Figure (52) Superposition of Temperature Distributions

distribution resulting from conduction within the heating surface. It is evident that the period required to attain the initial wall temperature depends on the wall material as shown in figures (49) and (50). The temperature disturbance caused by the transfer of heat from an instantaneous ring source can have an effect in materials which have high thermal diffusivity such as copper, but for a material such as steel which has lower thermal diffusivity than the copper, the temperature disturbance will not be as significant. For these materials, the formation of bubbles at adjacent sites may not be related and the regeneration of the initial wall temperature may depend only on the axial heat conduction within the heating surface.

Throughout this derivation the following assumptions were considered:

1. Nuclei capable of being activated exist at surrounding nucleation sites at distances S_1, S_2, \dots
2. Only the pair of active sites being investigated interact with each other.
3. Heat diffusing from an instantaneous ring source through the surface propagates in the radial direction close to the heating surface.
4. For the purposes of analysis, no heat is transferred from the ring source to the surrounding liquid.

Therefore,

$$\rho_s C_s \frac{\partial T_s}{\partial t} = k_s \left[\frac{1}{r} \frac{\partial}{\partial r} \left(r \frac{\partial T_s}{\partial r} \right) \right] \quad (5.26)$$

The initial conditions are:

$$T_s(r, 0) = T_0 \quad r=r' \quad (5.27)$$

$$T_s(r, 0) = 0 \quad r \neq r' \quad (5.28)$$

The boundary conditions are:

$$\frac{\partial T_s(0, t)}{\partial r} = 0 \quad (5.29)$$

$$T_s(\infty, t) = 0 \quad (5.30)$$

The solution of equation (5.26) for an instantaneous transfer of heat from a ring source was provided by Carslaw and Jager [27] as discussed in 5.2.1.

$$T_s(r, z, t) = \frac{Q'/\rho_s C_s}{8(\pi \kappa_s t)^{3/2}} \exp - \left[\frac{r^2 + r'^2 + z^2}{4 \kappa_s t} \right] I_0 \left(\frac{r r'}{2 \kappa_s t} \right) \quad (5.31)$$

Interpreting this solution to suit the problem by putting

$z=0$, $S=r$, $\tau=t$, $R_d=r'$ and $\theta'_s = T_s$, then equation (5.31) becomes

$$\theta'_s(S, \tau) = \frac{Q'/\rho_s C_s}{8(\pi \kappa_s \tau)^{3/2}} \exp - \left[\frac{S^2 + R_d^2}{4 \kappa_s \tau} \right] I_0 \left(\frac{S R_d}{2 \kappa_s \tau} \right) \quad (5.32)$$

The relationship between the time elapsed from bubble departure $(\tau - \tau_g)$ and the distance from the ring source $(S - R_d)$ can be obtained from equation (5.32) as discussed in Section 5.2.1.

$$(S - R_d) = 2 \sqrt{\kappa_s (\tau - \tau_g)} \quad (5.33)$$

Equation (5.33) can be rewritten for copper by substituting the value of the thermal diffusivity $\kappa_s = 8.15 \times 10^{-2} \text{ mm}^2/\text{ms}$, to obtain the relationship

$$(S-R_d) = 0.57 \sqrt{(\tau-\tau_g)} \quad (5.34)$$

The prediction of this relationship and the experimental findings are presented in figures (53) and (54). The theoretical prediction of the heat diffusion through the solid gave much better agreement with the experimental findings.

Comparison between the experimental findings and the three proposed theoretical models is presented in figure (55). The first two models failed to give satisfactory agreement with the experimental results, but the theoretical prediction corresponding to heat diffusion through the solid gave good agreement with the experimental findings.

5.3 Implications of the Research

The experimental results obtained at the lower level of heat flux (92.21 kW/m^2) and three different levels of subcooling ($0, 6.5, 12^\circ\text{C}$) showed that the separating distance (S) and the time elapsed (τ) between the start of bubble growth at two neighbouring active sites were uniquely related, such that the time elapsed between the start of bubble growth at the two neighbouring active sites increased with increasing separating distance. For this particular level of heat flux, all the experimental data for the saturated and subcooling boiling conditions plotted as $(S-R_d)$ versus $(\tau-\tau_g)$ tended to draw together

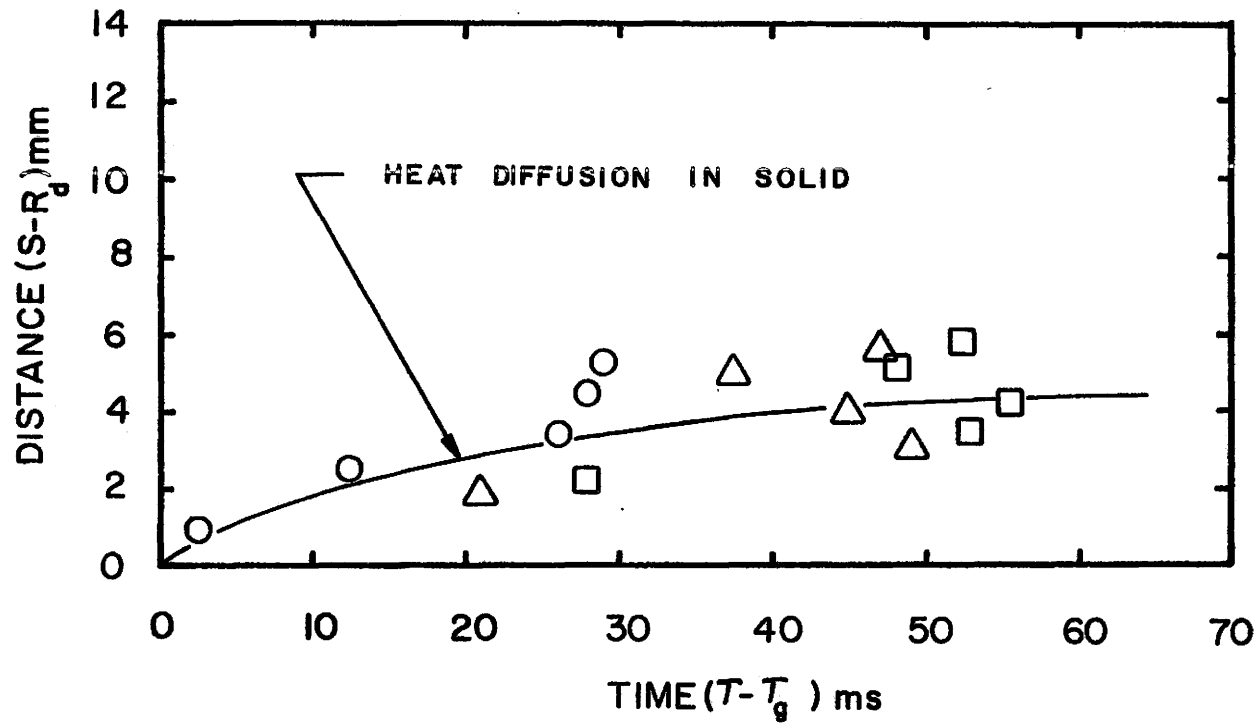


Figure (53)

Comparison Between the Experimental Results and the Prediction of Heat Diffusion in Solid

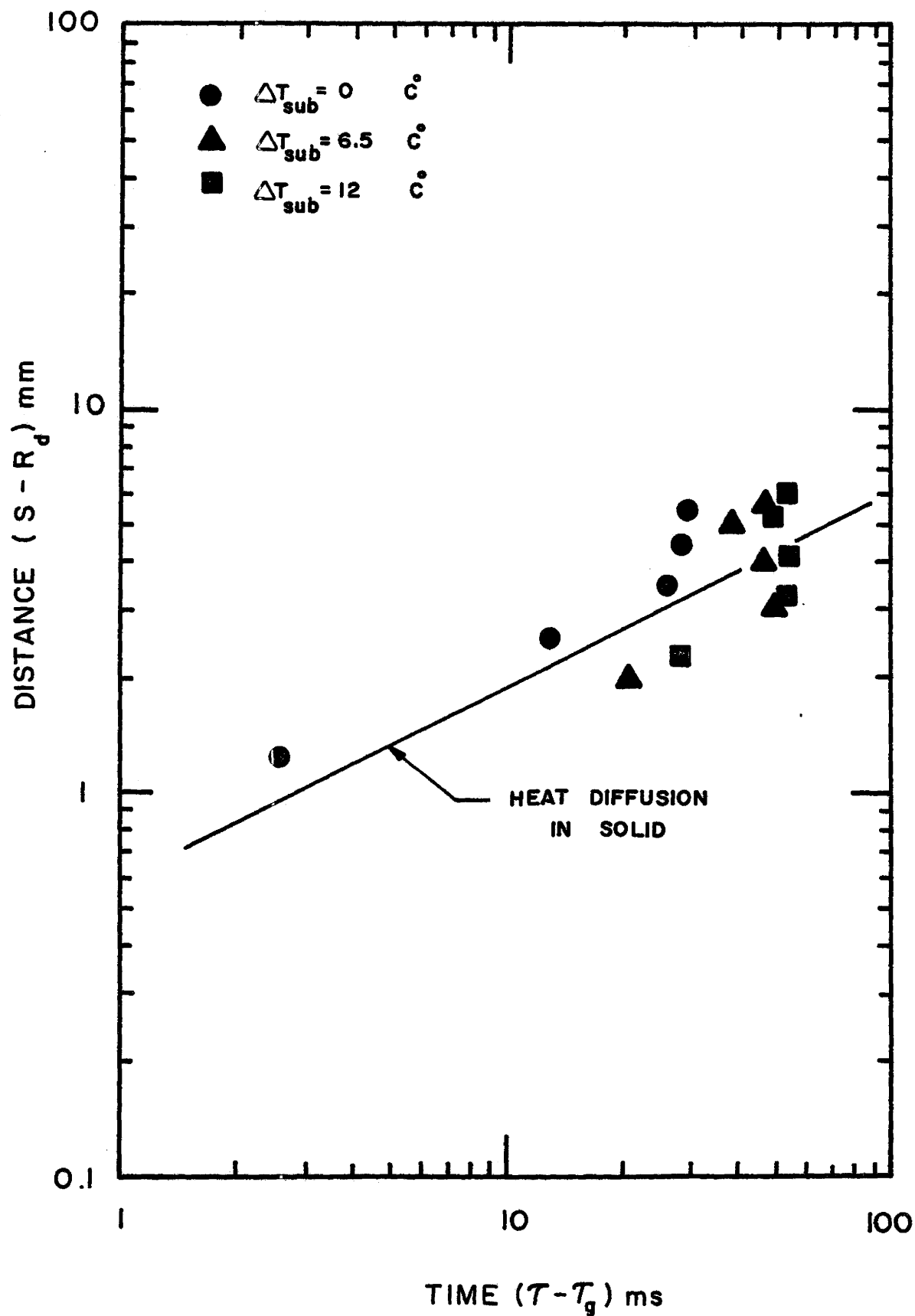


Figure (54). Comparison Between the Theoretical Prediction of the Heat Diffusion in the Solid and the Experimental Findings

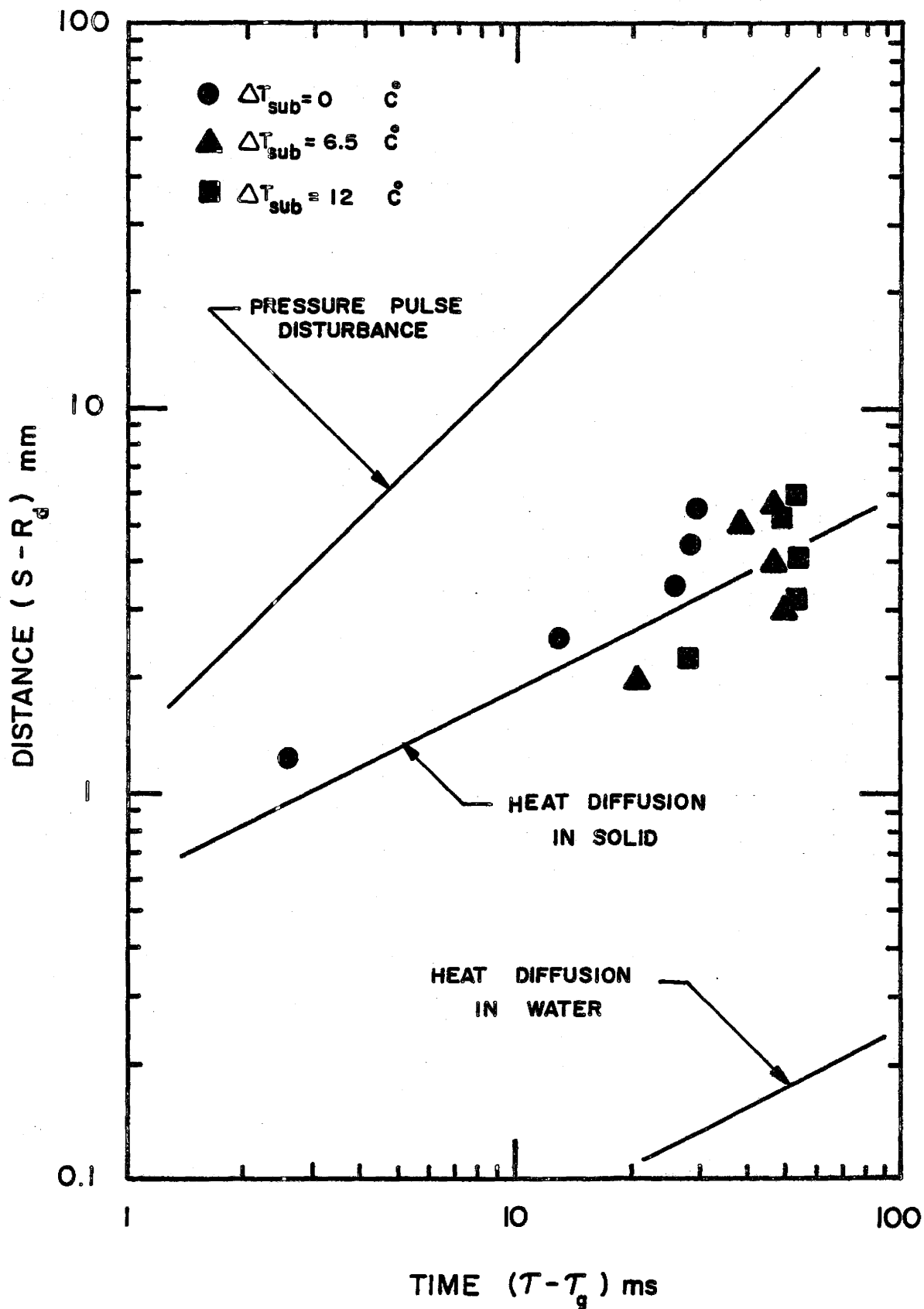


Figure (55). Comparison Between the Three Theoretical Models Predicting the Correlation of the Distance (S - R_d) with Time (τ - τ_g)

into a single curve suggesting that a single relationship might fit the data. A theoretical model involving heat diffusion in the solid close to the heating surface gave good agreement with the experimental findings at the lower level of heat flux suggesting that this might be the mechanism responsible for the activation of the surrounding nucleation sites.

As a result of the research performed, it has been proven that the bubble nucleation phenomenon and the distribution of active nucleation sites are related in a manner which is not yet completely understood. One implication of this interdependence is that the emission of a bubble at a nucleation site is governed by the pattern of bubble emissions of all of its neighbours within a certain as yet undetermined distance and that it is not an isolated event as commonly thought. Henceforth, it will be necessary to think in terms of "area averaged" bubble emission frequencies in the formulation of nucleate boiling heat transfer models. Obviously more research is required. The investigation reported herein only represents the first step in a series of experimental and theoretical studies to be done for the various liquid/surface combinations at different levels of heat flux and subcooling with a number of different applied pressures to investigate more general situations.

It is felt that this sort of investigation will advance our knowledge of the boiling phenomena and help to fill the gaps between the actual behaviour and the existing models in the prediction of boiling heat transfer.

REFERENCES

1. Chekanov, V. V., "Stavropol", Translated from Tephofizika Vysokikh Temperature, V. 15, No. 1, p. 121, 1977.
2. Sultan, M. and Judd, R. L., "Spatial Distribution of Active Sites and Bubble Flux Density", Journal of Heat Transfer, ASME, V. 100, No. 1, p. 56, 1978.
3. Becker, R. and Doring, Am. Phys., 24, p. 719, 1935.
4. Volmer, M., "Kinetics of Phase Formation", Ref. ATI No. 81935 (F-TS-6068-RE), Clearinghouse Fed. Sci. Tech. Inform., Springfield, Virginia.
5. Frenkel, J., "Kinetic Theory of Liquids", Dover, New York, 1955.
6. Corty, C. and Foust, A. S., "Surface Variables in Nucleate Boiling", Chem. Eng. Progress Symp. Series, 51, No. 17, p. 1, 1955.
7. Bankoff, S. G., "Ebullition from a Solid Surface in the Absence of Pre-existing Gaseous Phase", Trans. ASME, 79, p. 735, 1957.
8. Clark, H. B., Streng, P. S. and Westwater, J. W., "Active Sites for Nucleate Boiling", Chem. Eng. Progress, Symp. Series 55, p. 103, 1959.
9. Westwater, J. W. and Gaertner, R. F., "Population of Active Sites in Nucleate Boiling Heat Transfer", Chem. Eng. Progress Symp. Series 30, No. 56, 1960.
10. Heled, Y. and Orell, A., "Characteristic of Active Sites in Pool Boiling", Int. J. of Heat and Mass Transfer, V. 10, p. 553, 1967.
11. Hsu, Y. Y., "On the Size of Active Nucleation Cavities on a Heating Surface", Journal of Heat Transfer, ASME, Series C, V. 84, No. 3, 1962.
12. Nail, J. P., Vachon, R. I. and Morehouse, J., "An SEM Study of Nucleate Sites in Pool Boiling from 304 Stainless-Steel", Journal of Heat Transfer, ASME, 1974.

13. Judd, R. L., Private Communication.
14. Sgheiza, J. E. and Myers, J. E., "Infrared Studies of Nucleate Boiling", AICh.E. Symp. Series 164, V. 73, 1977.
15. Raad, T. and Myers, J. E., "Nucleation Studies in Pool Boiling on Thin Plates Using Liquid Crystals", AICh.E. Symp. Series 17, V. 260, 1971.
16. ASME Heat Transfer Division, "Two Phase Flow Instrumentation", Aug., 1969.
17. Iida, Y. and Kobayasi, K., "An Experimental Investigation on the Mechanism of Pool Boiling Phenomena by a Probe Method", 4th Int. Heat Transfer Conference, Paris, 1970.
18. Shoukri, M. and Judd, R. L., "A Theoretical Model for Bubble Frequency in Nucleate Pool Boiling Including Surface Effects", Sixth Int. Heat Transfer Conference, Canada, 1978.
19. Judd, R. L., and Hwang, K. S., "A Comprehensive Model for Nucleate Pool Boiling Heat Transfer", Journal of Heat Transfer, ASME, V. 93, No. 1, 1976.
20. Wiebe, J. R., "Temperature Profiles in Subcooled Nucleate Boiling", M.Eng., Mech. Eng. Dept., McMaster University, Canada, 1970.
21. Sultan, M., "Spatial Distribution of Active Sites and Bubble Flux Density", M.Eng., Mech. Eng. Dept., McMaster University, Canada, 1977.
22. George, E. P. Box and Gwilyn M. Jenkins, "Time Series Analysis Forecasting and Control", 1970.
23. Moissis, R. and Berenson, P. J., "The Hydrodynamic Transition in Nucleate Boiling", ASME Series C, V. 85, 1963.
24. Kirby, D. B. and Westwater, J. W., "Bubble and Vapour Behaviour on a Heated Horizontal Plate During Pool Boiling Near Burnout", Chem. Eng. Progress Symp. Series, V. 61, No. 57, 1965.
25. Hahne, E. and Grigull, U., "Heat Transfer in Boiling", Hemisphere Publishing Corporation, Chapter 2 by Beer, H., Burow, P. and Best, R., 1977.
26. Ingersoll, L. R. and Zobel, O. J., "Heat Conduction", McGraw-Hill, Inc., 1948.

27. Carslaw, H. S. and Jaeger, J. C., "Conduction of Heat in Solids", Oxford, Second Edition, 1973.
28. Karplus, H. B., "Propagation of Pressure Waves in a Mixture of Water and Steam", ARF 4132-12, Armour Research Foundation, Illinois Institute of Technology, Chicago, 16, Illinois, 1961.
29. Davies, A. L., "The Speed of Sound in Mixtures of Water and Steam", AEEW M452.
30. Gouse, S. W. and Brown, G. A., "A Survey of the Velocity of Sound in Two Phase Mixtures, ASME, 64WA/FE-35, 1964.
31. Barakat, S. A. and Sims, G. E., "Heat Transfer in Pool Barbotage", Sixth Int. Heat Transfer Conference, Canada, 1978.
32. Schenck, H., "Heat Transfer Engineering", Prentice-Hall Inc., 1959.
33. Kurihara, H. M., Myers, J. E., "The Effects of Superheat and Surface Roughness on Boiling Coefficients", A.I.Ch.E. Journal, V. 6, No. 1, 1960.
34. Mikic, B. B. and Rohsenow, W. M., "A New Correlation of Pool Boiling Data Including the Effect of Heating Surface Characteristics", Journal of Heat Transfer, ASME, p. 245, 1969.
35. Unal, H. C., "Maximum Bubble Diameter, Maximum Bubble-Growth Time and Bubble-Growth Rate During Subcooled Nucleate Flow Boiling of Water Up to 17.7 MN/m²", Int. Journal of Heat and Mass Transfer, V. 19, p. 643, 1976.
36. Fritz, W., "Maximum Volume of Vapour Bubbles", Zeitschrift fur Physik, V. 36, p. 379, 1935.
37. Staniszewski, B. E., "Nucleate Boiling Bubble Growth and Departure", Technical Report No. 16, DSR 7673, ONR Contract No. 1871 (39) Heat Transfer Laboratory, M.I.T., 1959.
38. Cole, R., "A Photographic Study of Pool Boiling in the Region of Critical Heat Flux", A.I.Ch.E. Journal 6, 4, p. 533, 1960.
39. Cole, R. and Rohsenow, W. M., "Correlation of Bubble Departure Diameters for Boiling Liquids", Chem. Eng. Progress Symp. Series, 65, p. 211, 1969.

40. Rallis, C. J., Greenland, R. V. and Kok, A., "Stagnant Pool Nucleate Boiling from a Horizontal Wire Under Saturated and Subcooled Conditions", The South African Mech. Eng., 1961.
41. Sultan, M., "Thesis Proposal to the Doctoral Supervisory Committee", Mech. Eng. Dept., McMaster University, June, 1979.
42. Hsu, Y. Y. and Graham, R. W., "Transport Processes in Boiling and Two-phase Systems", McGraw-Hill Book Company, 1976.
43. Van Wylen, S., "Fundamentals of Classical Thermodynamics", John Wiley Book Company, 1976.
44. Barakat, S. A., "Flow Patterns and Heat Transfer in Pool Boiling", Ph.D Thesis, University of Manitoba, Winnipeg, Canada, 1977.
45. Lorenz, J. J., "The Effect of Surface Conditions on Boiling Characteristics", Ph.D Thesis, Dept. of Mech. Eng., M.I.T., 1971.
46. Gaertner, R. A., "Photographic Study of Nucleate Pool Boiling on a Horizontal Surface", Journal of Heat Transfer, ASME, p. 17, 1965.
47. Kotake, S., "On the Liquid Film of Nucleate Boiling", Int. Journal of Heat and Mass Transfer, 15, p. 1595, 1970.
48. Shoukri, M., "The Influence of Surface Conditions in Nucleate Boiling", Ph.D. Thesis, Mech. Eng. Dept., McMaster University, Canada, 1977.
49. Thomson, M., "Theoretical Hydrodynamics", MacMillan and Company, Limited, 1969.
50. Bendat, J. S. and Piersol, G. A., "Measurement and Analysis of Random Data", John Wiley Inc., 1966.
51. Jenkins, G. M. and Watts, D. G., "Spectral Analysis and Its Applications", Holden-Day, 1968.
52. Voutsinos, C. M., "Laser Interferometric Investigation of Microlayer Evaporation for Various Levels of Subcooling and Heat Flux", M.Eng. Thesis, Mech. Eng. Dept., McMaster University, Canada, 1976.

APPENDIX A
ESTIMATE OF HEAT
TRANSFER RATE

In the present investigation, two methods were used to calculate the rate of heat transfer through the boiling surface. The first method considered the rate of heat transfer in the neck of the heater block to be determined by one-dimensional heat conduction using the one-dimensional Fourier conduction equation. The heat transfer in the radial direction was minimized by using vermiculate as an insulation material, so that it was reasonable to assume that

$$\frac{Q}{A} = -k \frac{dT}{dx} \quad (A.1)$$

where $k = 251 \text{ W/mK}$ according to Wiebe [33] and $\frac{dT}{dx}$ is the axial temperature gradient measured in the neck of the heater block.

The second method considered the actual rate of heat transfer as the total rate of heat generation less the rate of heat loss, using the same procedure as Wiebe [20] to calculate the rate of heat loss from the system as shown in figure (56).

A.1 Skirt Heat Loss

The heat loss through the skirt Q_{Fin} is shown in figure (56).

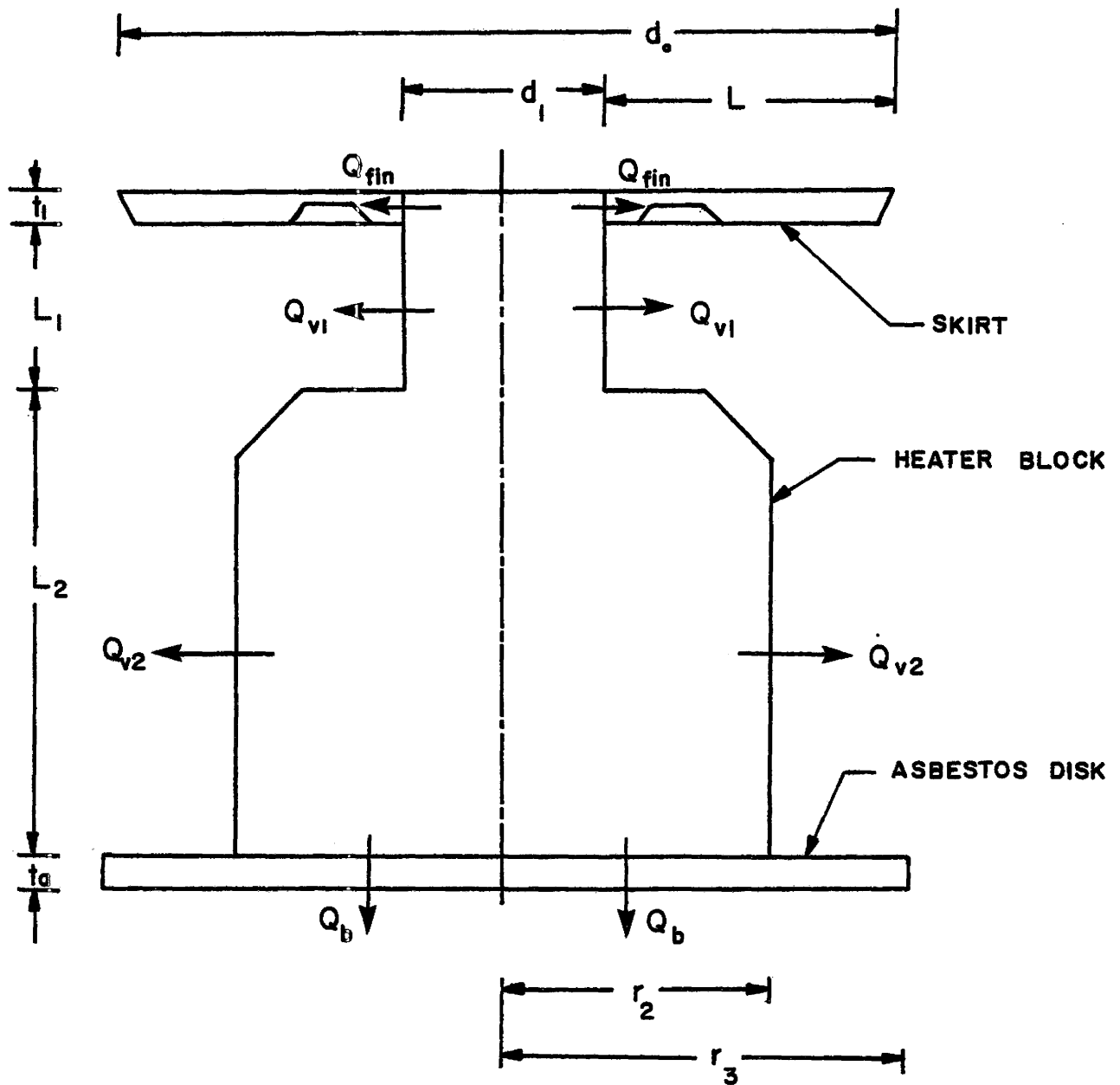


Figure (56). Heat Loss From the Heater Block

$$Q_{Fin} = \eta_f \bar{h}_c A_{Fin} (T_{Fin \text{ Base}} - T_{\infty}) \quad (A.2)$$

where

$$\eta_f = f (2\bar{h}_c L / k_s t_1) = f(mL) \quad (A.3)$$

The functional relationship between η_f and mL is given in reference [32].

$$\begin{aligned} k_s &= 16 \text{ W/mK} \\ \bar{h}_c &= 738.2 \text{ W/m}^2\text{K} \\ t_1 &= 12.7 * 10^{-3} \text{ m} \\ d_o &= 19.7 * 10^{-2} \text{ m} \\ d_i &= 5.1 * 10^{-2} \text{ m} \\ L &= 7.3 * 10^{-2} \text{ m} \\ A_{Fin} &= 2.8 * 10^{-2} \text{ m}^2 \\ mL &= 15.8 * 10^{-2} \end{aligned}$$

Then $\eta_f \approx 8.5 * 10^{-2}$ so that

$$Q_{Fin} = 1.78 (T_{Fin \text{ Base}} - T_{\infty}) \quad (A.4)$$

A.2 Radial Heat Loss Through Vermiculite

The volume occupied by the vermiculate can be considered to be comprised of two hollow cylinders for the analysis of heat transfer in the radial direction Q_{v1} and Q_{v2} as shown in figure (56). The locations of the thermocouples used in this analysis is shown in figure (57).

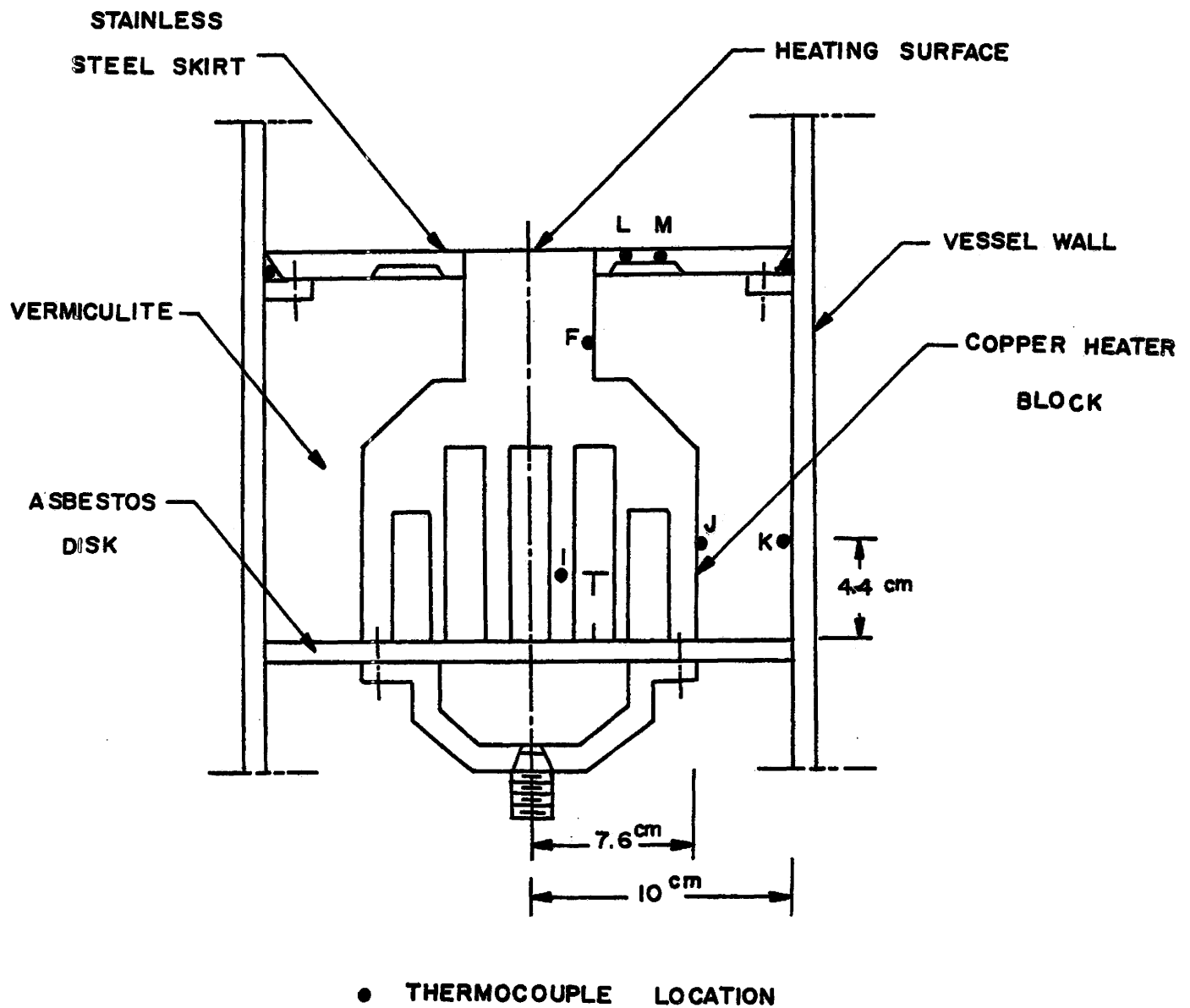


Figure (57). Location of Thermocouples Used in Determining Heat Loss

A.2.1 Heat Loss from Neck of the Heater Block

$$Q_{v1} = \frac{2\pi k_v L_1}{\ln\left(\frac{r_3}{r_i}\right)} (T_F - T_K) \quad (A.5)$$

where

$$k_v = 83 * 10^{-2} \text{ W/mK}$$

$$L_1 = 2.5 * 10^{-2} \text{ m}$$

$$r_i = 2.5 * 10^{-2} \text{ m}$$

$$r_3 = 10 * 10^{-2} \text{ m}$$

Therefore

$$Q_{v1} = 0.094 (T_F - T_K) \quad (A.6)$$

A.2.2 Heat Loss from the Base of the Heater Block

$$Q_{v2} = \frac{2\pi k_v L_2}{\ln\left(\frac{r_3}{r_2}\right)} (T_J - T_K) \quad (A.7)$$

where

$$r_2 = 7.6 * 10^{-2} \text{ m}$$

$$L_2 = 7.6 * 10^{-2} \text{ m}$$

Therefore

$$Q_{v2} = 1.38 (T_J - T_K) \quad (A.8)$$

A.3 Heat Loss from the Bottom Face of the Heater Block

The heat loss from the bottom face Q_b as shown in figure (56) was minimized by using an asbestos disk of

$6.35 * 10^{-3}$ m thickness. Accordingly the heat loss becomes

$$Q_b = \frac{(T_I - T_a)}{\frac{t_a}{k_a A_b} + \frac{1}{\bar{h}_{ca} A_b}} \quad (A.9)$$

where T_a is the surrounding air temperature

$$\begin{aligned} t_a &= 6.35 * 10^{-3} \text{ m} \\ k_a &= 15.6 * 10^{-2} \text{ W/mk} \\ A_b &= 3.6 * 10^{-2} \text{ m}^2 \\ \bar{h}_{ca} &= 0.1615 \left[\frac{T_{I'} - T_a}{d_3} \right] \text{ Reference (32)} \end{aligned} \quad (A.10)$$

$T_{I'}$ is the temperature of the outside surface of the asbestos disk

$$d_3 = 0.2 \text{ m}$$

and therefore

$$Q_b = \frac{(T_I - T_a)}{1.14 + \frac{115.66}{[T_{I'} - T_a]^{1/4}}} \quad (A.11)$$

$T_{I'}$ is obtained by a trial and error procedure as the heat transfer by conduction through the asbestos disk must equal the heat transfer by convection from the bottom face of the disk.

A.4 Numerical Calculation

$$Q_T = 400 \text{ Watts}$$

TABLE (4)
THERMOCOUPLE READINGS

THERMOCOUPLE	TEMPERATURE °C
A	122.50
B	127.20
C	132.10
D	127.15
E	127.15
F	127.10
G	100.00
H	100.00
I	155.20
J	115.20
K	108.72
L	101.10
M	100.50

A.4.1 The First Method

$$\frac{\Delta T}{\Delta x} = 765.3 \text{ K/m as shown in figure (58)}$$

Equation (A.1) gives

$$Q/A = 251 * 765.3 = 192.11 \text{ kW/m}^2$$

A.4.2 The Second Method

$$T_{\text{Fin Base}} = 101.1 \text{ }^{\circ}\text{C}$$

Equation (A.4) gives

$$Q_{\text{Fin Base}} = 1.78 (101.1 - 100) = 1.95 \text{ W}$$

Equation (A.6) gives

$$Q_{v1} = 0.094 (127.1 - 108.72) = 1.72 \text{ W}$$

Equation (A.7) gives

$$Q_{v2} = 1.38 (115.2 - 108.72) = 8.94 \text{ W}$$

Equation (A.11) gives

$$Q_b = \frac{(155.2 - 27.2)}{1.14 + \frac{115.66}{[142.38 - 27.2]^{1/4}}} = 3.51 \text{ W}$$

$$Q_{\text{Loss}} = Q_{\text{Fin Base}} + Q_{v1} + Q_{v2} + Q_b$$

$$= 1.95 + 1.72 + 8.94 + 3.51 = 16.12 \text{ W}$$

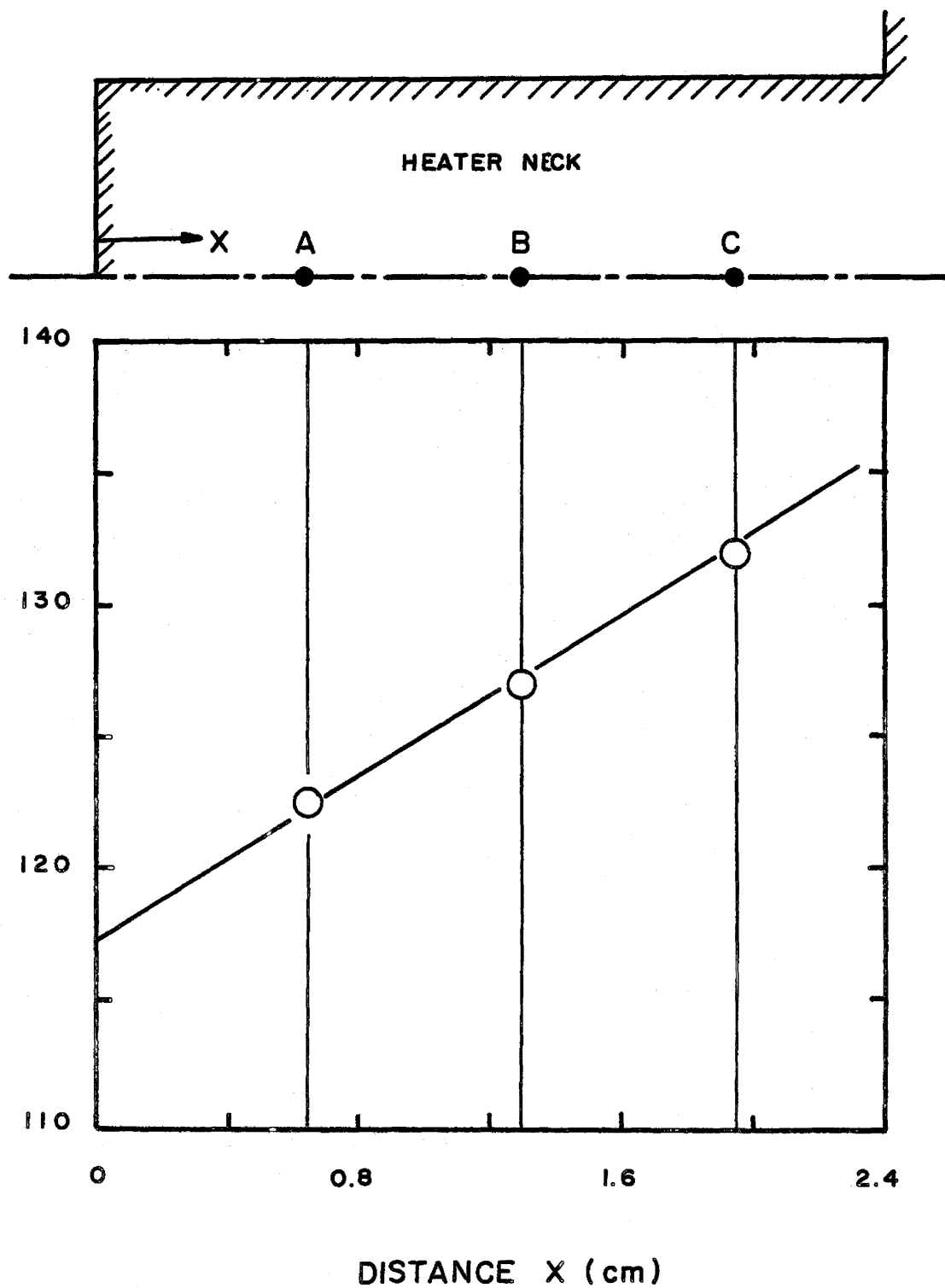


Figure (58). Temperature Gradient in the Heater Neck

$$Q_{\text{Actual}} = 400 - 16.12 = 383.87 \text{ W}$$

$$(Q/A)_{\text{Actual}} = 189.47 \text{ kW/m}^2$$

in comparison with

$$(Q/A) = 192.11 \text{ kW/m}^2$$

giving 1.37% difference.

The first method values were used to represent the value of the rate of heat transfer in the present investigation.

APPENDIX B

BULK LIQUID TEMPERATURE

In the present investigation it was essential to obtain the value of the bulk liquid temperature in both saturation and subcooled conditions. This value was required for computing the subcooling level in each test. The bulk liquid temperature could be determined by considering the temperature variation over the heating surface at different levels. At a certain distance from the surface, the liquid temperature remains constant in both of the saturated and subcooled conditions. A preliminary experimental study was conducted to obtain the liquid temperature distribution above the heating surface using the thermocouple probe shown in figure (59) positioned in the water at different levels as reported by Sultan [21].

Figure (60) shows three temperature profiles for the saturated condition obtained at three different radii. Additionally, figure (61) shows three temperature profiles obtained under conditions of high heat flux level (315 kW/m^2) and highly subcooled boiling liquid (53.9°C). At a displacement of approximately $5 * 10^{-2} \text{ m}$ from the heating surface, the three temperature profiles approach a common value of 100°C for the saturated conditions, whereas for the subcooled conditions, the three curves approach a common value of 46.1°C . Consequently, it was felt that the temperature

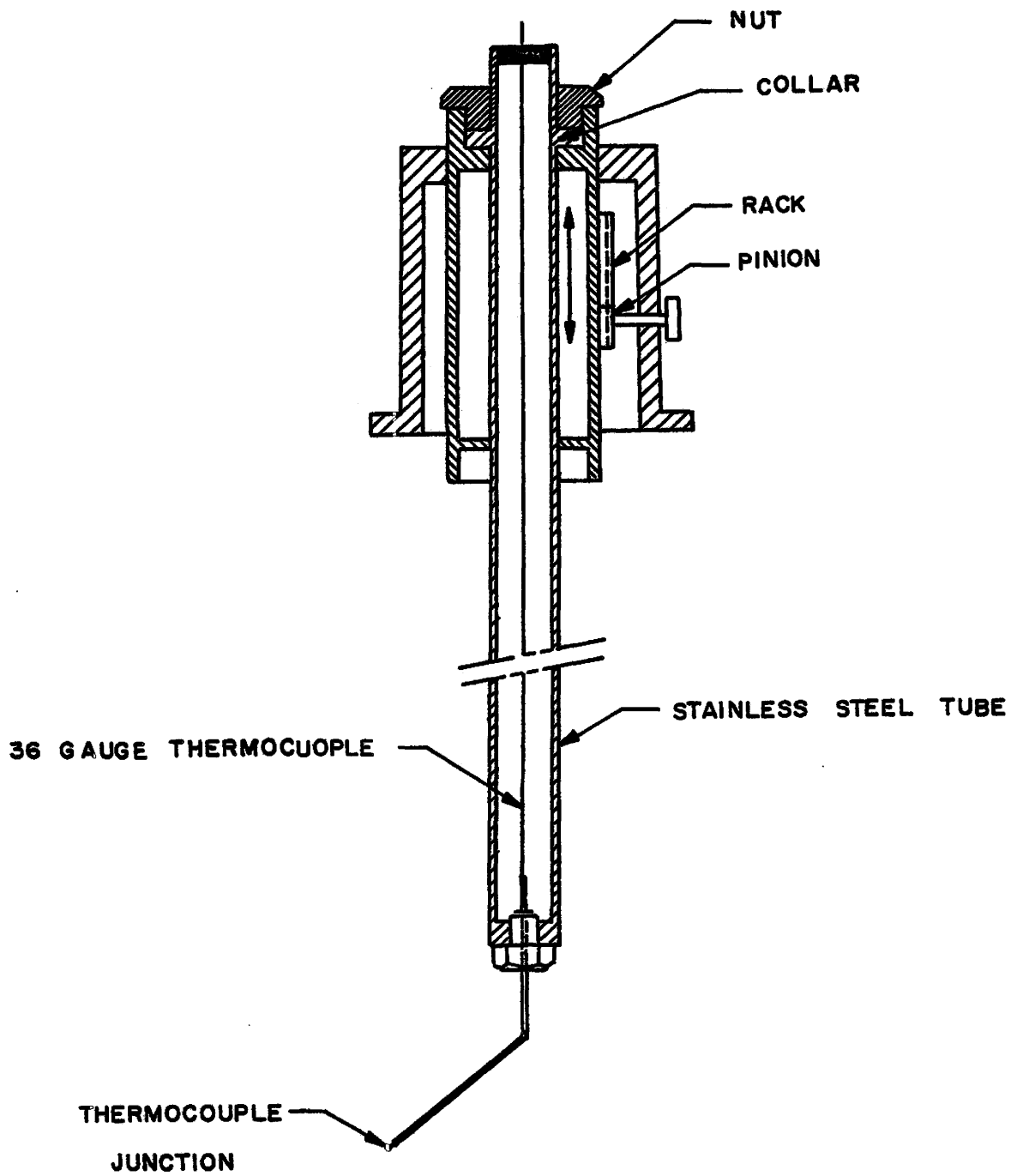


Figure (59). Thermocouple Probe

$$Q/A = 315 \text{ (kW/m}^2\text{)}$$

$$(T_s - T_\infty) = 0 \text{ (}^\circ\text{C)}$$

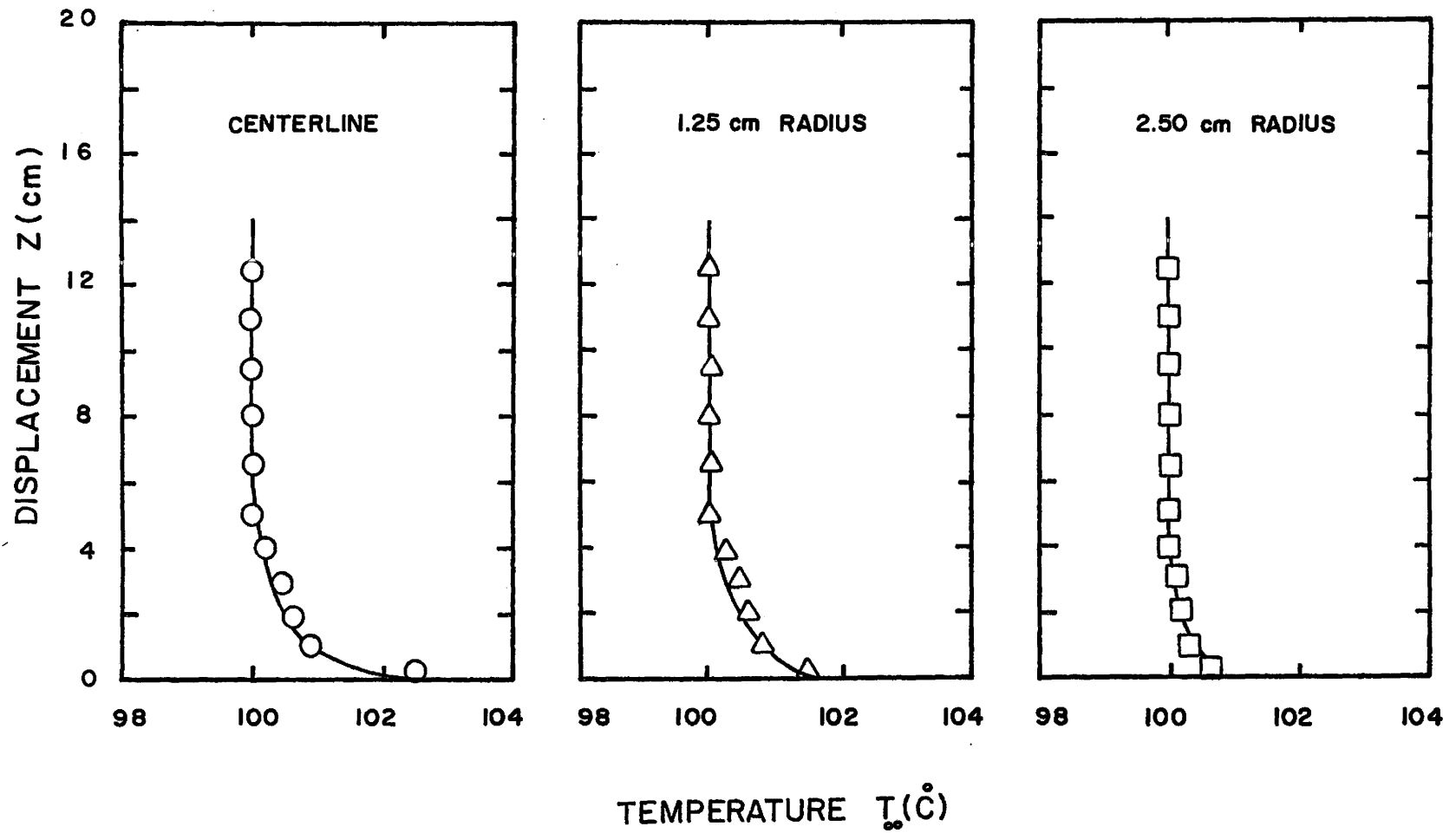


Figure (60). Bulk Liquid Temperature Profiles for Saturated Conditions

$$Q/A = 315 \text{ (kW/m}^2\text{)}$$

$$(T_s - T_\infty) = 53.9 \text{ (}^\circ\text{C)}$$

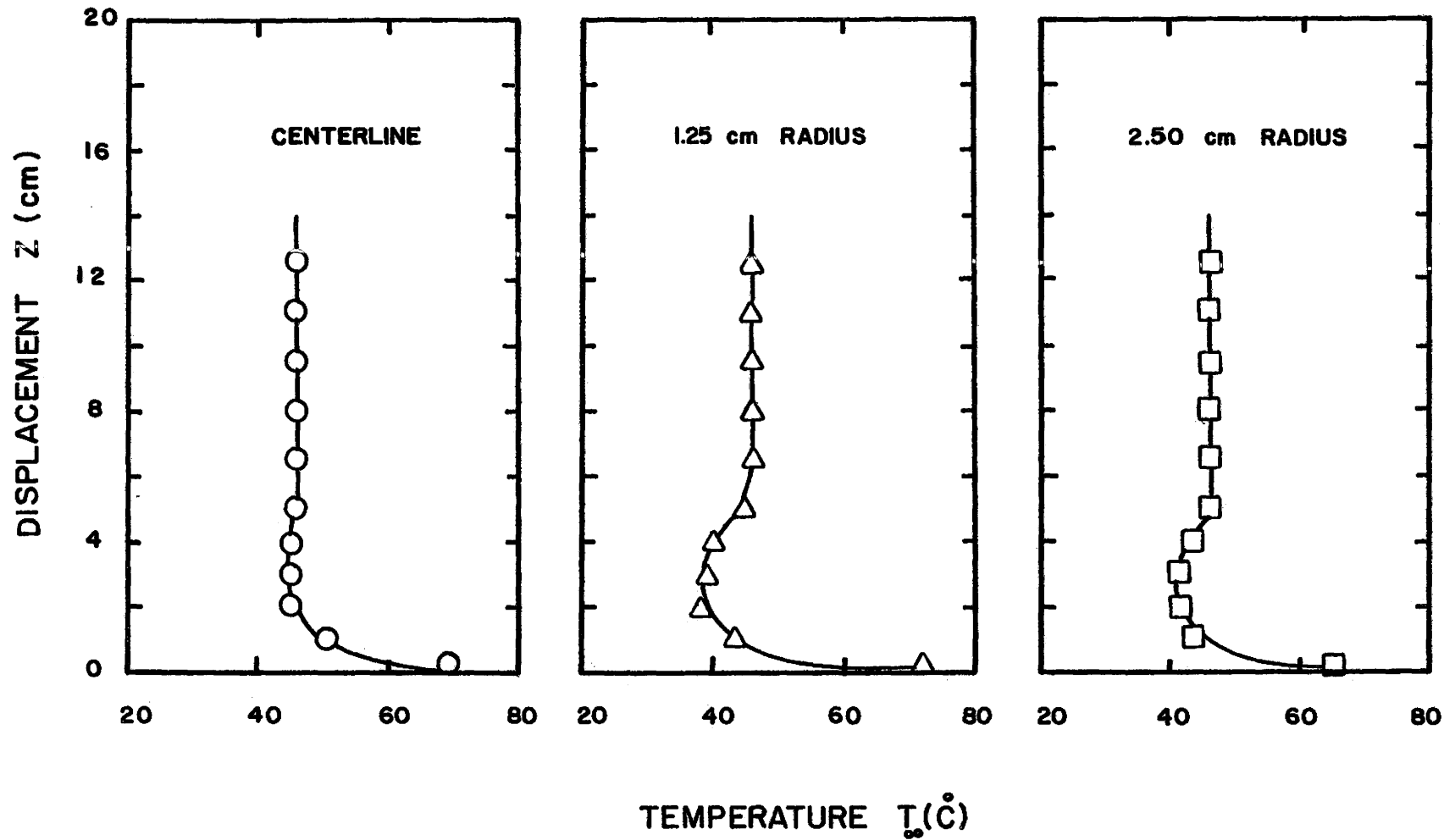


Figure (61). Bulk Liquid Temperature Profiles for Subcooled Conditions

measured at a displacement of $2 * 10^{-2}$ m from the surface would adequately characterize the bulk temperature. During the actual test, thermocouples were located at $5 * 10^{-2}$ m and $10 * 10^{-2}$ m from the heating surface at $2.5 * 10^{-2}$ m radial displacement. The two measurements taken were averaged so that the error resulting from using one thermocouple might be reduced.

APPENDIX C

PROPAGATION OF A TEMPERATURE DISTURBANCE IN A SEMI-INFINITE MEDIUM

In the present investigation the superheated liquid layer at the heating surface is pushed away from the nucleation site and high temperature liquid accumulates at the periphery of the growing bubble on the heating surface as shown schematically in figure (39). On the basis of this observation, the phenomenon responsible for the propagation of a temperature disturbance has been approximated by the diffusion of heat from an instantaneous ring source with strength Q at a radius r' in the plane $Z = 0$, through a semi-infinite medium.

The differential equation of conduction of heat in cylindrical coordinates is

$$\rho c \frac{\partial T}{\partial t} = k \left[\frac{1}{r} \frac{\partial}{\partial r} \left(r \frac{\partial T}{\partial r} \right) + \frac{\partial^2 T}{\partial Z^2} \right] \quad (C.1)$$

The initial conditions are:

$$T(r, 0) = T_0 \quad r=r' \quad (C.2)$$

$$T(r, 0) = 0 \quad r \neq r' \quad (C.3)$$

The boundary conditions are:

$$\frac{\partial T(0, t)}{\partial r} = 0 \quad (C.4)$$

$$T(\infty, t) = 0 \quad (C.5)$$

Carslaw and Jaeger [27] presented the solution of equation (C.1) in the form of

$$\theta'(r, z, t) = \frac{Q/\rho C}{8(\pi \kappa t)^{3/2}} \exp \left[-\frac{r^2 + r'^2 + z^2}{4\kappa t} \right] I_0 \left(\frac{rr'}{2\kappa t} \right) \quad (C.6)$$

Interpreting this solution to suit the problem by putting

$z = 0$, $S = r$, $\tau = t$, $R_d = r'$ and $\theta' = T_\ell - T_{sat}$, then equation (C.6) becomes

$$\theta'(S, \tau) = \frac{Q'/\rho C}{8(\pi \kappa \tau)^{3/2}} \exp \left[-\frac{S^2 + R_d^2}{4\kappa \tau} \right] I_0 \left(\frac{SR_d}{2\kappa \tau} \right) \quad (C.7)$$

The propagation of the maximum temperature disturbance is determined by

$$\left. \frac{\partial \theta(S, \tau)}{\partial \tau} \right|_{S = \text{const.}} = 0$$

Consequently from equation (C.7)

$$\begin{aligned} \left. \frac{\partial \theta'(S, \tau)}{\partial \tau} \right|_{S=\text{const.}} = & \frac{Q/\rho C}{8(\pi \kappa)^{3/2}} \left\{ -\frac{3}{2\tau^{5/2}} * e^{-\frac{S^2 + R_d^2}{4\kappa \tau}} I_0 \left(\frac{SR_d}{2\kappa \tau} \right) \right. \\ & + \frac{1}{\tau^{3/2}} * \frac{S^2 + R_d^2}{4\kappa \tau} e^{-\frac{S^2 + R_d^2}{4\kappa \tau}} I_0 \left(\frac{SR_d}{2\kappa \tau} \right) \\ & \left. + \frac{1}{\tau^{3/2}} * e^{-\frac{S^2 + R_d^2}{4\kappa \tau}} \left[-\frac{SR_d}{2\kappa \tau^2} * \frac{\partial I_0 \left(\frac{SR_d}{2\kappa \tau} \right)}{\partial \left(\frac{SR_d}{2\kappa \tau} \right)} \right] \right\} \quad (C.8) \end{aligned}$$

$$\left. \frac{\partial \theta'(S, \tau)}{\partial \tau} \right|_{S=\text{const.}} = \frac{Q/\rho C}{8(\pi \kappa \tau)^{3/2}} e^{-\left[\frac{S^2 + R_d^2}{4\kappa \tau}\right]} \left\{ -\frac{3}{2\tau} I_0\left(\frac{SR_d}{2\kappa \tau}\right) + \frac{S^2 + R_d^2}{4\kappa \tau^2} I_0\left(\frac{SR_d}{2\kappa \tau}\right) - \frac{SR_d}{2\kappa \tau^2} I_1\left(\frac{SR_d}{2\kappa \tau}\right) \right\} = 0 \quad (C.9)$$

However

$$\begin{aligned} -6\kappa \tau I_0\left(\frac{SR_d}{2\kappa \tau}\right) + (S^2 + R_d^2) I_0\left(\frac{SR_d}{2\kappa \tau}\right) \\ = 2 S R_d I_1\left(\frac{SR_d}{2\kappa \tau}\right) \end{aligned} \quad (C.10)$$

$$[(S^2 + R_d^2) - 6\kappa \tau] = 2 S R_d \left[I_1\left(\frac{SR_d}{2\kappa \tau}\right) / I_0\left(\frac{SR_d}{2\kappa \tau}\right) \right] \quad (C.11)$$

$$(S - R_d)^2 - 6\kappa \tau = \left[2 S R_d \left[I_1\left(\frac{SR_d}{2\kappa \tau}\right) / I_0\left(\frac{SR_d}{2\kappa \tau}\right) \right] - 2 S R_d \right] \quad (C.12)$$

$$(S - R_d)^2 = 6\kappa \tau - 2 S R_d \left[1 - \left[I_1\left(\frac{SR_d}{2\kappa \tau}\right) / I_0\left(\frac{SR_d}{2\kappa \tau}\right) \right] \right] \quad (C.13)$$

$$\frac{(S - R_d)^2}{4\kappa \tau} = \frac{3}{2} - \frac{SR_d}{2\kappa \tau} \left[1 - \left[I_1\left(\frac{SR_d}{2\kappa \tau}\right) / I_0\left(\frac{SR_d}{2\kappa \tau}\right) \right] \right] = F\left(\frac{SR_d}{2\kappa \tau}\right) \quad (C.14)$$

$$(S - R_d) = 2 \sqrt{\kappa \tau} \sqrt{F\left(\frac{SR_d}{2\kappa \tau}\right)} \quad (C.15)$$

$$(S - R_d) = 2 \sqrt{\kappa \tau} H\left(\frac{SR_d}{2\kappa \tau}\right) \quad (C.16)$$

The function $H\left(\frac{SR_d}{2\kappa \tau}\right)$ has been calculated at different values of $(SR_d/2\kappa \tau)$ between 0 to ∞ and the results showed that in the range of interest $0.5 < SR_d/2\kappa \tau < \infty$ the function $H(SR_d/2\kappa \tau)$

varies by less than 5% from unity. Therefore the function

$$(SR_d/2\kappa\tau) \approx 1, \text{ and}$$

$$(S-R_d) \approx 2 \sqrt{\kappa\tau} \quad (C.17)$$

is a good approximation.

For the present conditions

$$\tau = \tau - \tau_g$$

Equation (C.17) becomes

$$(S-R_d) \approx 2 \sqrt{\kappa(\tau - \tau_g)} \quad (C.18)$$

Equation (C.18) represents the propagation of the maximum temperature disturbance in a semi-infinite medium.

APPENDIX D

PREDICTION OF ACTIVE SITE DENSITY, BUBBLE GROWTH PERIOD, BUBBLE EMISSION FREQUENCY AND BUBBLE DEPARTURE SIZE

The active site density N/A_T in nucleate boiling has been reported by Sultan and Judd [2], Kurihara and Myers [33] and Westwater and Gaertner [9] among others. Their results indicated that the active site density increases with increasing heat flux. Sultan and Judd [2] using the present apparatus showed that changes in heat flux and sub-cooling did not affect the pattern of active nucleation sites appreciably. For the lower level of heat flux (92.11 kW/m^2) the value of N/A_T is approximately $4 \times 10^5 \text{ bubble/m}^2$ according to Sultan and Judd's [8] results.

The vapour bubble grows on the heating surface until its size reaches the bubble departure size marking the end of the growth period τ_g , i.e., the bubble growth period ends when,

$$R(\tau_g) = R_d \quad (D.1)$$

The bubble growth period τ_g in the saturation conditions was calculated according to the Mikic and Rohsenow [34] relationship. For the lower level of heat flux (91.11 kW/m^2), the surface superheat is 17°C and the bubble growth period τ_g is approximately 5.9 ms. In the case of subcooled boiling Unal [35] proposed a semi-empirical model to predict bubble

growth period for boiling of water at low velocity as follows.

$$\tau_g = \frac{1}{1.46 \, bc\phi} \quad (D.2)$$

where $\phi = 1$ for $v \leq 0.61 \, \text{m/s}$

$$b = \frac{\Delta T_{\text{sub}}}{2(1 - \rho_v / \rho_l)} \quad (D.3)$$

$$c \approx 65 \quad \text{for} \quad P = 0.1 \, \text{MN/m}^2$$

$$\Delta T_{\text{sub}} = T_{\text{sat}} - T_{\infty}$$

At $\Delta T_{\text{sub}} = 6.5^\circ\text{C}$ and atmospheric pressure conditions

$$b \approx 3.25$$

$$c \approx 65$$

$$\tau_g = 3.2 \, \text{ms}$$

and at $\Delta T_{\text{sub}} = 12.0^\circ\text{C}$ and atmospheric pressure conditions

$$b \approx 6.1$$

$$c \approx 65$$

$$\tau_g = 1.7 \, \text{ms}$$

The formation, growth and departure of a bubble from an active nucleation site is a cyclical process. Therefore the bubble emission frequency is given by

$$f = \frac{1}{\tau_w + \tau_g} \quad (D.4)$$

The bubble cycle time is given by

$$\tau_T = \tau_w + \tau_g \quad (D.5)$$

The average bubble emission frequency was measured by Sultan [21] for boiling water on the same copper surface at atmospheric pressure. At the lower level of heat flux (91.11 kW/m^2) the average bubble emission frequency is approximately 20 bubble/s. Therefore the average bubble cycle time τ_T is approximately 50 ms.

A variety of expressions have been proposed for the bubble departure size. In general, most of them are based on the Fritz [36] relationship which was derived by equating buoyant and surface tension forces. Later Staniszewski [37] and Cole [38] modified the Fritz relationship, taking into account dynamic affects. The bubble departure size D_d for the saturation conditions was calculated according to the Cole and Rohsenow [39] relationship as follows

$$D_d = C \left[\frac{\sigma g_0}{g(\rho_l - \rho_g)} \right]^{1/2} (J_a^*)^{5/4} \quad (D.6)$$

where

$$C = 1.5 * 10^{-4} \quad \text{for water}$$

$$J_a^* \text{ is a modified Jakob number } \left(\frac{\rho_l c_l T_{\text{sat}}}{\rho_v h_{fg}} \right)$$

Mikic and Rohsenow [34] suggested that the prediction of bubble departure diameter D_d when detaching from the heating

surface using equation (D.6) seems to give the best agreement in the whole range of available experimental data for a variety of liquids. For water,

$$\begin{aligned}\sigma &= 54.85 * 10^{-3} \text{ N/m} \\ \rho_l &= 958 \text{ kg/m}^3 \\ \rho_g &= 0.597 \text{ kg/m}^3 \\ T_{\text{sat}} &= 373 \text{ K} \\ h_{\text{fg}} &= 2257 \text{ kJ/kg}\end{aligned}$$

Substitution into equation (D.6) gives

$$D_d = 2.34 \text{ mm}$$

In the case of subcooled boiling the maximum bubble diameter was determined according to Rallis et al. [40] who assumed that the maximum bubble diameter is proportional to the temperature difference between the heating surface and the subcooled liquid as follows.

$$\frac{D_{d_{\text{sub}}}}{D_{d_{\text{sat}}}} = \frac{T_w - T_{\text{sat}}}{T_w - T_{\infty}} \quad (\text{D.7})$$

and derived a general equation to predict the heat flux in both saturated and subcooled boiling; the prediction showed good agreement with their experimental results.

In the present investigation the bubble departure sizes for subcooled boiling were obtained according to reference [40]. At $\Delta T_{\text{sub}} = 6.5^\circ\text{C}$, $D_d = 1.5 \text{ mm}$ and at $\Delta T_{\text{sub}} = 12.0^\circ\text{C}$, $D_d = 1.1 \text{ mm}$.

APPENDIX E

DETERMINATION OF QUALITY IN TWO PHASE MIXTURES

The mass quality of a two phase mixture, x , is defined as

$$x = \frac{m_v}{m_v + m_\ell} \quad (\text{E.1})$$

For a control volume as shown in figure (62) bounded by the maximum bubble diameter at departure from the heating surface in the vertical direction, and per unit area in the horizontal direction the mass quality x for the two phase mixture is obtained as follows. The volume of the vapour bubbles in contact with the heating surface per unit area

$$\frac{V_v}{A_T} = \frac{4}{3} \pi \bar{R}^3 \left(\frac{N}{A_T} \frac{\tau_g}{\tau_T} \right) \quad (\text{E.2})$$

The volume of water in contact with the heating surface per unit area

$$\frac{V_\ell}{A_T} = 2 R_d - \frac{V_v}{A_T} \quad (\text{E.3})$$

so

$$\frac{V_v}{V_\ell} = \frac{1}{\left[\frac{2 R_d}{\frac{4}{3} \pi \bar{R}^3 \frac{N}{A_T} \frac{\tau_g}{\tau_T}} \right] - 1} \quad (\text{E.4})$$

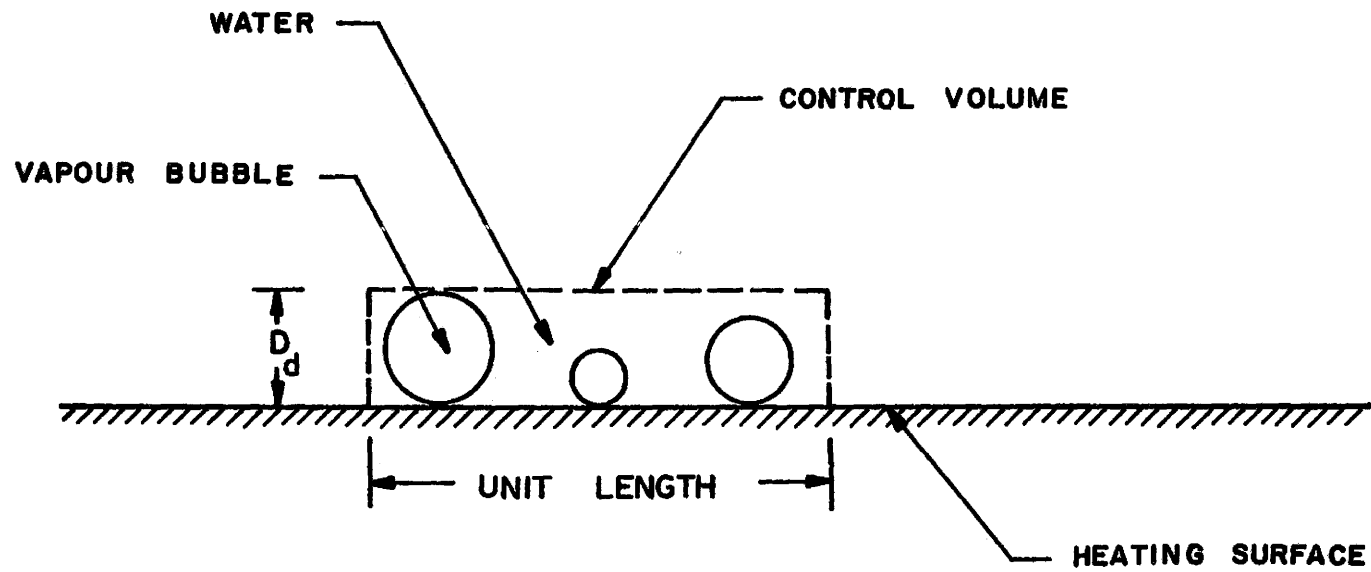


Figure (62). Control Volume for Determination of the Quality of Two-Phase Mixtures

$$\bar{R}^3 = \frac{1}{\tau_g} \int_0^{\tau_g} R^3(t) dt \quad (E.5)$$

$$R(t) = A\sqrt{t} \quad (E.6)$$

where A is constant dependent on the Jakob Number as well as the physical properties of the fluid.

Equation (E.5) becomes

$$\bar{R}^3 = \frac{A^3}{\tau_g} \int_0^{\tau_g} t^{3/2} dt \quad (E.7)$$

$$\bar{R}^3 = \frac{2}{5} A^3 \tau_g^{3/2} \quad (E.8)$$

$$\bar{R}^3 = \frac{2}{5} R_d^3 \quad (E.9)$$

Letting

$$\frac{V_v}{V_l} = \frac{1}{B-1} \quad (E.10)$$

then

$$B = \frac{2 R_d}{\frac{4}{3}\pi \bar{R}^3 \frac{N}{A_T} \frac{\tau_g}{\tau_T}} \quad (E.11)$$

$$B = \frac{2 R_d}{\frac{4}{3}\pi * \frac{2}{5} R_d^3 \frac{N}{A_T} \frac{\tau_g}{\tau_T}} \quad (E.12)$$

resulting in

$$B = \frac{15}{\pi D_d^2 \frac{N}{A_T} \frac{\tau_g}{\tau_T}} \quad (E.13)$$

From equation (E.1)

$$x = \frac{\rho_v V_v}{\rho_v V_v + \rho_l V_l} \quad (\text{E.14})$$

$$x = \frac{1}{1 + \frac{\rho_l V_l}{\rho_v V_v}} \quad (\text{E.15})$$

By substitution of equation (E.13) into equation (E.10)

$$\frac{V_v}{V_l} = \frac{1}{\frac{15}{[\pi D_d^2 \frac{N}{A_T} \frac{\tau_g}{\tau_T}] - 1}} \quad (\text{E.16})$$

For saturated conditions at atmospheric pressure for boiling of water

$$\frac{\rho_l}{\rho_v} = 1602.56 \quad (\text{E.17})$$

Substituting equations (E.16) and (E.17) in equation (E.15) gives

$$x = \frac{1}{1 + 1602.56 \left[\frac{15}{\pi D_d^2 \frac{N}{A_T} \frac{\tau_g}{\tau_T}} - 1 \right]} \quad (\text{E.18})$$

so that the quality x in the two phase mixture is a function of the bubble departure size, active site density and the ratio of the growth to cycle time.

APPENDIX F

TIME DELAY CALIBRATION

The time difference between the start of bubble growth at two neighbouring active sites was calculated by cross-spectral density function analysis and cross-correlation function coefficient analysis for the two probe signals. The time difference between the activity in the two probe signals was considered as the time difference between the start of bubble growth at the two different active sites. In order to obtain confidence in the computer results, a calibration test was done for the time difference τ . Two sine wave signals with the same frequency and amplitude having a varying time shift less than the cycle time were transmitted to an oscilloscope and the DECLAB 11/03 digital computer simultaneously. At the same instant that the signals were digitized by the computer, the signals were also stored on the oscilloscope screen in order to be able to measure the time shift between the two sine waves. The digital computer output for the time delay in the two cases of $x(t)$ leading or lagging $y(t)$ are shown in figure (63). Comparison of these values with the computer obtained values for both cross-spectral density function and cross-correlation function coefficient analysis are shown in figures (64 and 65) which indicate that the computer analysis yields the correct value of the time elapsed between the start of bubble growth at two neighbouring active sites.

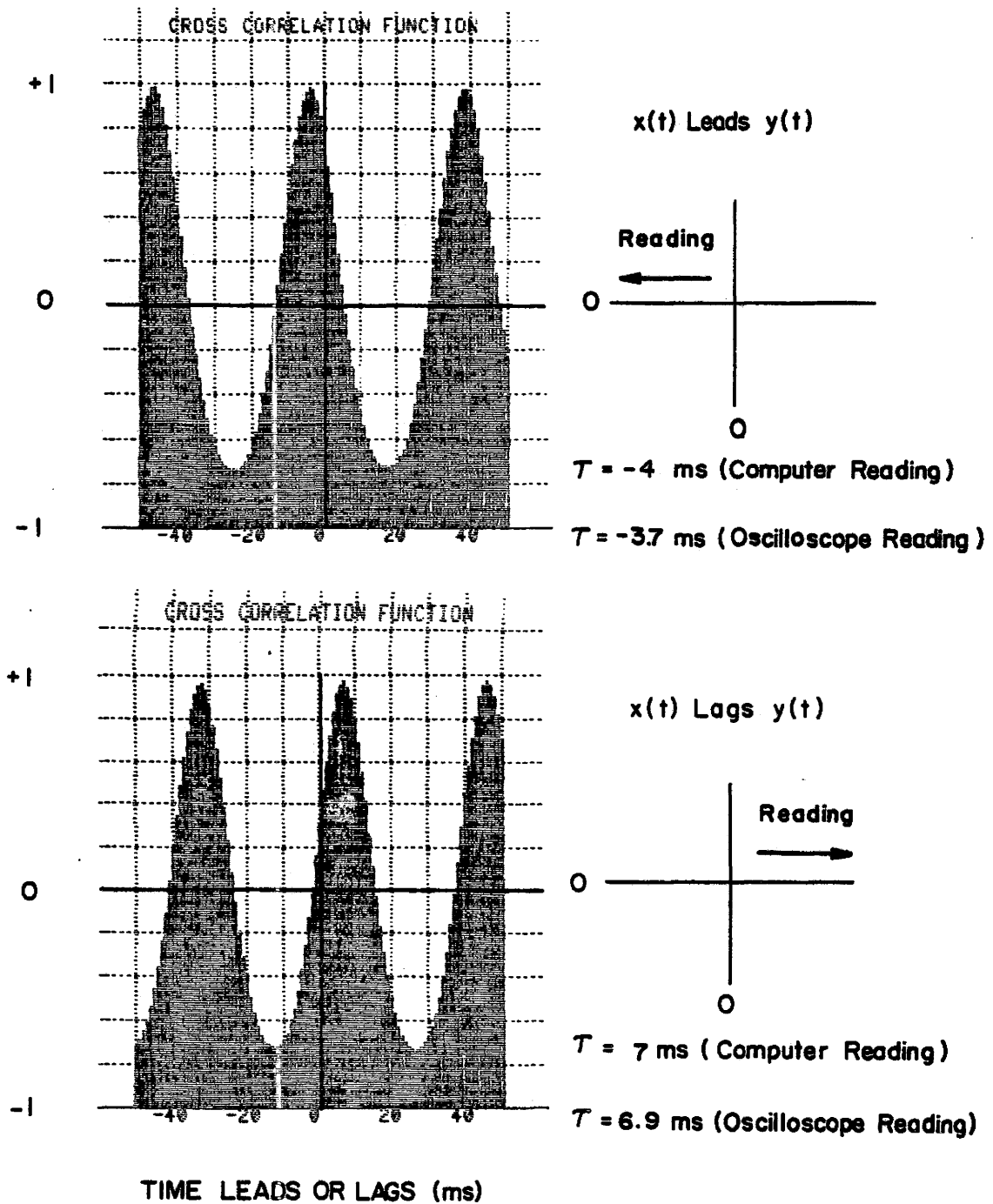


Figure (63). An Example of the Time Delay Calibration for $x(t)$ Leading or Lagging $y(t)$, [Cross-Correlation Function]

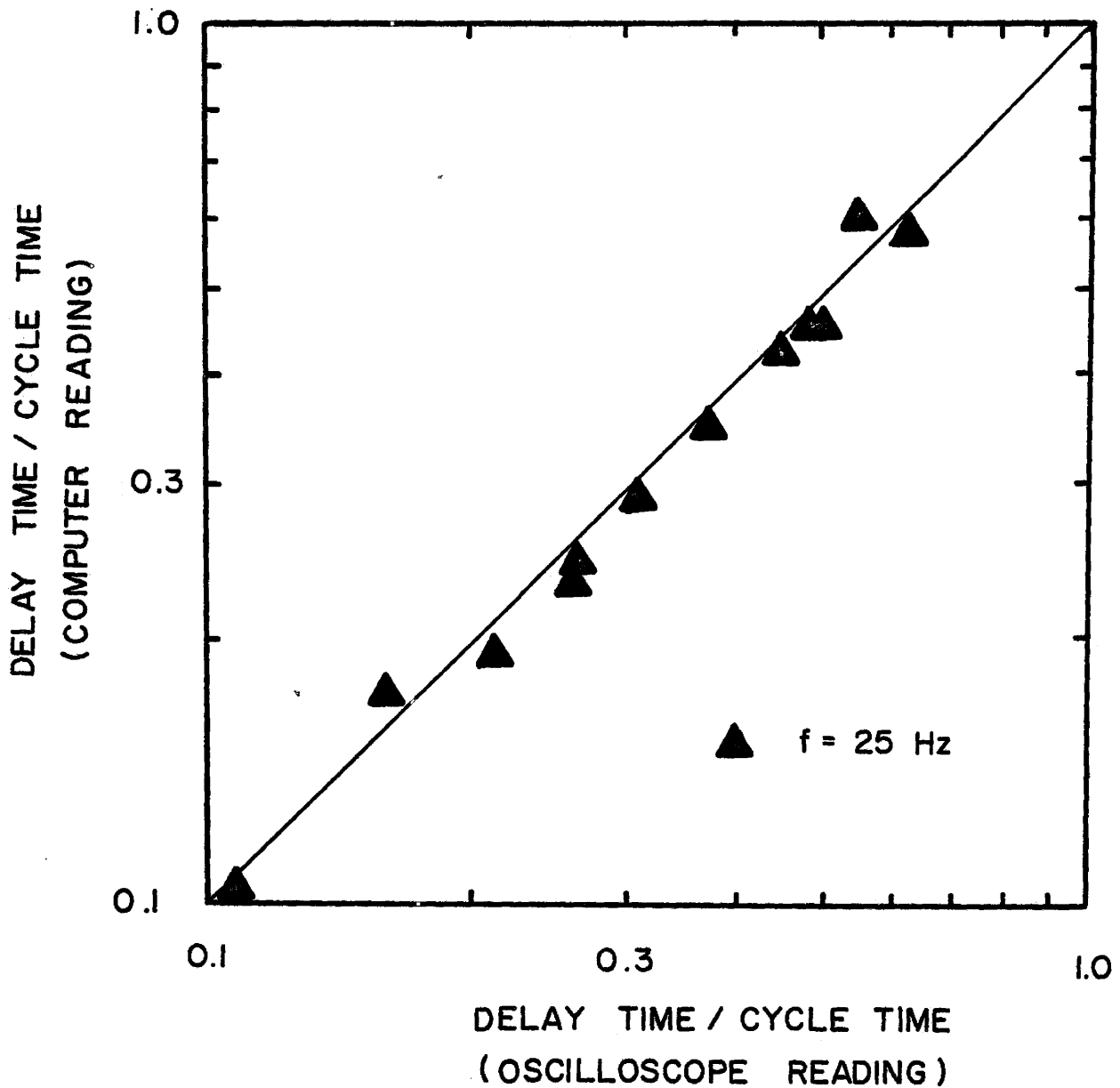


Figure (64). Time Delay Calibration for $x(t)$ Leading or Lagging $y(t)$, [Cross-Correlation Function]

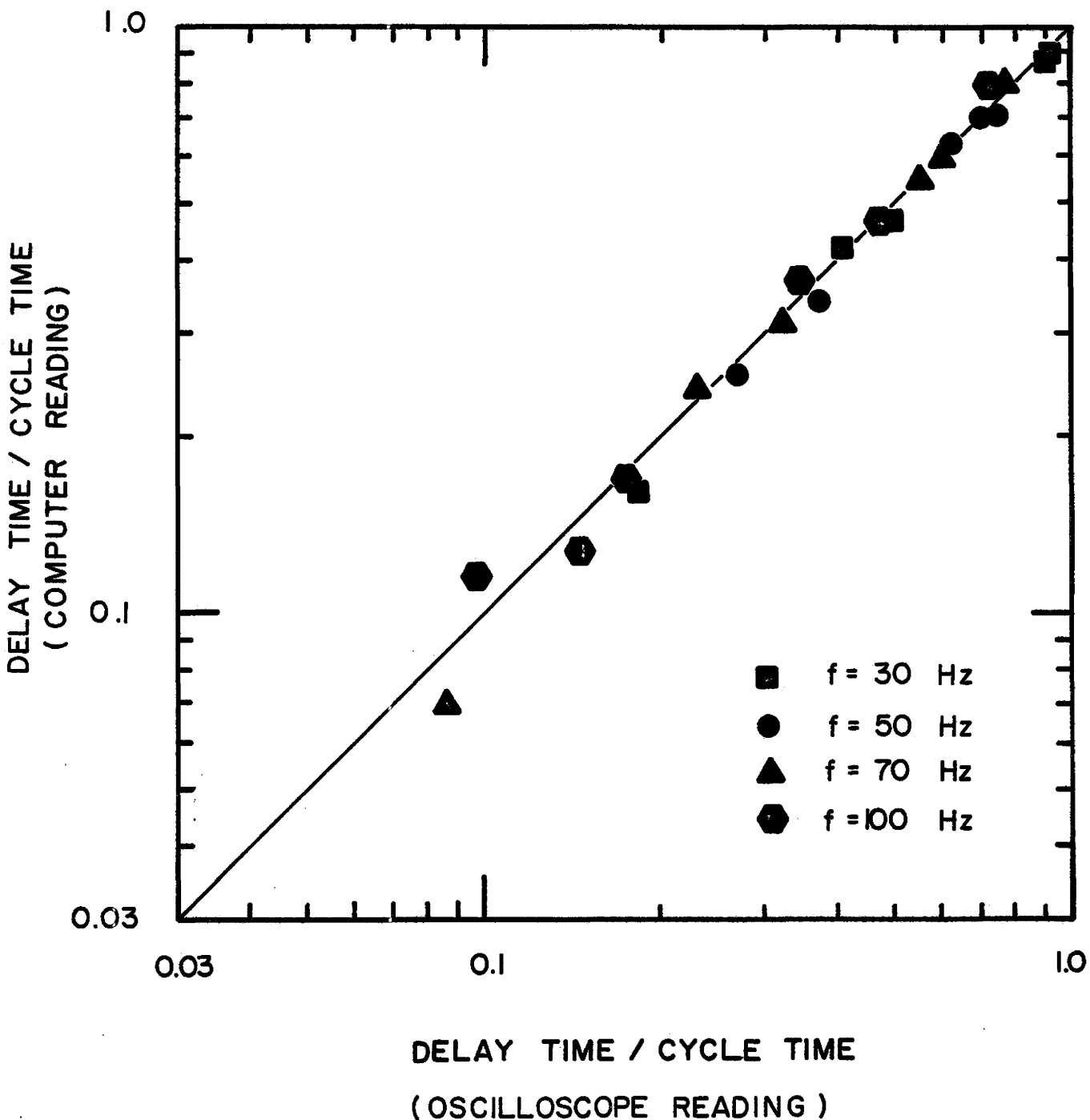


Figure (65). Time Delay Calibration for $x(t)$ Leading or Lagging $y(t)$, [Cross-Spectral Density Function]

APPENDIX G

BUBBLE DETECTION PROBE ASSEMBLY

The single most important component of the apparatus was the bubble detection probe assembly. Alternating current with a frequency of 11,000 Hz at 10 volts passed through the 0.007 inch diameter varnished copper wires of the probe which were bared to the water or vapour in the gap between the heating surface and the tips. It was important to use very small diameter varnished copper wire and to place the wire tips as near as possible to the heating surface in order to detect the bubbles originating from the two neighbouring active sites.

The design details of the bubble detection probe assembly are shown in figure (66). It consisted of two stainless steel cylinders A and B, 1/2 and 1/4 inches in diameter respectively. Cylinder B travelled up and down in the vertical direction while cylinder A was stationary on the X-Y stage. Probe #1 was made in a conical shape having a drilled hole with a diameter of 0.032 inches. A stainless steel tube closely matching the hole diameter was soldered at the tip of the copper cone in order to support the varnished copper wire in such a way as to disturb the flow pattern of the bubble emitted as little as possible. Probe #2, rotated around pivot 0 and a leaf spring was used

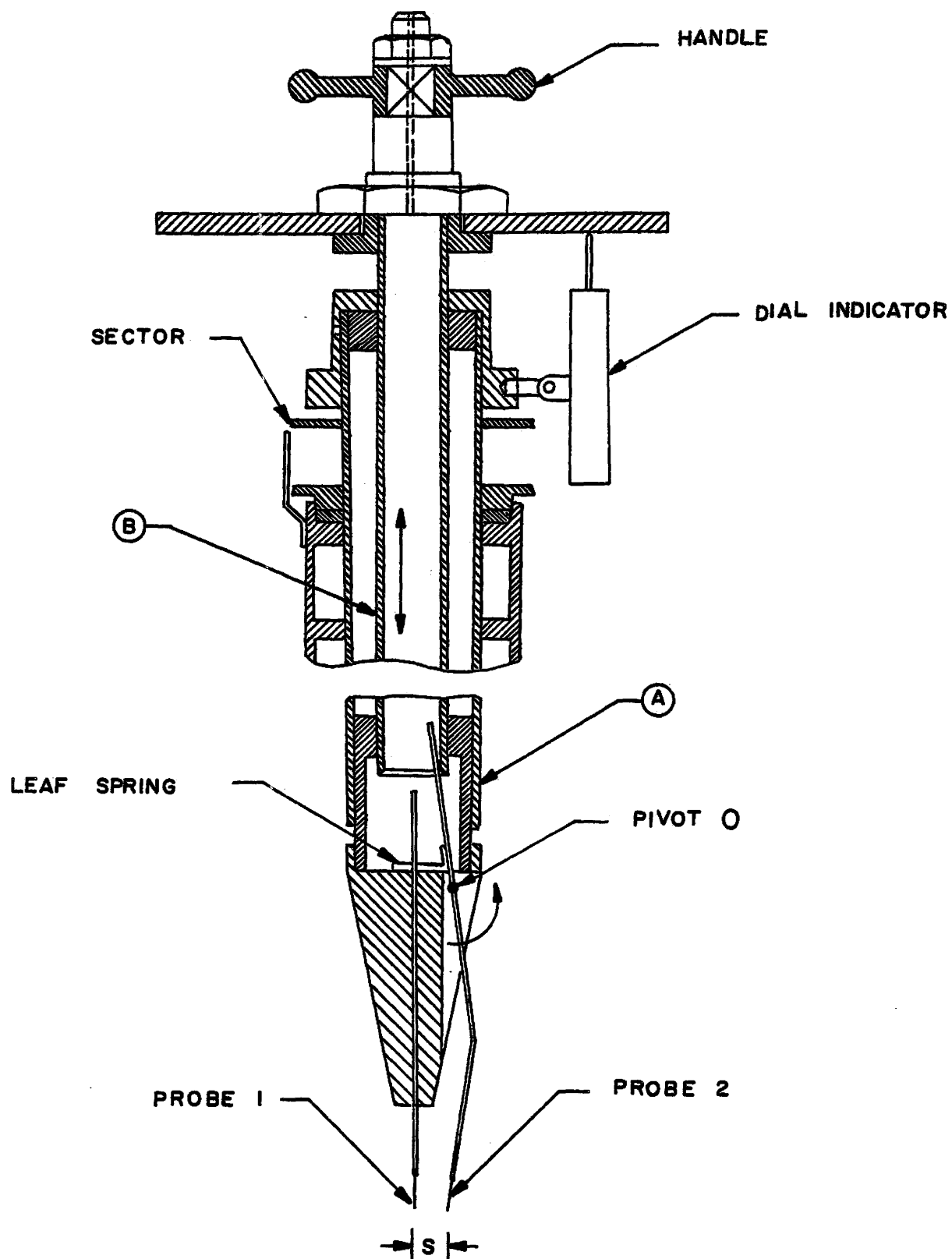


Figure (66). Bubble Detection Probe Assembly

to keep the stainless steel tube in contact with the bottom of cylinder B. When the handle was rotated, cylinder B moved and positioned the stainless steel tube of probe #2, the tube rotated around pivot 0 and a separating distance S was established between the probe tips. Any further movement of cylinder B caused the separation distance S between the probe tips to change. The vertical travel of cylinder B with respect to cylinder A was determined with a dial indicator.

The positioning mechanism which was used for controlling the vertical distance between the copper wire tips and the heating surface is depicted in figure (67). Figure (68) shows the relationship between displacement of the dial indicator and the separating distance between the probe tips.

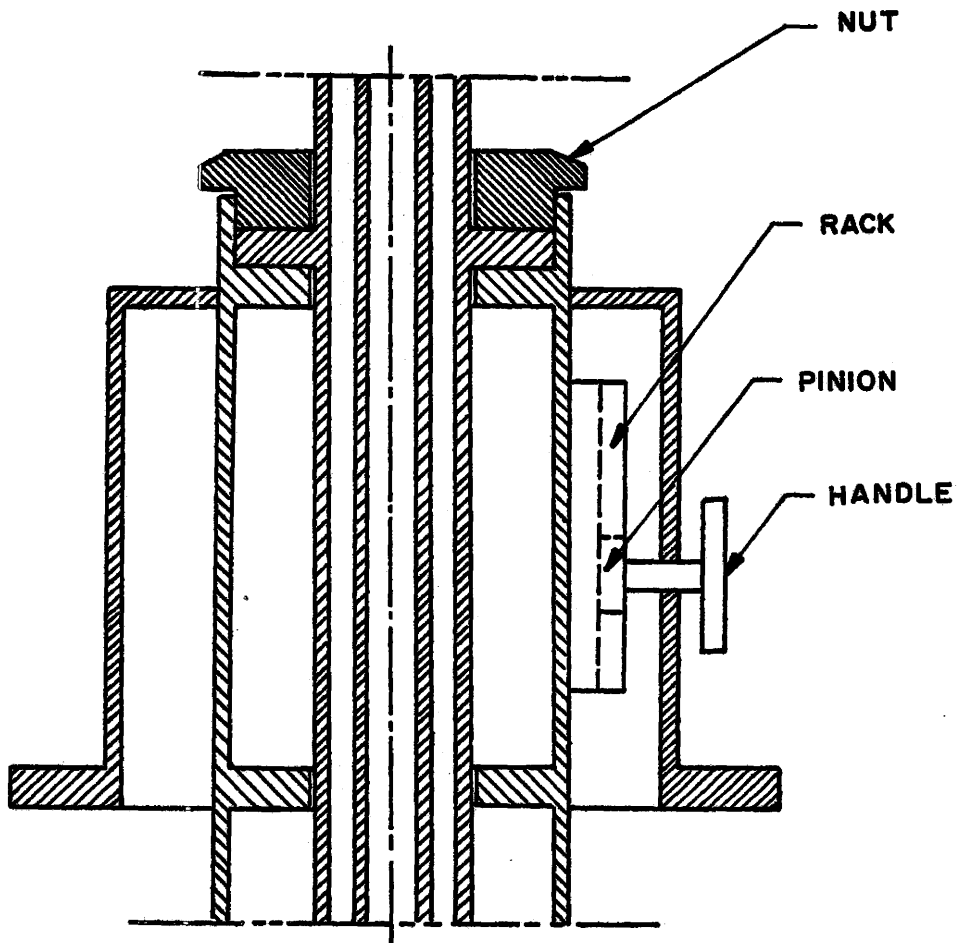


Figure (67). Positioning Mechanism

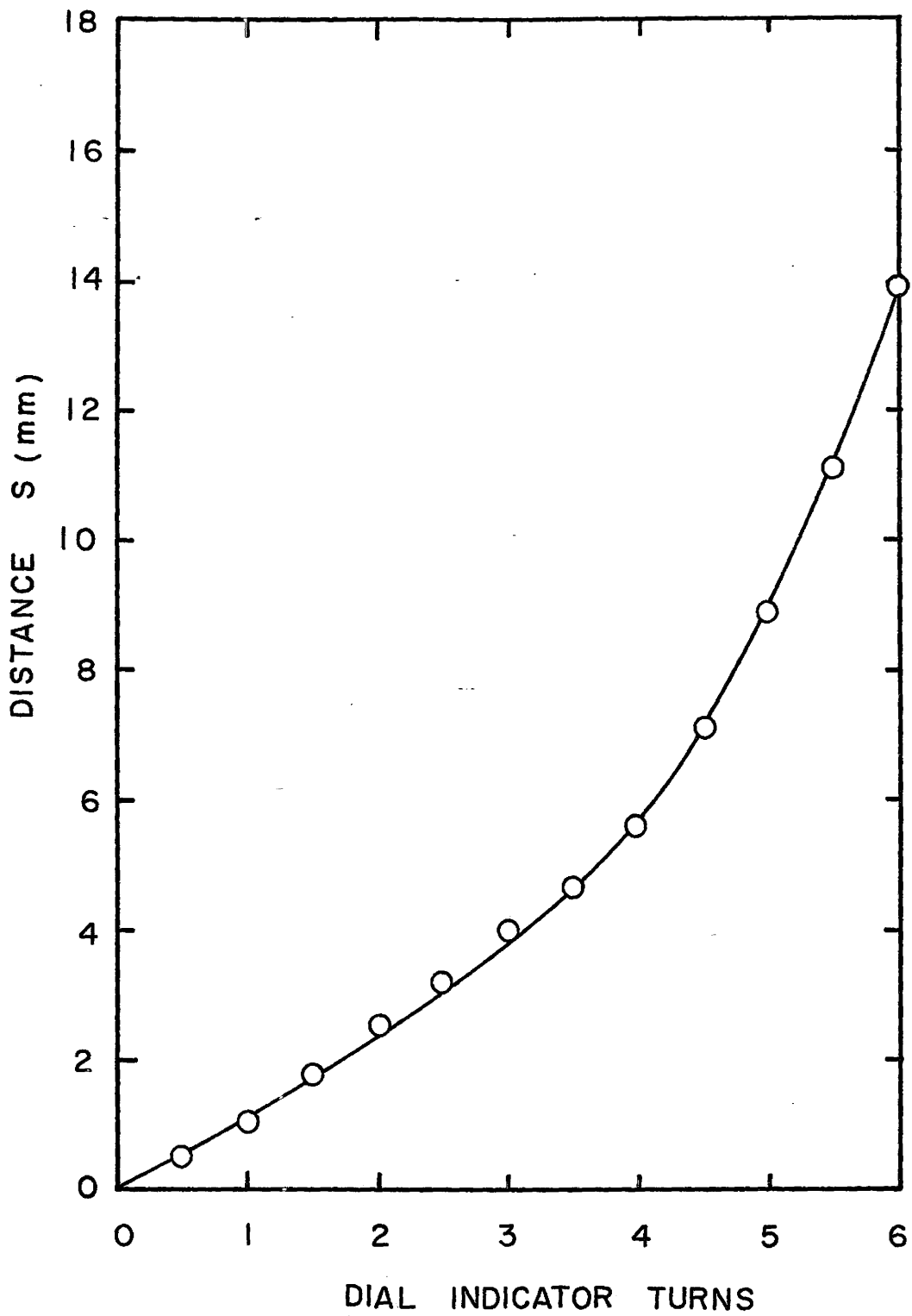


Figure (68). Relationship Between the Separation Distance and the Number of Dial Indicator Turns

APPENDIX H
EXPERIMENTAL DATA AND RESULTS

TABLE (5)
TABULATION OF THE EXPERIMENTAL DATA

Test No.	Heat Flux Q/A (kW/m ²)	Subcooling ΔT_{sub} (°C)	Separation Distance S mm	Time Elapsed τ (ms)
A1	192.11	0	2.2	21
			2.7	No Value
			3.7	No Value
			4.2	24
			4.5	No Value
A2	192.11	0	2.5	No Value
			3.2	No Value
			4.1	No Value
			4.7	No Value
A3	192.11	0	2.1	No Value
			2.9	10
			3.4	No Value
			4.6	No Value
A4	192.11	0	2.7	40
			3.4	No Value
			4.1	No Value
			4.5	No Value
			5.1	No Value
B1	192.11	7.5	2.30	35.0
			2.80	2.0
			2.50	8.0
			5.00	19.0

(continued)

Test No.	Heat Flux Q/A(kW/m ²)	Subcooling ΔT_{sub} (°C)	Separation Distance S mm	Time Elapsed τ (ms)
B2	192.11	7.5	2.25	18.5
			3.33	37.0
			3.50	7.0
			4.30	15.0
			4.70	38.0
			5.50	36.0
			6.50	14.0
B3	192.11	7.5	2.10	20.0
			2.70	11.0
			3.00	10.0
			3.40	28.5
			4.30	15.0
B4	192.11	7.5	2.90	2.0
			3.40	37.0
			4.10	3.0
			5.30	27.0
			6.60	31.0
C	92.21	0	3.00	8.5
			3.50	16.0
			4.00	15.0
			5.50	28.0
			6.50	33.0
D	92.21	7.5	2.00	10.0
			3.00	15.5
			5.50	36.0
			6.50	40.0

(continued)

Test No.	Heat Flux Q/A (kW/m ²)	Subcooling ΔT_{sub} (°C)	Separation Distance S mm	Time Elapsed τ (ms)
E	92.21	0	2.50	8.5
			3.70	19.2
			4.70	32.6
			5.70	34.0
			6.50	35.0
F	92.21	6.5	2.50	24.4
			3.70	52.2
			4.70	49.4
			5.70	41.5
			6.50	50.4
G	92.21	12	2.50	29.4
			3.70	54.3
			4.70	57.3
			5.70	50.0
			6.50	54.8

TABLE (6)

TABULATION OF THE EXPERIMENTAL RESULTS

Test No.	Heat Flux Q/A (kW/m ²)	Subcooling ΔT_{sub} (°C)	(S-R _d)	($\tau - \tau_g$)
E	92.21	0	1.33	2.6
			2.53	13.3
			3.53	26.7
			4.53	28.1
			5.33	29.1
F	92.21	6.5	1.75	21.2
			2.95	49.0
			3.95	46.0
			4.95	38.3
			5.75	47.2
G	92.21	12	1.95	27.7
			3.15	52.6
			4.15	55.6
			5.15	43.3
			5.95	53.1

APPENDIX I
CORRELATION ANALYSIS

The correlation coefficient between the two variables τ and S is given by

$$R_{xy} = \frac{\sum_{i=1}^n (S_i - \bar{S}) (\tau_i - \bar{\tau})}{\left[\sum_{i=1}^n (S_i - \bar{S})^2 \right]^{1/2} \left[\sum_{i=1}^n (\tau_i - \bar{\tau})^2 \right]^{1/2}} \quad (I.1)$$

The quantity R_{xy} is a measure of the association between the two variables, the correlation coefficient R_{xy} lying between -1 and +1. For the case of $R_{xy} = 1$, the two variables τ and S are perfectly positively correlated and the possible values of τ and S all lie on a straight line, with a positive slope in the (τ, S) plane. If $R_{xy} = -1$, the two variables τ and S are perfectly negatively correlated and the possible values of τ and S again lie on a straight line, with a negative slope in the (τ, S) plane. If $R_{xy} = 0$, the two variables are uncorrelated, that is, linearly unassociated with each other.

In the present investigation the correlation coefficient for the different levels of heat flux and different levels of subcooling were calculated according to equation (I.1). The computed results are represented in Table (5).

TABLE (7)

CORRELATION COEFFICIENT ANALYSIS

Test No.	$\sum_{i=1}^n (S_i - \bar{S})^2$	$\sum_{i=1}^n (\tau_i - \bar{\tau})^2$	$\sum_{i=1}^n (S_i - \bar{S})(\tau_i - \bar{\tau})$	R_{xy}
B1	5.345	630.00	-16.50	-0.28
B2	12.22	1008.32	10.24	0.092
B3	5.70	319.44	17.51	0.41
B4	8.97	1071.00	45.60	0.465
C	8.50	406.20	58.25	0.99
D	13.24	660.50	93.07	0.99